UNIVERSITY OF OKLAHOMA

GRADUATE COLLEGE

ANALYSIS OF ENVIRONMENTAL MODIFICATIONS BY DEEP CONVECTION DURING THE MESOSCALE PREDICTABILITY EXPERIMENT

A DISSERTATION

SUBMITTED TO THE GRADUATE FACULTY

in partial fulfillment of the requirements for the

Degree of

DOCTOR OF PHILOSOPHY

By

CHRISTOPHER ANDREW KERR
Norman, Oklahoma
2017

ANALYSIS OF ENVIRONMENTAL MODIFICATIONS BY DEEP CONVECTION DURING THE MESOSCALE PREDICTABILITY EXPERIMENT

A DISSERTATION APPROVED FOR THE
SCHOOL OF METEOROLOGY

BY

Dr. Xuguang Wang, Chair

Dr. David Stensrud, Co-Chair

Dr. Steven Cavallo

Dr. Michael Coniglio

Dr. Alan Shapiro

Dr. S. Lakshmivarahan

Acknowledgements

First and foremost, I’m greatly appreciative of my advisors Drs. David Stensrud and Xuguang Wang. Their guidance over the course of my time as a graduate student has been invaluable and has placed me in a position to successfully carry out my research goals. I am also grateful for the input provided by my entire committee. Many discussions were had with several colleagues and mentors including Ryan Sobash, Glen Romine, Morris Weisman, Jeff Anderson, Kent Knopfmeier, Dusty Wheatley, Lou Wicker, Corey Potvin, Pat Skinner, Thomas Jones, Nusrat Yussouf, Jack Kain, Gerry Creager, Monte Flora, Chris Bednarczyk, Derek Stratman, Stacey Hitchcock, and Sam Degelia.

On a more personal note, this would not have been possible without the support of my wife/personal cheerleader, Rebecca, and the many opportunities provided by my parents and best educators, Steve and Diane. Special thanks to my brothers and friends have allowed me to keep laughing throughout this journey.

Table of Contents

Acknowledgements iv
List of Tables vi
List of Figures vii
Abstract xvii
Chapter 1: Introduction 1
  1.1 Background and motivation 1
  1.2. MPEX upsonde operations and convective events 4
Chapter 2: Methodology 9
  2.1 Mesoscale data assimilation 12
  2.2 Storm-scale data assimilation 12
  2.3 Convective perturbation technique 15
  2.4 Ensemble sensitivity analysis 18
    2.4.1 ESA on the storm-scale 19
    2.4.2 ESA statistical significance testing 20
Chapter 3: Verification of ensemble near-storm environment analyses and forecasts 24
  3.1 Near-storm environment analysis errors 24
  3.2 Bias distributions 38
  3.3 Physics dependent errors 40
  3.4. Near-storm environment forecast errors 43
  3.5. Discussion and conclusions 51
Chapter 4: Environmental modifications by convection 55
  4.1 Vertical wind shear and CAPE perturbations 55
  4.2 Cold pools 70
  4.3 Upper troposphere 77
  4.4 Discussion and conclusions 91
Chapter 5: Ensemble sensitivity analysis (ESA) applied to convective-scale forecasts 92
  5.1 29 May MCS results 92
  5.2 30 May non-tornadic supercell results 104
  5.2 31 May tornadic supercell results 112
  5.4 Supercell evolution sensitivity to storm-induced shear perturbations 126
  5.5 Discussion and conclusions 133
Summary 137
References 140

List of Tables

Table 2.1. Physics options applied to 18 GEFS members. This set of physics options also is applied to these same 18 GEFS members in reverse order to create members 19-36 (for example, member 19 is initialized with GEFS member 18 but has physics option 1 applied). The Thompson microphysics and RAP land surface parameterization is applied to all members. PBL schemes include the Yonsei University (YSU), Mellor–Yamada–Janjic (MYJ), and Mellor–Yamada–Nakanishi–Niino (MYNN) schemes. Shortwave (SW) and longwave (LW) radiation schemes include the Dudhia shortwave scheme, Rapid Radiative Transfer Model (RRTM) shortwave scheme, and the Rapid Radiative Transfer Model–Global (RRTMG) shortwave and longwave schemes (adapted from Wheatley et al. 2015)…………………………………………………...10

Table 2.2. Description of the convective events each day. The start and end times of radar data assimilation are listed with the corresponding radars that collected the data including Dodge City, KS (KDDC), Amarillo, TX (KAMA), Vance Air Force Base, OK (KVNX), Wichita, KS (KICT), Oklahoma City, OK (KTLX), and Frederick, OK (KFDR). The number of MPEX upsondes released during each event are listed last…14

Table 3.1. Sfc-700 hPa and Sfc-500 hPa wind shear RMSD and MB for all upsondes and each individual near-storm environment region. All RMSDs and MBs are in m s^{-1}. The number of shear observations within each region is listed last……………………30

Table 5.1. List of scalar forecast metrics (*J*) and initial condition variables (*x*) for which ESA is applied on each day……………………………………………………………95

List of Figures

Figure 1.1. Hourly observed reflectivity 30 dBZ contours for (a) 28 May 2100 UTC (black), 2200 UTC (blue), and 2300 UTC (green), (b) 29 May 2100 UTC (black), 2200 UTC (blue), and 2300 UTC (green), (c) 30 May 1900 UTC (black), 2000 UTC (blue), 2100 UTC (green), and 2200 UTC (gray), (d) 31 May 2200 UTC (black), 2300 UTC (blue), 1 June 0000 UTC (green), 0100 UTC (gray). MPEX upsonde releases are denoted with circles (NSSL-red, Purdue-orange, CSU-yellow, TAMU-purple)............. 7

Figure 1.2. 2100 UTC 28 May MPEX sounding skew-T thermodynamic profiles and hodographs with NSSL (red), Purdue (orange), CSU (green), and TAMU (purple)........ 8

Figure 2.1. Outer model domain (CONUS; 15 km grid spacing) and nested, convection-resolving domain (3 km grid spacing) which includes KS, OK, and the TX Panhandle. 11

Figure 2.2. One hour changes in ensemble mean analysis 0-6 km vertical wind shear from 2130 – 2230 UTC on 31 May 2013 (filled) and low-level reflectivity analysis (black contours), (a) mesoscale domain (b) storm-scale domain (c) difference between mesoscale and storm-scale domain, revealing changes induced by convection……… 17

Figure 2.3. 24-hour average forecasted MSLP (within box) sensitivity to initial condition MSLP (adapted from Torn and Hakim 2008)……………………………… 22

Figure 2.4. Example scatterplots of ensemble initial condition 0-6 km shear (m s^{-1}) and forecast 2-5 km UH (m^{2}s^{-2}) for a statistically significant sensitivity (top) and statistically insignificant sensitivity (bottom). The regression slope is more pronounced in the significant case (slope: 3.2, standard error: 1.5) than in the insignificant case (slope: 1.4 (abs), standard error: 1.5)……………………………………………………………23

Figure 3.1. Examples of low-level ensemble mean analysis reflectivity and surface winds in knots (barbs) with observed 20 dBZ reflectivity outlined with solid black line, at 0.5^{o} tilt by the designated radar, (a) 2300 UTC 28 May (KDDC), (b) 2200 UTC 29 May (KAMA), (c) 2000 UTC 20 May (KTLX), (d) 2300 UTC 31 May (KTLX). Example radial velocity (e) and reflectivity (f) sawtooth diagrams show ensemble mean prior and posterior RMSE (blue) and ensemble total spread (green) from 28 May with time (minutes) after storm-scale assimilation begins………………………………… 31

Figure 3.2. Number of MPEX upsonde samples with height 28-31 May. All (black), inflow (thick blue), non-inflow (thin blue), outflow (thick green), non-outflow (thin green), anvil (thick red), and non-anvil (thin red)…………………………………….. 32

Figure 3.3. Vertical profiles of temperature (T) root mean square difference (RMSD, solid), mean ensemble spread (MES, dashed), and mean bias (MB, solid). All upsonde RMSD and MES, 1000-100 hPa (a), all upsonde MB, 1000-100 hPa (b), inflow (red) and non-inflow (blue) RMSD and MES, 1000-500 hPa (c), inflow (red) and non-inflow (blue) MB, 1000-500 hPa (d), outflow (red) and non-outflow (blue) RMSD and MES, 1000-500 hPa (e), outflow (red) and non-outflow (blue) MB, 1000-500 hPa (f), anvil (red) and non-anvil (blue) RMSD and MES, 1000-100 hPa (g), anvil (red) and non-anvil (blue) MB, 1000-100 hPa (h)…………………………………………………… 33

Figure 3.4. As in Fig. 3.3, but for relative humidity (RH)…………………………… 34

Figure 3.5. As in Fig. 3.3, but for zonal winds (u-wind)……………………......... 35

Figure 3.6. As in Fig. 3.3, but for meridional winds (v-wind)………………………...36

Figure 3.7. As in Fig. 3.3, but for wind speed…………………………………………37

Figure 3.8. Individual ensemble member bias histograms where frequency is number of ensemble member biases over all 81 samples (2,916 total) for (a) 875 hPa temperature with 0.5 K bins, (b) 750 hPa relative humidity, 5% bins, (c) 225 hPa u-wind, 1 m s^{-1} bins, and (d) 200 hPa v-wind, 1 m s^{-1} bins……………………………………………..39

Figure 3.9. RMSD and MB for mean of members with specific physics schemes (YSU PBL – red, MYJ PBL – blue, MYNN PBL – green, Dudhia-RRTM combination – black, RRTMG combination – magenta). Profiles are for temperature RMSD (a), temperature MB (b), relative humidity RMSD (c), relative humidity MB (d), u-wind RMSD (e), u-wind MB (f), v-wind RMSD (g), and v-wind MB (h)…………………..42

Fig. 3.10. Vertical profiles of one-hour forecast temperature (T) root mean square difference (RMSD, solid), mean ensemble spread (MES, dashed), and mean bias (MB, solid). All upsonde RMSD and MES, 1000-100 hPa (a), all upsonde MB, 1000-100 hPa (b), inflow (red) and non-inflow (blue) RMSD and MES, 1000-500 hPa (c), inflow (red) and non-inflow (blue) MB, 1000-500 hPa (d), outflow (red) and non-outflow (blue) RMSD and MES, 1000-500 hPa (e), outflow (red) and non-outflow (blue) MB, 1000-500 hPa (f), anvil (red) and non-anvil (blue) RMSD and MES, 1000-100 hPa (g), anvil (red) and non-anvil (blue) MB, 1000-100 hPa (h)……………………………………..46

Fig. 3.11. As in Fig. 3.10, but for relative humidity (RH)……………………………..47

Fig. 3.12. As in Fig. 3.10, but for zonal winds (u-wind)………………………………48

Fig. 3.13. As in Fig. 3.10, but for meridional winds (v-wind)…………………………49

Fig. 3.14. As in Fig. 3.10, but for wind speed…………………………………………..50

Figure 4.1. Ensemble mean analysis 0-6 km vertical wind shear in m s^{-1} (filled) and low-level reflectivity (black contours) on 29 May 2013 at (a) 2100 UTC (b) 2130 UTC (c) 2200 UTC (d) 2230 UTC……………………………………………………...58

Figure 4.2. 29 May 2013 ensemble mean analysis 0-6 km vertical wind shear difference in m s^{-1} from 2100 UTC due to convection (filled) and low-level reflectivity at (a) 2130 UTC (b) 2200 UTC (c) 2230 UTC…………………………………………………..59

Figure 4.3. Ensemble mean analysis 0-6 km vertical wind shear in m s^{-1} (filled) and low-level reflectivity (black contours) on 30 May 2013 at (a) 1900 UTC (b) 1930 UTC (c) 2000 UTC (d) 2030 UTC……………………………………………………...60

Figure 4.4. Ensemble mean analysis 0-6 km vertical wind shear in m s^{-1} (filled) and low-level reflectivity (black contours) on 31 May 2013 at (a) 2130 UTC (b) 2200 UTC (c) 2230 UTC (d) 2300 UTC……………………………………………………...61

Figure 4.5. 30 May 2013 ensemble mean analysis 0-6 km vertical wind shear difference in m s^{-1} from 1900 UTC due to convection (filled) and low-level reflectivity at (a) 1930 UTC (b) 2000 UTC (c) 2030 UTC…………………………………………………..62

Figure 4.6. 31 May 2013 ensemble mean analysis 0-6 km vertical wind shear difference in m s^{-1} from 2130 UTC due to convection (filled) and low-level reflectivity at (a) 2200 UTC (b) 2230 UTC (c) 2300 UTC…………………………………………………..63

Figure 4.7. Ensemble mean analysis CAPE in J kg^{-1} (filled) and low-level reflectivity (black contours) on 29 May 2013 at (a) 2100 UTC (b) 2130 UTC (c) 2200 UTC (d) 2230 UTC…………………………………………………………………...........64

Figure 4.8. 29 May 2013 ensemble mean analysis CAPE difference in J kg^{-1} from 2100 UTC due to convection (filled) and low-level reflectivity at (a) 2130 UTC (b) 2200 UTC (c) 2230 UTC……………………………………………………………..65

Figure 4.9. Ensemble mean analysis CAPE in J kg^{-1} (filled) and low-level reflectivity (black contours) on 30 May 2013 at (a) 1900 UTC (b) 1930 UTC (c) 2000 UTC (d) 2030 UTC………………………………………………………………….......66

Figure 4.10. 30 May 2013 ensemble mean analysis CAPE difference in J kg^{-1} from 1900 UTC due to convection (filled) and low-level reflectivity at (a) 1930 UTC (b) 2000 UTC (c) 2030 UTC……………………………………………………………..67

Figure 4.11. Ensemble mean analysis CAPE in J kg^{-1} (filled) and low-level reflectivity (black contours) on 31 May 2013 at (a) 2130 UTC (b) 2200 UTC (c) 2230 UTC (d) 2300 UTC…………………………………………………………………………68

Figure 4.12. 31 May 2013 ensemble mean analysis CAPE difference in J kg^{-1} from 2130 UTC due to convection (filled) and low-level reflectivity at (a) 2200 UTC (b) 2230 UTC (c) 2300 UTC…………………………………………………………………..69

Figure 4.13. Ensemble mean analysis lowest model level temperature in ^{o}C (filled) and low-level reflectivity (black contours) on 29 May 2013 at (a) 2100 UTC (b) 2130 UTC (c) 2200 UTC (d) 2230 UTC……………………………………………………...71

Figure 4.14. 29 May 2013 ensemble mean analysis lowest model level temperature difference in ^{o}C from 2100 UTC due to convection (filled) and low-level reflectivity at (a) 2130 UTC (b) 2200 UTC (c) 2230 UTC……………………………………………72

Figure 4.15. Ensemble mean analysis lowest model level temperature in ^{o}C (filled) and low-level reflectivity (black contours) on 30 May 2013 at (a) 1900 UTC (b) 1930 UTC (c) 2000 UTC (d) 2030 UTC……………………………………………………...73

Figure 4.16. 30 May 2013 ensemble mean analysis lowest model level temperature difference in ^{o}C from 1900 UTC due to convection (filled) and low-level reflectivity at (a) 1930 UTC (b) 2000 UTC (c) 2030 UTC……………………………………………74

Figure 4.17. Ensemble mean analysis lowest model level temperature in ^{o}C (filled) and low-level reflectivity (black contours) on 31 May 2013 at (a) 2130 UTC (b) 2200 UTC (c) 2230 UTC (d) 2300 UTC……………………………………………………...75

Figure 4.18. 31 May 2013 ensemble mean analysis lowest model level temperature difference in ^{o}C from 2130 UTC due to convection (filled) and low-level reflectivity at (a) 2200 UTC (b) 2230 UTC (c) 2300 UTC……………………………………………76

Figure 4.19. Ensemble mean analysis 250 hPa wind speed (shaded) in m s^{-1} and wind barbs on 29 May 2013 at (a) 2100 UTC (b) 2130 UTC (c) 2200 UTC (d) 2230 UTC. The ensemble analysis cloud outline is denoted by the thick black line and is determined using the method described by Kerr et al. (2015)……………………………………...79

Figure 4.20. Ensemble mean analysis 250 hPa wind speed difference in m s^{-1} from 29 May 2100 UTC (filled) and cloud outline (thick black line) at (a) 2130 UTC (b) 2200 UTC (c) 2230 UTC…………………………………………………………………..80

Figure 4.21. Ensemble mean analysis 250 hPa wind speed (shaded) in m s^{-1} and wind barbs on 30 May 2013 at (a) 1900 UTC (b) 1930 UTC (c) 2000 UTC (d) 2030 UTC. The ensemble analysis cloud outline is denoted by the thick black line and is determined using the method described by Kerr et al. (2015)……………………………………...81

Figure 4.22. Ensemble mean analysis 250 hPa wind speed difference in m s^{-1} from 30 May 1900 UTC (filled) and cloud outline (thick black line) at (a) 1930 UTC (b) 2000 UTC (c) 2030 UTC…………………………………………………………………..82

Figure 4.23. Ensemble mean analysis 250 hPa wind speed (shaded) in m s^{-1} and wind barbs on 31 May at (a) 2130 UTC (b) 2200 UTC (c) 2230 UTC (d) 2300 UTC. The ensemble analysis cloud outline is denoted by the thick black line……………………83

Figure 4.24. Ensemble mean analysis 250 hPa wind speed difference in m s^{-1} from 31 May 2130 UTC (filled) and cloud outline (thick black line) at (a) 2200 UTC (b) 2230 UTC (c) 2300 UTC……………………………………………………………………..84

Figure 4.25. Ensemble mean analysis 250 hPa temperature in ^{o}C (shaded) and wind barbs on 29 May 2013 at (a) 2100 UTC (b) 2130 UTC (c) 2200 UTC (d) 2230 UTC. The ensemble analysis cloud outline is denoted by the thick black line……………….85

Figure 4.26. Ensemble mean analysis 250 hPa temperature difference in ^{o}C from 29 May 2100 UTC (filled) and cloud outline (thick black line) at (a) 2130 UTC (b) 2200 UTC (c) 2230 UTC……………………………………………………………………..86

Figure 4.27. Ensemble mean analysis 250 hPa temperature in ^{o}C and wind barbs on 30 May 2013 at (a) 1900 UTC (b) 1930 UTC (c) 2000 UTC (d) 2030 UTC. The ensemble analysis cloud outline is denoted by the thick black line………………………………87

Figure 4.28. Ensemble mean analysis 250 hPa temperature difference in ^{o}C from 30 May 1900 UTC (filled) and cloud outline (thick black line) at (a) 1930 UTC (b) 2000 UTC (c) 2030 UTC……………………………………………………………………..88

Figure 4.29. Ensemble mean analysis 250 hPa temperature in ^{o}C and wind barbs on 31 May at (a) 2130 UTC (b) 2200 UTC (c) 2230 UTC (d) 2300 UTC. The ensemble analysis cloud outline is denoted by the thick black line………………………………89

Figure 4.30. Ensemble mean analysis 250 hPa temperature difference in ^{o}C from 31 May 2130 UTC (filled) and cloud outline (thick black line) at (a) 2200 UTC (b) 2230 UTC (c) 2300 UTC……………………………………………………………………..90

Figure 5.1. 29 May target storm averaged composite reflectivity (> 20 dBZ) sensitivity to initial condition 850 hPa wind speed in dBZ (m s^{-1})$^{-1}$ and ensemble mean forecasted reflectivity (20 dBZ; black contour) and ensemble mean initial condition reflectivity (20 dBZ; gray contour) for forecast times (a) 1-hour, valid 2230 UTC (b) 1-hour with statistical significance test (c) 2-hour, valid 2330 UTC (d) 2-hour with statistical significance test……………………………………………………………………...96

Figure 5.2. 29 May target storm averaged composite reflectivity (> 20 dBZ) sensitivity to initial condition 850 hPa temperature in dBZ (^{o}C)$^{-1}$ and ensemble mean forecasted reflectivity (20 dBZ; black contour) and ensemble mean initial condition reflectivity (20 dBZ; gray contour) for forecast times (a) 1-hour, valid 2230 UTC (b) 1-hour with statistical significance test (c) 2-hour, valid 2330 UTC (d) 2-hour with statistical significance test……………………………………………………………………...97

Figure 5.3. 29 May target storm averaged composite reflectivity (> 20 dBZ) sensitivity to initial condition 850 hPa water vapor mixing ratio in dBZ (g kg^{-1})$^{-1}$ and ensemble mean forecasted reflectivity (20 dBZ; black contour) and ensemble mean initial condition reflectivity (20 dBZ; gray contour) for forecast times (a) 1-hour, valid 2230 UTC (b) 1-hour with statistical significance test (c) 2-hour, valid 2330 UTC (d) 2-hour with statistical significance test……………………………………………………...98

Figure 5.4. 29 May target storm averaged composite reflectivity (> 20 dBZ) sensitivity to initial condition SHR01 in dBZ (m s^{-1})$^{-1}$ and ensemble mean forecasted reflectivity (20 dBZ; black contour) and ensemble mean initial condition reflectivity (20 dBZ; gray contour) for forecast times (a) 1-hour, valid 2230 UTC (b) 1-hour with statistical significance test (c) 2-hour, valid 2330 UTC (d) 2-hour with statistical significance test……………………………………………………………………………..….99

Figure 5.5. 29 May target storm averaged composite reflectivity (> 20 dBZ) sensitivity to initial condition SHR03 in dBZ (m s^{-1})$^{-1}$ and ensemble mean forecasted reflectivity (20 dBZ; black contour) and ensemble mean initial condition reflectivity (20 dBZ; gray contour) for forecast times (a) 1-hour, valid 2230 UTC (b) 1-hour with statistical significance test (c) 2-hour, valid 2330 UTC (d) 2-hour with statistical significance test……………………………………………………………………………..100

Figure 5.6. 29 May target storm averaged LLW (> 10 m s^{-1}) sensitivity to initial condition SHR01 (unitless) and ensemble mean forecasted reflectivity (20 dBZ; black contour) and LLW (10 m s^{-1}; green contour) and ensemble mean initial condition reflectivity (20 dBZ; gray contour) for forecast times (a) 1-hour, valid 2230 UTC (b) 1-hour with statistical significance test (c) 2-hour, valid 2330 UTC (d) 2-hour with statistical significance test……………………………………………………………101

Figure 5.7. 29 May target storm averaged LLW (> 10 m s^{-1}) sensitivity to initial condition 850 hPa temperature in m s^{-1} (^{o}C)$^{-1}$ and ensemble mean forecasted reflectivity (20 dBZ; black contour) and ensemble mean initial condition reflectivity (20 dBZ; gray contour) and LLW (10 m s^{-1}; green contour) for forecast times (a) 1-hour, valid 2230 UTC (b) 1-hour with statistical significance test (c) 2-hour, valid 2330 UTC (d) 2-hour with statistical significance test…………………………………………………………102

Figure 5.8. 29 May target storm averaged LLW (> 10 m s^{-1}) sensitivity to initial condition 850 hPa water vapor mixing ratio in m s^{-1} (g kg^{-1})$^{-1}$ and ensemble mean forecasted reflectivity (20 dBZ; black contour) and LLW (10 m s^{-1}; green contour) and ensemble mean initial condition reflectivity (20 dBZ; gray contour) for forecast times (a) 1-hour, valid 2230 UTC (b) 1-hour with statistical significance test (c) 2-hour, valid 2330 UTC (d) 2-hour with statistical significance test………………………………..103

Figure 5.9. 30 May target storm averaged composite reflectivity (> 20 dBZ) sensitivity to initial condition 850 hPa water vapor mixing ratio in dBZ (g kg^{-1})$^{-1}$ and ensemble mean forecasted reflectivity (20 dBZ; black contour) and ensemble mean initial condition reflectivity (20 dBZ; gray contour) for forecast times (a) 30 minutes, valid 1930 UTC (b) 30 minutes with statistical significance test (c) 1-hour, valid 2000 UTC (d) 1-hour with statistical significance test……………………………………………106

Figure 5.10. 30 May target storm averaged composite reflectivity (> 20 dBZ) sensitivity to initial condition 700 hPa water vapor mixing ratio in dBZ (g kg^{-1})$^{-1}$ and ensemble mean forecasted reflectivity (20 dBZ; black contour) and ensemble mean initial condition reflectivity (20 dBZ; gray contour) for forecast times (a) 30 minutes, valid 1930 UTC (b) 30 minutes with statistical significance test (c) 1-hour, valid 2000 UTC (d) 1-hour with statistical significance test……………………………………………107

Figure 5.11. 30 May target storm averaged composite reflectivity (> 20 dBZ) sensitivity to initial condition CAPE in dBZ (10 J kg^{-1})$^{-1}$ and ensemble mean forecasted reflectivity (20 dBZ; black contour) for forecast times (a) 30 minutes, valid 1930 UTC (b) 30 minutes with statistical significance test (c) 1-hour, valid 2000 UTC (d) 1-hour with statistical significance test……………………………………………………….108

Figure 5.12. 30 May target storm averaged 2-5 km UH (> 5 m^2s^{-2}) sensitivity to initial condition SHR06 in m^2s^{-2} (m s^{-1})$^{-1}$ and ensemble mean forecasted reflectivity (20 dBZ; black contour) and 2-5 km UH (5 m^2s^{-2}; green contour) and ensemble mean initial condition reflectivity (20 dBZ; gray contour) for forecast times (a) 30 minutes, valid 1930 UTC (b) 30 minutes with statistical significance test (c) 1-hour, valid 2000 UTC (d) 1-hour with statistical significance test……………………………………………109

Figure 5.13. 30 May target storm averaged 2-5 km UH (> 5 m^2s^{-2}) sensitivity to initial condition 850 hPa wind speed in m^2s^{-2} (m s^{-1})$^{-1}$ and ensemble mean forecasted reflectivity (20 dBZ; black contour) and 2-5 km UH (5 m^2s^{-2}; green contour) and ensemble mean initial condition reflectivity (20 dBZ; gray contour) and ensemble mean initial condition reflectivity (20 dBZ; gray contour) for forecast times (a) 30 minutes, valid 1930 UTC (b) 30 minutes with statistical significance test (c) 1-hour, valid 2000 UTC (d) 1-hour with statistical significance test……………………………………...110

Figure 5.14. 30 May target storm averaged 2-5 km UH (> 5 m^2s^{-2}) sensitivity to initial condition 850 hPa temperature in m^2s^{-2} (^{o}C)$^{-1}$ and ensemble mean forecasted reflectivity (20 dBZ; black contour) and 2-5 km UH (5 m^2s^{-2}; green contour) and ensemble mean initial condition reflectivity (20 dBZ; gray contour) for forecast times (a) 30 minutes, valid 1930 UTC (b) 30 minutes with statistical significance test (c) 1-hour, valid 2000 UTC (d) 1-hour with statistical significance test……………………………………...111

Figure 5.15. 31 May target storm averaged composite reflectivity (> 20 dBZ) sensitivity to initial condition 850 hPa water vapor mixing ratio in dBZ (g kg^{-1})$^{-1}$ and ensemble mean forecasted reflectivity (20 dBZ; black contour) and ensemble mean initial condition reflectivity (20 dBZ; gray contour) for forecast times (a) 30 minutes, valid 2300 UTC (b) 30 minutes with statistical significance test (c) 1-hour, valid 2330 UTC (d) 1-hour with statistical significance test (e) 90 minutes, valid 0000 UTC, 01 June (f) 90 minutes with statistical significance test……………………………………………..115

Figure 5.16. 31 May target storm averaged composite reflectivity (> 20 dBZ) sensitivity to initial condition 700 hPa water vapor mixing ratio in dBZ (g kg^{-1})$^{-1}$ and ensemble mean forecasted reflectivity (20 dBZ; black contour) and ensemble mean initial condition reflectivity (20 dBZ; gray contour) for forecast times (a) 30 minutes, valid 2300 UTC (b) 30 minutes with statistical significance test (c) 1-hour, valid 2330 UTC (d) 1-hour with statistical significance test (e) 90 minutes, valid 0000 UTC, 01 June (f) 90 minutes with statistical significance test…………………………………………......116

Figure 5.17. 31 May target storm averaged composite reflectivity (> 20 dBZ) sensitivity to initial condition CAPE in dBZ (10 J kg^{-1})$^{-1}$ and ensemble mean forecasted reflectivity (20 dBZ; black contour) for forecast times (a) 1-hour, valid 2330 UTC (b) 1-hr with statistical significance test (c) 90 minutes, valid 0000 UTC, 01 June (d) 90 minutes with statistical significance test…………………………………………………………….117

Figure 5.18. 31 May target storm averaged accumulated rainfall (> 10 mm) sensitivity to initial condition 850 hPa water vapor mixing ratio in mm (g kg^{-1})$^{-1}$ and ensemble mean forecasted reflectivity (20 dBZ; black contour) and accumulated rainfall (10 mm; green contour) and ensemble mean initial condition reflectivity (20 dBZ; gray contour) for forecast times (a) 30 minutes, valid 2300 UTC (b) 30 minutes with statistical significance test (c) 1-hour, valid 2330 UTC (d) 1-hour with statistical significance test (e) 90 minutes, valid 0000 UTC, 01 June (f) 90 minutes with statistical significance test……………………………………………………………………………..118

Figure 5.19. 31 May target storm averaged accumulated rainfall (> 10 mm) sensitivity to initial condition 700 hPa water vapor mixing ratio in mm (g kg^{-1})$^{-1}$ and ensemble mean forecasted reflectivity (20 dBZ; black contour) and accumulated rainfall (10 mm; green contour) and ensemble mean initial condition reflectivity (20 dBZ; gray contour) for forecast times (a) 30 minutes, valid 2300 UTC (b) 30 minutes with statistical significance test (c) 1-hour, valid 2330 UTC (d) 1-hour with statistical significance test (e) 90 minutes, valid 0000 UTC, 01 June (f) 90 minutes with statistical significance test……………………………………………………………………………..119

Figure 5.20. 31 May target storm averaged 2-5 km UH (> 75 m^2s^{-2}) sensitivity to initial condition SHR06 in m^2s^{-2} (m s^{-1})$^{-1}$ and ensemble mean forecasted reflectivity (20 dBZ; black contour) and 2-5 km UH (75 m^2s^{-2}; green contour) and ensemble mean initial condition reflectivity (20 dBZ; gray contour) for forecast times (a) 30 minutes, valid 2300 UTC (b) 30 minutes with statistical significance test (c) 1-hour, valid 2330 UTC (d) 1-hour with statistical significance test (e) 90 minutes, valid 0000 UTC, 01 June (f) 90 minutes with statistical significance test……………………………………..120

Figure 5.21. 31 May target storm averaged 2-5 km UH (> 75 m^2s^{-2}) sensitivity to initial condition 850 hPa wind speed in m^2s^{-2} (m s^{-1})$^{-1}$ and ensemble mean forecasted reflectivity (20 dBZ; black contour) and 2-5 km UH (75 m^2s^{-2}; green contour) and ensemble mean initial condition reflectivity (20 dBZ; gray contour) for forecast times (a) 1-hour, valid 2330 UTC (b) 1-hour with statistical significance test (c) 90 minutes, valid 0000 UTC, 01 June (d) 90 minutes with statistical significance test…………...121

Figure 5.22. 31 May target storm averaged 2-5 km UH (> 75 m^2s^{-2}) sensitivity to initial condition 850 hPa temperature in m^2s^{-2} (^oC)$^{-1}$ and ensemble mean forecasted reflectivity (20 dBZ; black contour) and 2-5 km UH (75 m^2s^{-2}; green contour) and ensemble mean initial condition reflectivity (20 dBZ; gray contour) for forecast times (a) 1-hour, valid 2330 UTC (b) 1-hour with statistical significance test (c) 90 minutes, valid 0000 UTC, 01 June (d) 90 minutes with statistical significance test…………………………...122

Figure 5.23. 31 May target storm averaged 0-1 km UH (> 5 m^2s^{-2}) sensitivity to initial condition SHR01 in m^2s^{-2} (m s^{-1})$^{-1}$ and ensemble mean forecasted reflectivity (20 dBZ; black contour) and 0-1 km UH (5 m^2s^{-2}; green contour) and ensemble mean initial condition reflectivity (20 dBZ; gray contour) for forecast times (a) 30 minutes, valid 2300 UTC (b) 30 minutes with statistical significance test (c) 1-hour, valid 2330 UTC (d) 1-hour with statistical significance test. The black dot in (a) and (c) is the grid point for Fig. 5.24……………………………………………………………………...123

Figure 5.24. Scatter plots of initial condition SHR01 versus target storm forecasted average 0-1 UH (> 5 m^2s^{-2}) at black dot in Fig. 5.23 for forecast lead times (a) 30 minutes (b) 1-hour…………………………………………………………………124

Figure 5.25. Example scatterplots of initial condition water vapor mixing ratio (g kg^{-1}) and one-hour forecast reflectivity (dBZ; top); initial condition 0-6 km shear and one-hour forecast 2-5 km UH (m^2s^{-2}; bottom)…………………………………………..125

Figure 5.26. Schematic of storm-induced perturbation period followed by the forecast. In the 31 May case, the perturbation period spans 2130 – 2230 UTC………………..128

Figure 5.27. 30 May target storm averaged 2-5 km UH (> 5 m^2s^{-2}) sensitivity to initial one hour storm-induced change of SHR06 in m^2s^{-2} (m s^{-1})$^{-1}$ and ensemble mean forecasted reflectivity (20 dBZ; black contour) and 2-5 km UH (5 m^2s^{-2}; green contour) for forecast times (a) 30 minutes, valid 1930 UTC (b) 30 minutes with statistical significance test (c) 1-hour, valid 2000 UTC (d) 1-hour with statistical significance test (e) 90 minutes, valid 2030 UTC (f) 90 minutes with statistical significance test…….129

Figure 5.28. 31 May target storm averaged 2-5 km UH (> 75 m^2s^{-2}) sensitivity to initial one hour storm-induced change of SHR06 in m^2s^{-2} (m s^{-1})$^{-1}$ and ensemble mean forecasted reflectivity (20 dBZ; black contour) and 2-5 km UH (75 m^2s^{-2}; green contour) for forecast times (a) 30 minutes, valid 2300 UTC (b) 30 minutes with statistical significance test (c) 1-hour, valid 2300 UTC (d) 1-hour with statistical significance test (e) 90 minutes, valid 0000 UTC, 01 June (f) 90 minutes with statistical significance test……………………………………………………………………130

Figure 5.29. 31 May target storm averaged 0-1 km UH (> 5 m^2s^{-2}) sensitivity to initial one hour storm-induced change of SHR01 in m^2s^{-2} (m s^{-1})$^{-1}$ and ensemble mean forecasted reflectivity (20 dBZ; black contour) and 2-5 km UH (5 m^2s^{-2}; green contour) for forecast times (a) 30 minutes, valid 2300 UTC (b) 30 minutes with statistical significance test (c) 1-hour, valid 2300 UTC (d) 1-hour with statistical significance test (e) 90 minutes, valid 0000 UTC, 01 June (f) 90 minutes with statistical significance test………………………………………………………………………………..131

Figure 5.30. Idealized storm averaged 2-5 km UH with time for environments initialized with SHR06 of 27 m s^{-1} (red), 32 m s^{-1} (blue), 40 m s^{-1} (green)……………………...132

Abstract

The Mesoscale Predictability Experiment (MPEX) conducted during the spring of 2013 included frequent coordinated sampling of near-storm environments via upsondes. These unique observations were taken to better understand the upscale effects of deep convection on the environment, and are used to validate the accuracy of convection-allowing ($\Delta x = 3$ km) model ensemble analyses. A 36-member ensemble was created with physics diversity using the Weather Research and Forecasting model, and observations were assimilated via the Data Assimilation Research Testbed using an ensemble adjustment Kalman filter. A four-day sequence of convective events from 28-31 May 2013 in the south central United States was analyzed by assimilating Doppler radar and conventional observations. No MPEX upsonde observations were assimilated. Since the ensemble mean analyses produce an accurate depiction of the storms, the MPEX observations are used to verify the accuracy of the analyses of the near-storm environment.

The MPEX observations reveal modest analysis errors overall when considering all samples, although specific environmental regions reveal larger errors in some state fields. Since the environmental ensemble analyses have been thoroughly verified, convection-allowing models are used to assess the short-term (1-2 hours) impacts of convection on the surrounding environment. Convection evolution dependencies on the environment are assessed using the ensemble sensitivity technique. This includes forecast proxies for various hazards including tornadoes, hail, and damaging winds. Results suggest scenarios where environmental modifications by convection are significant in further convection evolution, supporting the notion of storm-environment feedbacks.

Chapter 1: Introduction

Multiple portions of this dissertation are direct excerpts published in the Kerr et al. (2017; © American Meteorological Society). This includes most of Chapters 1,2, and 3.

1.1 Background and motivation

Convection-allowing models (CAMs) can improve predictions of the organization and evolution of convection (e.g., Kain et al. 2006, 2008; Clark et al. 2010a,b). Reliable forecasts of deep convection are needed to improve warnings for associated high-impact meteorological phenomena (e.g., damaging winds, flash flooding, hail, tornadoes; Stensrud et al. 2009, 2013). The practical predictability of such events is largely dependent on having accurate initial conditions and small model error (Zhang et al. 2007; Cintineo and Stensrud 2013). Results from Cintineo and Stensrud (2013) suggest that convective environments must be well represented by the models to ensure reasonable forecast accuracy. Thus, one facet that must be well depicted is the impact of long-lived convection on the environment, i.e. upscale feedbacks. Proper depictions of these feedbacks should lead to better short-term forecasts. The largest hindrance to evaluating the accuracy of model analyses of near-storm environments is the lack of sufficient observations to perform such studies.

The Mesoscale Predictability Experiment (MPEX) included frequent, coordinated sampling of near-storm environments from 15 May – 15 June 2013 across the Great Plains of the United States using radiosondes (also called upsondes or sondes) (Weisman et al. 2015; Trapp et al. 2016; Hitchcock et al. 2016). One goal of MPEX was to observe short-term storm-induced changes in the environment via upsondes.

These upsondes provided vertical profiles of temperature, humidity, pressure, and zonal and meridional wind components at a variety of locations near areas of deep convection and thus should have sampled the upscale feedbacks from convection on the nearby mesoscale environment. While many previous studies have demonstrated the impacts of deep convection on the surrounding environment through either model simulations (e.g., Maddox 1980; Fritsch and Maddox 1981b; Brooks et al. 1994; Stensrud 1996; Stensrud and Anderson 2001) or observations (e.g., Fritsch and Maddox 1981a; Parker 2014), the number of near-storm environment observations has been limited, causing extensive verification to be neglected.

Mesoscale convective systems (MCSs) are known to be a cause of upper-tropospheric meso-alpha-scale anticyclones (Ninomiya 1971a,b; Maddox 1980; Fritsch and Maddox 1981; Anabor et al. 2009; Trier and Sharman 2009; Metz and Bosart 2010). With these anticyclones, 200 hPa winds and geopotential heights can be perturbed by over 20 m s^{-1} and 80 m, respectively (Leary 1979; Fritsch and Maddox 1981; Perkey and Maddox 1985; Smull and Augustine 1993). These perturbations often are observed relatively soon after the convective event (6-24 h; Weisman et al. 2015). Jet-streaks have also been shown to be enhanced due to the presence of MCSs (Keyser and Johnson 1984; Wolf and Johnson 1995a,b). Simulated supercells increase storm-relative environmental helicity (SREH) and convective available potential energy (CAPE) within convective inflow-regions (Brooks et al. 1994). Low-level inflow to deep convection also increases if the convection is persistent (Stensrud 1996).

Although many studies have described the impacts of deep convection on the large-scale environment, few have focused on nearby mesoscale environmental impacts and the accuracy of numerical weather models' depictions of these alterations. While CAMs can successfully simulate the structure of convection via radar data assimilation (e.g., Snyder and Zhang 2003; Dowell et al. 2004; Yossouf et al. 2013, 2015; Johnson et al. 2015), it is unknown whether or not radar data assimilation with a CAM provides sufficient information for storm-scale model analyses to reasonably represent the changes in the near-storm environment from convective feedbacks. Using upsonde observations collected from near-storm environments during MPEX, a more complete evaluation of model ensemble analysis accuracy within the environments surrounding deep convection is performed. This evaluation is done in order to assess whether the numerical model's depiction of the environments influenced by convection is reasonable. This evaluation will further reveal any systematic biases and model errors within the convectively perturbed environment that could influence subsequent predictions of convective evolution.

Once verified as previously stated, ensemble analyses will be used to analyze the impacts of convection on the surrounding mesoscale environment in the low-, mid-, and upper-troposphere. These storm-induced environmental changes may have significant effects on further convection predictability. Dependencies of convection evolution on the surrounding environment will be evaluated using an ensemble sensitivity technique (Torn and Hakim 2008). Convection evolution may also be dependent on the environmental modifications described previously. The broader understanding of storm-environment relationships that are the focus of this study will ultimately improve short-term predictability of potentially hazardous convective events such as tornadoes, hail, and flash flooding.

1.2. MPEX upsonde operations and convective events

The observational foundation of this research comes from the special MPEX upsonde observations. Four mobile upsonde units operated during MPEX to sample pre-convective (PDE strategy) and near-storm environments that were convectively disturbed (CDE; Weisman et al. 2015; Trapp et al. 2016). These units were from the National Severe Storms Laboratory (NSSL), Purdue University, Colorado State University (CSU), and Texas A&M University (TAMU). NSSL, Purdue, and TAMU used radiosondes manufactured by International Met Systems (iMet) while CSU made use of Vaisala radiosondes. The differences in observation error and data quality between these two radiosonde systems are negligible (Trapp et al. 2016). Sondes were carried by 200 gram latex balloons that could ascend above the tropopause, having maximum flight times of approximately one hour. During CDE sampling, observations were collected in convective inflow, convective outflow, and anvil regions among others.

The four convective events highlighted in this study occurred from 28 – 31 May 2013 in portions of Texas, Oklahoma, and Kansas. Forcing for convection initiation generally stemmed from drylines, with modest large-scale forcing resulting from a cyclonic vorticity maximum ejecting into the central US. All four MPEX upsonde units targeted a diminishing thunderstorm cluster in the Oklahoma Panhandle moving into southern Kansas on 28 May. The units predominantly sampled the downstream environment at fixed locations, beginning at 2000 UTC in a rectangular formation, to measure environmental changes as convection approached their locations (Fig. 1.1a). The final sonde was released around 0030 UTC 29 May. An example of simultaneously released upsonde profiles show how a realistic convective environment can vary over short distances (< 150 km; Fig. 1.2). The NSSL and TAMU launches were approximately 115 km apart, but TAMU observed a stout capping inversion while NSSL – located closer to the dryline - did not. The following day (29 May) featured a developing squall line in the Texas Panhandle that eventually translated into western Oklahoma. Upsondes were released in the wake of the squall line and sampled the environment around a bookend vortex on the convective line's northern edge (Fig. 1.1b). Deployments shifted to central Oklahoma for 30 and 31 May, where supercell thunderstorms were targeted. The inflow region of a nontornadic supercell was sampled every 30 minutes for several hours on 30 May by NSSL, while the three other units sampled the convective wake and environment to the north of this predominately eastward moving supercell (Fig. 1.1c). NSSL, Purdue, and CSU sampled the tornadic supercell that produced a large tornado near El Reno, Oklahoma on 31 May (Bluestein et al. 2015). As in the previous day, both inflow and wake regions were sampled frequently (Fig. 1.1d).

Over this four-day period, a total of 81 upsondes were released. It should be noted that some upsondes did not ascend very far above 600 hPa after release for a variety of reasons (interference with convection, balloon burst, etc.), so only the profiles below upsonde termination are used for verification. Manual quality control also was applied to the entire upsonde data set. The estimated accuracies of the upsonde observations are 0.5 K for temperature, 5% for relative humidity, 1 m s^{-1} for the zonal and meridional wind components, and 1 hPa for pressure between the surface and tropopause.

The next chapter outlines the various methodologies used within this volume. Chapter 3 presents the results of near-storm environment verification using MPEX upsonde observations (Kerr et al. 2017). Chapter 4 quantifies select environmental modifications by convection. Chapter 5 assesses the sensitivity of convection evolution to environmental features.

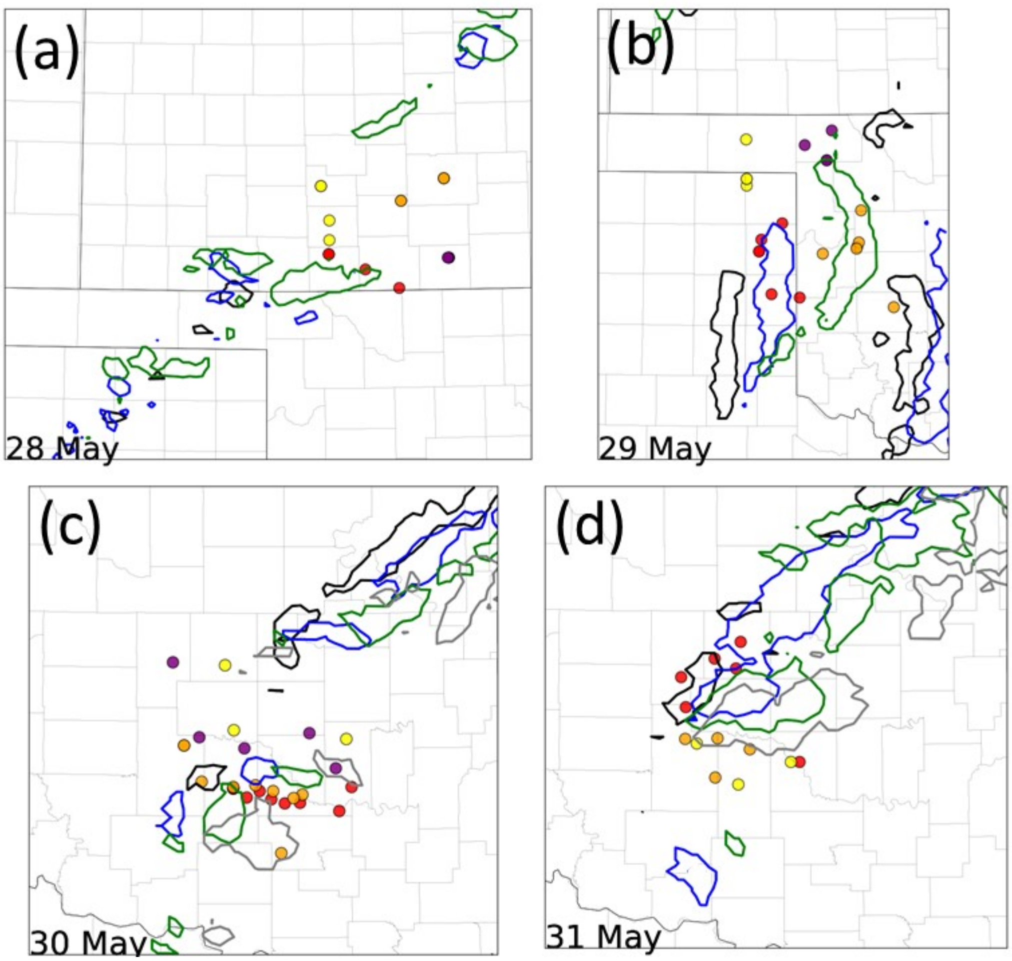

Figure 1.1. Hourly observed reflectivity 30 dBZ contours for (a) 28 May 2100 UTC (black), 2200 UTC (blue), and 2300 UTC (green), (b) 29 May 2100 UTC (black), 2200 UTC (blue), and 2300 UTC (green), (c) 30 May 1900 UTC (black), 2000 UTC (blue), 2100 UTC (green), and 2200 UTC (gray), (d) 31 May 2200 UTC (black), 2300 UTC (blue), 1 June 0000 UTC (green), 0100 UTC (gray). MPEX upsonde releases are denoted with circles (NSSL-red, Purdue-orange, CSU-yellow, TAMU-purple).

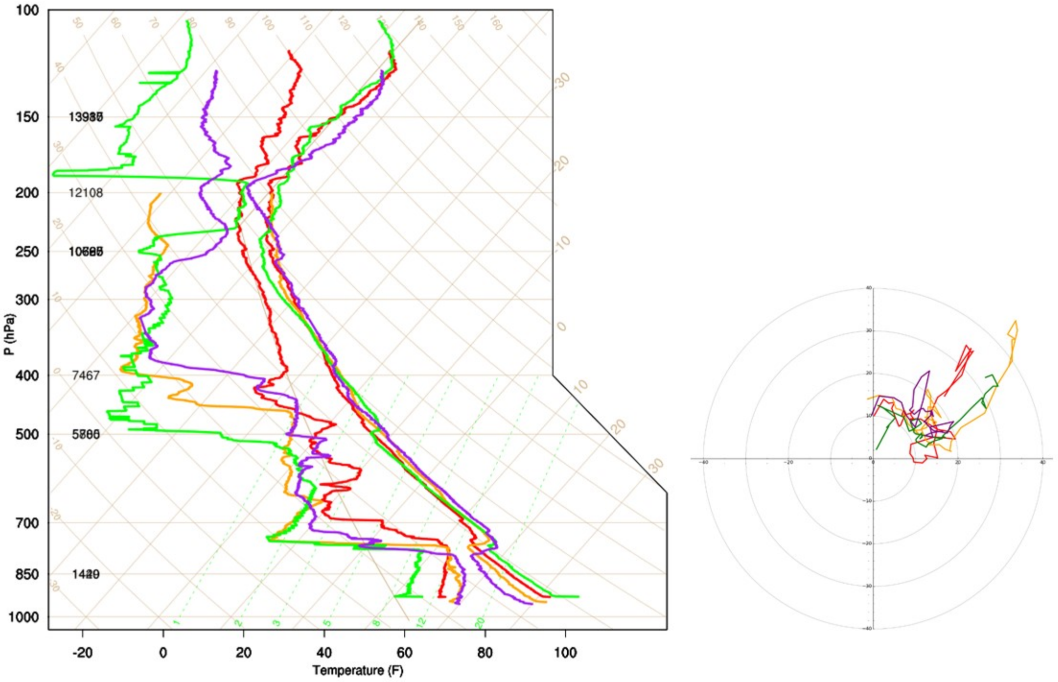

Figure 1.2. 2100 UTC 28 May MPEX sounding skew-T thermodynamic profiles and hodographs with NSSL (red), Purdue (orange), CSU (green), and TAMU (purple).

Chapter 2: Methodology

The four-day sequence chosen is simulated using the Advanced Research version of the Weather Research and Forecasting model (WRF-ARW) version 3.4.1 (Skamarock et al. 2008). A nested domain is placed over portions of Texas, Oklahoma, and Kansas in order to encompass all targeted convection during the 28 – 31 May period. This inner domain has a horizontal grid spacing of 3 km while the outer domain (CONUS) has a grid spacing of 15 km (Fig. 2.1). Both domains used 51 vertical layers from the surface to 10 hPa. The NSSL Experimental Warn-on-Forecast (WoF) System for ensembles (NEWS-e) is utilized (Wheatley et al. 2015; Jones et al. 2016). This 36-member ensemble is initialized at 0000 UTC each respective day using a downscaled 21-member Global Ensemble Forecast System (GEFS). The boundary conditions for the outer domain are also created using the GEFS. The outer domain serves as the boundary conditions for the inner domain.

Ensemble members are developed following Wheatley et al. (2015) using a combination of 18 GEFS members and 18 physics combinations of planetary boundary layer (PBL), long- and short-wave radiation, and convective (outer domain only) parameterization schemes (Table 2.1). Members 1-18 are initialized with the corresponding GEFS member (member 1 with GEFS member 1, member 2 with GEFS member 2, etc.) and are run with the corresponding numerical physics combination from Table 2.1. Members 19-36 are initialized with the same 18 GEFS members in descending order (member 19 with GEFS member 18, member 20 with GEFS member 17, etc.) while running the physics combinations in ascending order (member 19 with combination 1, member 20 with combination 2, etc.) All ensemble members use the

Thompson et al. (2008) microphysics scheme. Since there are only 18 unique initial conditions at 0000 UTC (due to only 18 GEFS members), the model is integrated one hour forward to 0100 UTC each day to create 36 unique initial conditions.

Member	PBL	SW Radiation	LW Radiation	Cumulus
1	YSU	Dudhia	RRTM	Kain-Fritsch
2	YSU	RRTMG	RRTMG	Kain-Fritsch
3	MYJ	Dudhia	RRTM	Kain-Fritsch
4	MYJ	RRTMG	RRTMG	Kain-Fritsch
5	MYNN	Dudhia	RRTM	Kain-Fritsch
6	MYNN	RRTMG	RRTMG	Kain-Fritsch
7	YSU	Dudhia	RRTM	Grell
8	YSU	RRTMG	RRTMG	Grell
9	MYJ	Dudhia	RRTM	Grell
10	MYJ	RRTMG	RRTMG	Grell
11	MYNN	Dudhia	RRTM	Grell
12	MYNN	RRTMG	RRTMG	Grell
13	YSU	Dudhia	RRTM	Tiedtke
14	YSU	RRTMG	RRTMG	Tiedtke
15	MYJ	Dudhia	RRTM	Tiedtke
16	MYJ	RRTMG	RRTMG	Tiedtke
17	MYNN	Dudhia	RRTM	Tiedtke
18	MYNN	RRTMG	RRTMG	Tiedtke

Table 2.1. Physics options applied to 18 GEFS members. This set of physics options also is applied to these same 18 GEFS members in reverse order to create members 19-36 (for example, member 19 is initialized with GEFS member 18 but has physics option 1 applied). The Thompson microphysics and RAP land surface parameterization is applied to all members. PBL schemes include the Yonsei University (YSU), Mellor–Yamada–Janjic (MYJ), and Mellor–Yamada–Nakanishi–Niino (MYNN) schemes. Shortwave (SW) and longwave (LW) radiation schemes include the Dudhia shortwave scheme, Rapid Radiative Transfer Model (RRTM) shortwave scheme, and the Rapid Radiative Transfer Model–Global (RRTMG) shortwave and longwave schemes (adapted from Wheatley et al. 2015)

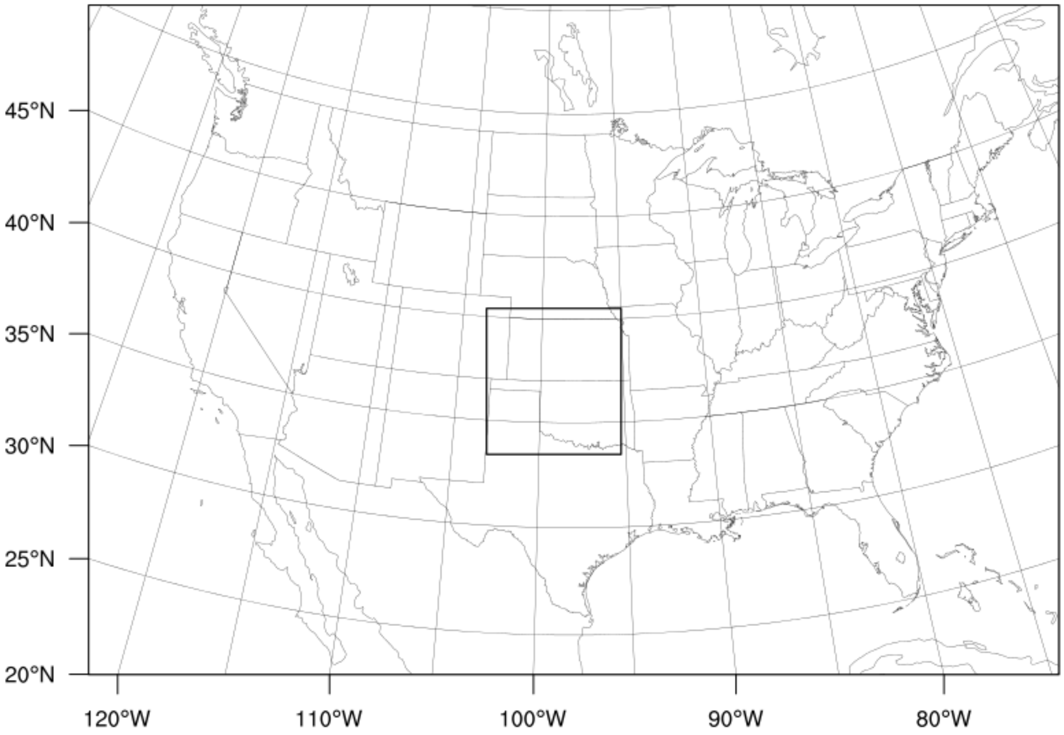

Figure 2.1. Outer model domain (CONUS; 15 km grid spacing) and nested, convection-resolving domain (3 km grid spacing) which includes KS, OK, and the TX Panhandle.

2.1 Mesoscale data assimilation

Hourly cycles of mesoscale data assimilation begin at 0100 UTC, when the first analysis is created. Conventional observations of temperature, dewpoint, pressure, and zonal and meridional wind components, provided by the NOAA Meteorological Assimilation Data Ingest System (MADIS), are assimilated using an ensemble adjustment Kalman filter (EAKF) available via the Data Assimilation Research Testbed (DART; Anderson 2001; Anderson et al. 2009). These observations platforms include METAR and marine surface stations, the Aircraft Communications Addressing and Reporting System (ACARS), and rawinsondes along with data from MADIS mesonet and the Oklahoma Mesonet. The MPEX upsonde observations are not assimilated.

The Gaspari and Cohn (1999) Gaussian-like localization function is utilized for all observations assimilated. The horizontal localization cutoff for non-mesonet mesoscale observations is approximately 458 km with a vertical localization cutoff of 8 km [consistent with Wheatley et al. (2012, 2015)]. Mesonet observations have a horizontal localization of approximately 60 km [consistent with Sobash and Stensrud (2015), Wheatley et al. (2015), and Jones et al. (2016)]. Ensemble spread is maintained using spatial and temporal prior adaptive inflation (Anderson 2007).

2.2 Storm-scale data assimilation

At a predetermined time based on each day's convective event (Table 2.2), storm-scale data assimilation begins. Level II radar data (radar reflectivity and radial velocity; radars for each event listed in Table 2.2) are assimilated every 15 minutes along with MADIS mesonet, Oklahoma Mesonet, and conventional rawinsonde observations. As with the outer domain, no MPEX observations are assimilated. The horizontal localization cutoff for radar observations is 18 km with a 6 km vertical cutoff (Yussouf et al. 2013; Wheatley et al. 2014, 2015; Jones et al. 2016). Surface and conventional rawinsonde observations retain the identical localization specifications as used in mesoscale data assimilation. This assimilation only updates the inner domain as the parent domain continues to serve as lateral boundary conditions without update from data assimilation. Radar reflectivity observations less than 10 dBZ are considered clear-air reflectivity observations and set to 0 dBZ (Wheatley et al. 2015). Radial velocity observations are only assimilated if they are collocated with reflectivity observations exceeding or equal to 20 dBZ.

After quality control of radar observations, the data are objectively analyzed to a 6-km Cartesian grid using the Cressman scheme (Cressman 1959) via the Observation Processing and Wind Synthesis (OPAWS; Majcen et al. 2008) software. Radar observations collected within a 15-minute window centered on the analysis time are assimilated. Observation errors of 5 dBZ for radar reflectivity and 3 m s^{-1} for radial velocity are assumed uniform and constant throughout each experiment (Dowell et al. 2004; Aksoy et al. 2009; Yussouf et al. 2013, Wheatley et al. 2015; Jones et al. 2016). Convection spin-up is induced by the additive noise technique developed by Dowell and Wicker (2009). Perturbations are added to the temperature, dewpoint, and horizontal wind fields in each member at locations where the reflectivity innovations are >10 dBZ and reflectivity observations are >25 dBZ (Sobash and Wicker 2015).

The 15-minute storm-scale data assimilation cycling continues until a predetermined ending time that is unique to each experiment (Table 2.2). The ending times are based on the end of MPEX upsonde operations. High-resolution (Δx = 3 km) ensemble analyses are thus available every 15 minutes from convection initiation to the end of MPEX operations for each of the four cases. MPEX upsonde observations are windowed to the closest 15-minute analysis time to the upsonde release time. All observations collected by each sonde are considered valid at this analysis time. Ensemble sounding profiles are created for each MPEX upsonde by linearly interpolating the ensemble analysis output to the horizontal sonde location at logarithmically interpolated 25 hPa vertical increments. Windowing each observation throughout the flight did not result in statistically significant differences (not shown).

Date	Event	Radars	Start Time	End Time	Upsondes
28 May	Oklahoma Panhandle; southern Kansas thunderstorm cluster	KDDC, KICT, KAMA, KVNX	1900 UTC	0200 UTC (29 May)	18
29 May	Texas Panhandle; western Oklahoma bow echo and bookend vortex	KAMA, KFDR, KDDC, KVNX	1700 UTC	2345 UTC	20
30 May	Central Oklahoma non-tornadic supercell	KTLX, KFDR	1700 UTC	2300 UTC	28
31 May	Central Oklahoma tornadic supercell	KTLX, KFDR, KVNX	2100 UTC	0230 UTC (01 June)	15

Table 2.2. Description of the convective events each day. The start and end times of radar data assimilation are listed with the corresponding radars that collected the data including Dodge City, KS (KDDC), Amarillo, TX (KAMA), Vance Air Force Base, OK (KVNX), Wichita, KS (KICT), Oklahoma City, OK (KTLX), and Frederick, OK (KFDR). The number of MPEX upsondes released during each event are listed last.

2.3 Convective perturbation technique

Severe storms often form in environments with strong horizontal gradients and rapid temporal changes in vertical wind shear and instability (Cortinas and Stensrud 1995; Wagner et al. 2008; Kerr et al. 2017). Thus, it is important to separate the evolution of the environment from any changes attributable to convective feedbacks. A method is developed to discern whether short-term changes in the environment are convectively induced or not.

As discussed earlier, the forecasts are produced on an outer domain with parameterized convection, and inner domain analyses are created with explicit convection via the Thompson microphysics scheme. An investigation of the outer domain forecasts shows that parameterized convection did not occur in the regions targeted during MPEX. This situation suggests that the outer domain forecast can be used to quantify the environmental changes not linked to deep convection. For the inner domain, environmental changes with time include both convectively-induced changes as well as other environmental changes. Thus, using the changes on both the inner and outer domain, the environmental impacts by convection are revealed by subtracting the changes on the outer domain from these on the inner domain. This difference represents the short-term changes in the near-storm environment induced by convection.

To calculate the difference fields, temporal changes in the outer domain model state are first linearly interpolated in the horizontal to the $\Delta x = 3$ km grid points on the inner domain, and this downscaled outer domain is then subtracted from the inner, convection-allowing domain change of the same variable. The difference reveals environmental variables that have been altered by nearby convection. Fig. 2.2 displays an example of the outer and inner domain 0-6 km vertical wind shear change over a one hour period and the difference between these two (inner – outer) which reveals impacts by convection on the surrounding shear field.

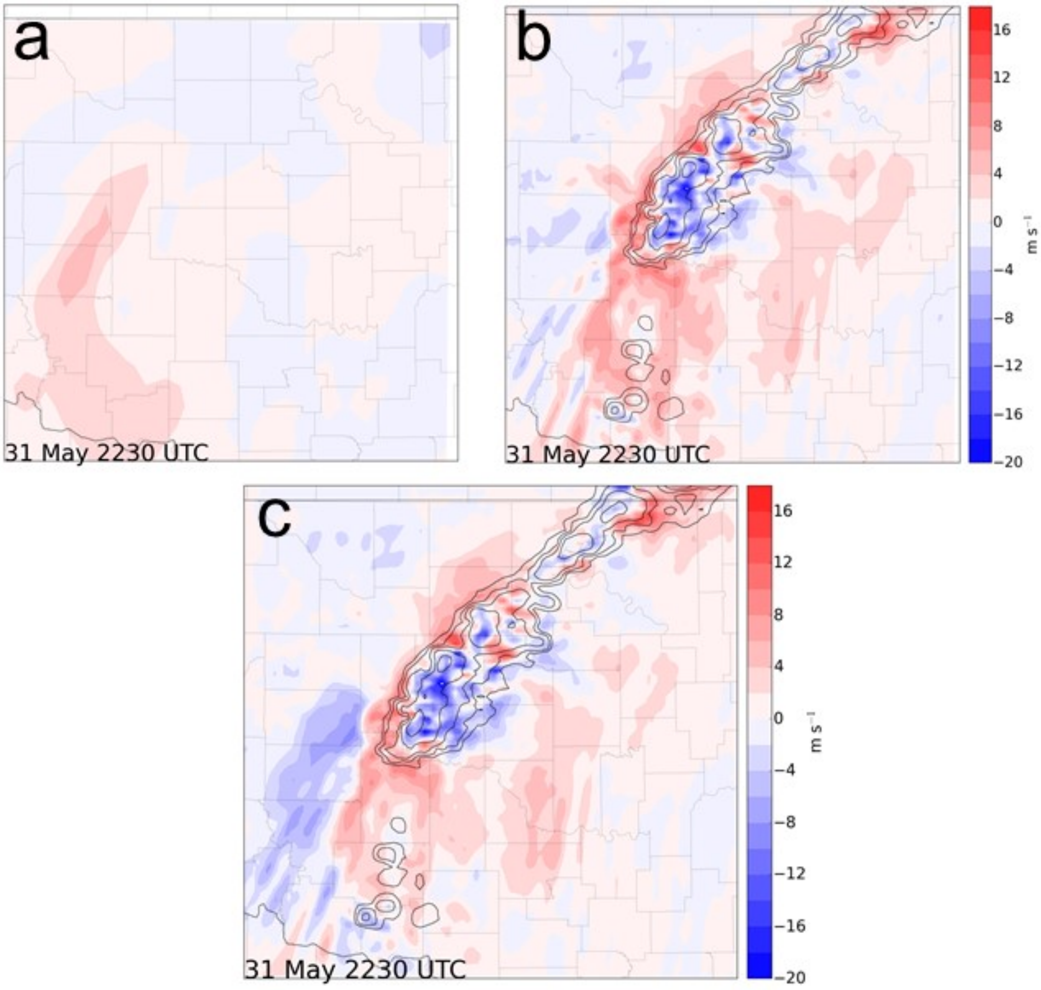

Figure 2.2. One hour changes in ensemble mean analysis 0-6 km vertical wind shear from 2130 – 2230 UTC on 31 May 2013 (filled) and low-level reflectivity analysis (black contours), (a) mesoscale domain (b) storm-scale domain (c) difference between mesoscale and storm-scale domain, revealing changes induced by convection.

2.4 Ensemble sensitivity analysis

Ensemble sensitivity analysis (ESA) is a technique that uses a group of ensemble forecasts to reveal dependencies of forecast metrics on variables (same or different) at an earlier time, including initial conditions from which the forecasts are initialized (Ancell and Hakim 2007; Hakim and Torn 2008; Torn and Hakim 2008). This method is a simple linear regression derived from the response of a given scalar forecast metric to an initial condition variable. The sensitivity is defined by

$$\frac{\partial J}{\partial x} = \frac{cov(J, x)}{var(x)}$$

where *J* is a scalar forecast metric, *x* is an initial condition variable, and *cov* and *var* are the covariance and variance of the given variables, respectively.

One advantage of ESA is that it is computationally inexpensive compared to adjoint sensitivity (LeDimet and Talagrand 1986). ESA has been thoroughly applied to synoptic-scale phenomena including mid-latitude cyclones (Ancell ad Hakim 2007; Torn and Hakim 2008; Garcies and Homar 2009, 2010; Torn and Hakim 2009; Chang et al. 2013; McMurdie and Ancell 2014) and tropical cyclones (Torn 2010; Ito and Wu 2013; Torn and Cook 2013; Xie et al. 2013; Torn 2014). Fig. 2.3 is adapted from Torn and Hakim (2008) and shows sensitivities of 24-hour forecast mean sea-level pressure (MSLP) within a designated response region, in this case western Washington State, to initial condition MSLP. From these results, it is apparent that higher initial condition MSLP over the Pacific Ocean in regions of positive sensitivity will result in higher average MSLP within the response region in a 24-hour forecast. Torn and Hakim (2008) test this method by inserting or denying observations for assimilation. This technique successfully verifies the ESA results.

ESA has recently been applied on the mesoscale to examine sensitivities in convection forecasts (Bednarczyk and Ancell 2015; Torn and Romine 2015; Weisman et al. 2015; Hill et al. 2016; Romine et al. 2016). In these studies, ESA is applied to spatially averaged convection-related variables, such as reflectivity, vertical velocity, and precipitation. Bednarczyk and Ancell (2015) and Hill et al. (2016) show convection to be sensitive to upstream, synoptic-scale features in both the upper and lower troposphere. Torn and Romine (2015), Weisman et al. (2015), and Romine et al. (2016) use ESA in cases during MPEX where dropsonde observations were targeted in regions of high sensitivity. Results from Romine et al. (2016) suggest targeted observations of upstream features can help improve convection forecasts in the 12-24 hour range.

2.4.1 ESA on the storm-scale

This study applies ESA to short-term (1-2 hour) forecasts of individual thunderstorms on 29, 30 and 31 May 2013. ESA must be applied to very short-term forecasts in order for relationships between initial condition variables and forecast metrics to have somewhat of a linear relationship. Applying ESA to longer-term forecasts, say 3-6 hours, of individual storms would not yield meaningful results and the linear assumption would fail. The sensitivity of storm-related forecast metrics, including storm averaged reflectivity and updraft helicity (UH), to environmental initial condition variables, including moisture and vertical wind shear, is investigated. UH is a measure of updraft rotation defined by

$$UH = \int_{z_0}^{z_t} w\zeta dz$$

where w is updraft velocity, ζ is the vertical component of relative vorticity, and z_t and z_0 are heights (Kain et al. 2008). Since environmental features that will affect convection evolution on the time scale of 1-2 hours are generally in close proximity to convective storms (< 100 km), a localization radius is placed centered on the main updraft of the supercell cases of 30 May and 31 May *only*. Localization is not applied to the 29 May case since the convective system is of larger scale. Localization removes distant spurious sensitivities that can arise due to ensemble sampling error, a common issue in ensemble data assimilation and forecasting (e.g., Wheatley et al. 2015; Jones et al. 2016; Kerr et al. 2017).

2.4.2 ESA statistical significance testing

To counteract potential ensemble sampling error, a statistical significance test, specifically a one-sample *t*-test that reveals the standard error-slope ratio, is applied to remove sensitivities that are statistically insignificant. This test is applied to the estimate of the sample distribution regression slope coefficient with a 95% confidence interval (p-value < 0.05; Wilks 2011, section 7.2.5). If a regression slope has a p-value < 0.05, there is a < 5% chance the observed effect in the sample is consistent with the null hypothesis meaning one can reject the null hypothesis that changes to an initial condition do not affect a forecast metric. Results suggest that when a relationship between an initial condition variable and forecast metric is highly nonlinear, the sensitivity will likely not pass the significance test since the standard error-slope ratio is too large. Example scatterplots illustrate statistically significant and insignificant sensitivities (Fig. 2.4). Statistically significant sensitivities are represented by a notable regression slope, whereas insignificant regression slopes are small in magnitude. This test can be imperfect, where sensitivities representing known physical variable relationships may be deemed insignificant even if changes in the initial condition would affect the forecast metric. Therefore, ESAs are shown with both the significance test applied and not applied without a localization radius in Chapter 5.

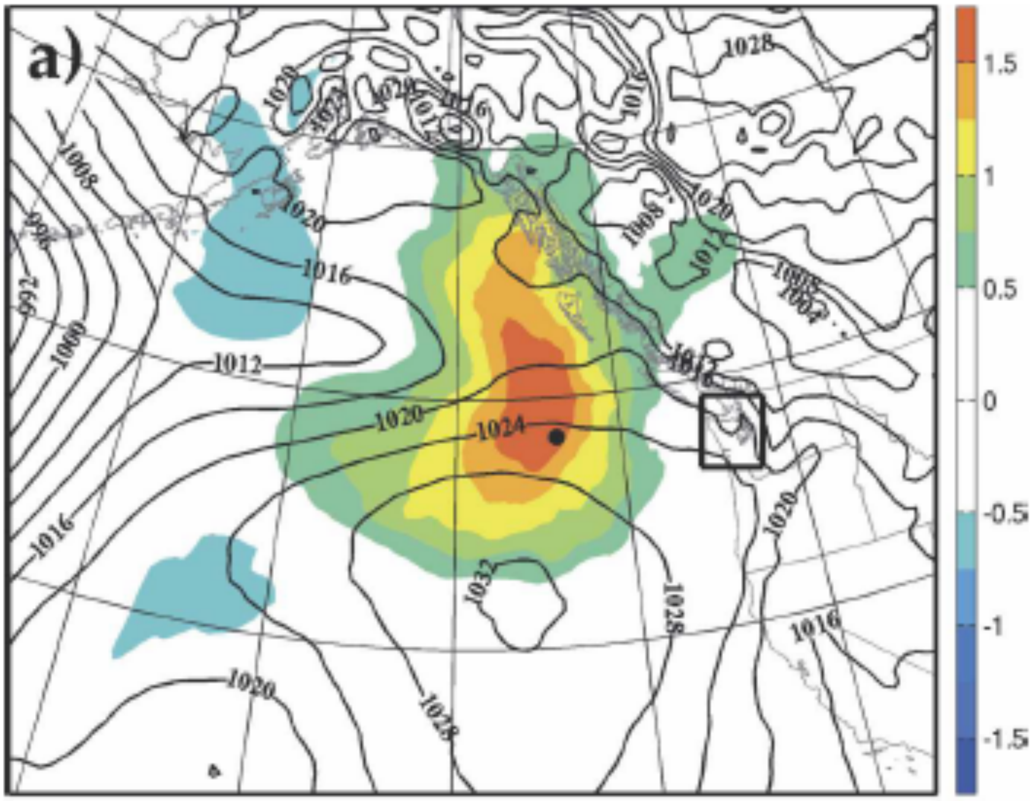

Figure 2.3. 24-hour average forecasted MSLP (within box) sensitivity to initial condition MSLP (adapted from Torn and Hakim 2008).

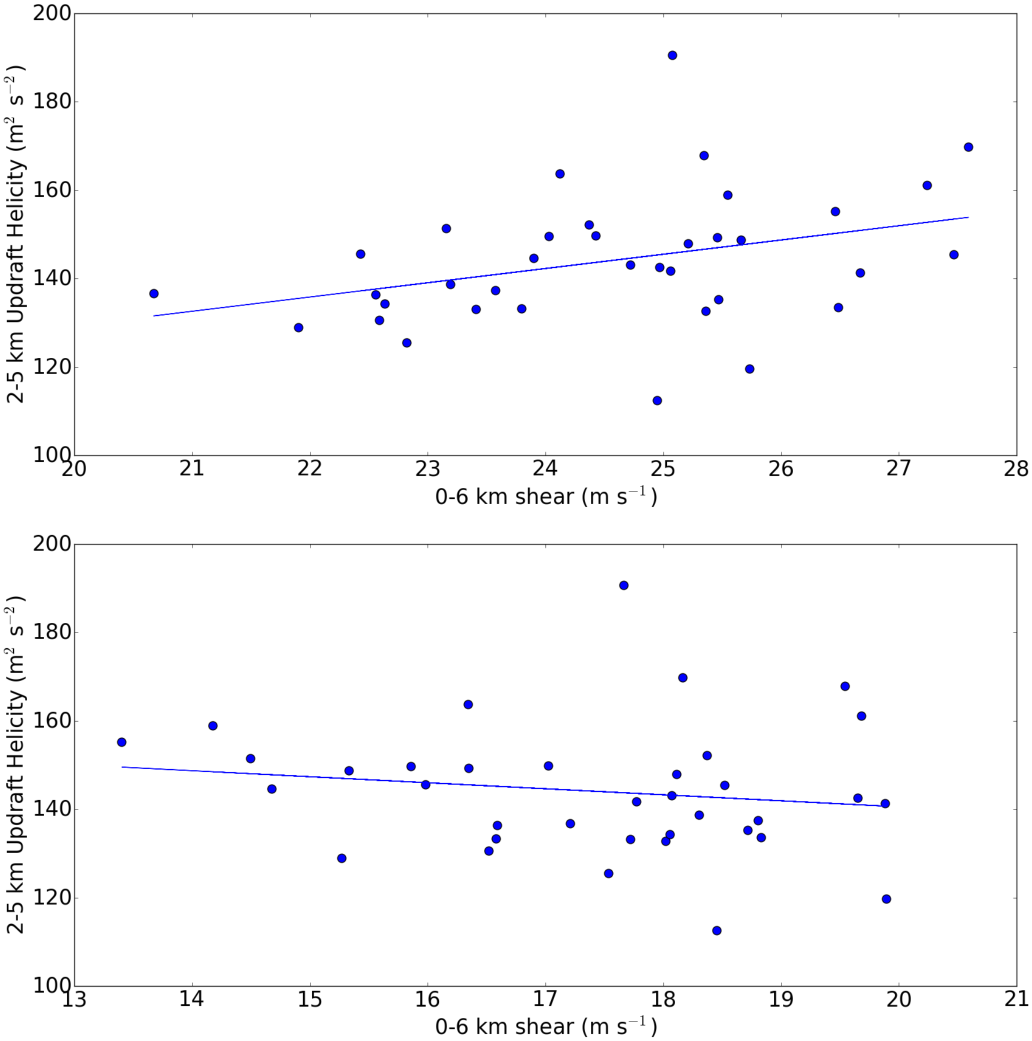

Figure 2.4. Example scatterplots of ensemble initial condition 0-6 km shear (m s^{-1}) and forecast 2-5 km UH (m^2s^{-2}) for a statistically significant sensitivity (top) and statistically insignificant sensitivity (bottom). The regression slope is more pronounced in the significant case (slope: 3.2, standard error: 1.5) than in the insignificant case (slope: 1.4 (abs), standard error: 1.5).

Chapter 3: Verification of ensemble near-storm environment analyses and forecasts

A subjective evaluation of the analyses rendered with radar data assimilation indicate that the 15-min ensemble mean analyses reproduce the structures of supercells, squall lines, and other convective features as seen in earlier studies (Snyder and Zhang 2003; Dowell et al. 2004; Tong and Xue 2005; Aksoy et al. 2009, 2010; Yussouf and Stensrud 2010). The ensemble mean reflectivity analyses show that the depictions of the targeted convection on each day compare reasonably to reflectivity observations (Figs. 3.1a-d). Further evidence of radar data assimilation effectiveness is shown by the root-mean-square error (RMSE) and total ensemble spread from 28 May (Fig. 3.1e,f), which illustrate how radial velocity and reflectivity assimilation has positive impacts on ensemble mean analyses. Similar behaviors are seen in the other three cases and indicate that the ensemble data assimilation system is producing a reasonable analysis of the ongoing convection.

3.1 Near-storm environment analysis errors

The ensemble mean analyses of the near-storm environment are evaluated using diagnostics with the special MPEX observations of temperature, relative humidity, zonal and meridional wind components. Vertical profiles of the root-mean-square difference (RMSD) are calculated using samples over the four-day period and is defined as

$$RMSD = \sqrt{\frac{1}{N}\sum_{n=1}^{N}(x_a^n - x_o^n)^2}$$

where x_a^n is the ensemble mean analysis, x_o^n is observation, and *N* is the number of observations collected at the respective pressure level over the four-day period. Mean ensemble spread (MES) is defined as

$$MES = \frac{1}{N}\sum_{n=1}^{N}\sqrt{\sigma_{obs}^2 + \frac{1}{35}\sum_{i=1}^{36}(\overline{x_a} - x_{ia})^2}$$

where *i* is ensemble member, σ_{obs}^2 is observation error variance, $\overline{x_a}$ is ensemble mean analysis, x_{ia} is ensemble member analysis, and *N* is the number of observations. Another diagnostic is mean bias of the analyses (MB), defined as

$$MB = \frac{1}{N}\sum_{n=1}^{N}(x_a^n - x_o^n)$$

where x_a^n, x_o^n, and *N* are previously defined.

The pressure-dependent sample size (Fig. 3.2a) has a magnitude of 81 between 925 and 850 hPa. The sample size generally decreases with height due to a variety of sonde and/or balloon failures. At 500 hPa, the sample size is 70. The sample size continues to decrease, reaching only 11 at 100 hPa. As previously stated, upsondes were released in a variety of regions surrounding the targeted convection including inflow, anvil, and outflow. Inflow soundings are designated as those released in areas where ground-relative low-level winds are directed into the region of convection. Anvil regions are areas under upper-level cloud produced by convection, including instances where inflow soundings sampled the storm anvil in upper-levels. Outflow environments are mainly confined to upstream (relative to storm motion) cold pool regions along with surging outflow ahead of convective cells. The upsonde counts for individual regions within the near-storm environments (Figs. 3.2) show a modest sample size for inflow and outflow regions (17 and 15 upsondes, respectively). A majority of upsondes were released within anvil regions (56 upsondes).

The RMSD of ensemble mean temperature for all 81 samples (Fig. 3.3a) reveals a local maximum just below 850 hPa of approximately 2 K. While the MB (Fig. 3.3b) does not show a local maximum at this height, the MES below 850 hPa exceeds 6 K. Inspection of individual soundings suggests that this RMSD maximum is caused by the analyses failing to accurately capture the capping inversion strength, as also seen in Coniglio et al. (2013). Another local RMSD maximum of ~1.75 K is seen at 500 hPa in association with a local minimum in MB of ~ -1 K, part of a mid-level cold bias that is present across all regions. Inspection of individual observed upsondes often reveals the presence of weak to moderate stable layers at the top of the elevated mixed layer (as in the CSU and TAMU soundings in Fig. 1.2). These features are not captured by the analyses, which tend to have smooth vertical temperature profiles, contributing to the mid-level cold bias. The largest RMSD, MES, and MB is in upper-levels near the tropopause. Temperatures near the tropopause have large spatial variations, as seen in Fig. 1.2 where upsondes were released within 150 km of each other. Significant horizontal gradients in tropopause temperature lead to larger RMSDs and MBs as well as large MES due to ensemble variability.

For inflow soundings, observations reveal a small warm bias of approximately 1 K from the surface up to 600 hPa that slowly transitions to a negative bias by 500 hPa (Fig. 3.3c,d). In contrast, outflow analyses have a large warm MB of slightly less than 2 K in low-levels (near 850 hPa; Fig. 3.3e,f), corresponding to a very large RMSD of approximately 4 K at the same pressure level. This warm bias is unique to outflow regions since it does not appear in non-outflow regions. The pronounced warm bias and RMSD maximum in these low-levels is due to the analysis cold pools being warmer than observed, as also suggested by Engerer et al. (2008). This result also suggests cold pools are too shallow in the ensemble analyses. Some outflow samples are considered anvil as well (Figs. 3.3g,h), where the inclusion of outflow samples is the source of the RMSD maximum near 850 hPa for these two regions. Anvil region MES in upper-levels of the troposphere increases dramatically, signifying large temperature ensemble variations within thunderstorm anvils.

Relative humidity RMSDs for all upsondes increase with height, beginning near 6 % at 925 hPa and increasing to approximately 18 % between 850 and 700 hPa (Fig. 3.4a). MB magnitudes are less than 10 % below 500 hPa, suggesting low-level relative humidity analyses are reasonable (Fig. 3.4b). RMSD and MB continue to increase into the mid-levels (~ 400 hPa) reaching ~25% and ~13 %, respectively, and the values of RMSD tend to remain fairly constant until the tropopause. Inspection of a number of upsonde humidity profiles suggests that the larger RMSDs and MBs in mid- to upper-levels likely are due in part to either the presence or absence of observed moist layers combined with smooth ensemble analyses and large MES. As Fig. 1.2 suggests, moist layers have well-defined tops where relative humidity decreases rapidly with height. Therefore, small vertical displacement errors in the locations of the moist layers produce large RMSDs. The upsondes also have a known issue measuring humidity when RH is < 20 %, a common occurrence in upper-levels of the troposphere (Sapucci et al. 2005) that contributes to the large positive MB and large RMSD values above 400 hPa. Large RMSD and, by comparison, small MB below 700 hPa, result from a large variance in analysis errors among samples. This result is evidenced by MES between 850 and 700 hPa, where the MES magnitude approaches 80 %.

The RMSDs of zonal and meridional winds for all upsondes reveal relatively small analysis errors in low-levels (Figs. 3.5a,3.6a). The zonal wind RMSD is less than 5 m s^{-1} below 450 hPa but slowly and steadily increases until 225 hPa. The zonal mean MB (Fig. 3.5b) oscillates around 0 m s^{-1} in the low- to mid-levels and is strictly positive above ~325 hPa. Meridional winds also have RMSDs less than 5 m s^{-1} above 925 hPa and below 500 hPa. Both the zonal and meridional winds have a local RMSD maximum in the upper-levels of the troposphere near 200 hPa, with the zonal wind having a small positive MB and the meridional wind having a larger negative MB. This finding is associated with large MES within thunderstorm anvils for both zonal and meridional winds (Figs. 3.5g, 3.6g). An encouraging result arises from the inflow region zonal wind below 500 hPa, where MB oscillates between -2 and 2 m s^{-1} throughout that vertical depth (Fig. 3.5d). However, the inflow region meridional wind has negative MBs for the entire depth with magnitudes reaching ~ 3 m s^{-1} and RMSDs at or above 5 m s^{-1} (Fig. 3.6c,d). The northerly bias indicates an under prediction of inflow wind speeds into the convective region given the strong southerly component associated with storm inflow in the supercell cases of 30 and 31 May. Non-inflow region results show smaller meridional wind RMSDs in low- to mid-levels than found in the inflow region by comparison.

Wind speed for all upsondes is negatively biased in the analyses from the surface to 400 hPa (Fig. 3.7b). A negative wind speed maximum in MB occurs at 200 hPa. This maximum is collocated with a negative meridional wind MB at 200 hPa (Fig.

3.6b), which produces the negative wind speed bias along with some directional error. A comparison of wind components in the 150-100 hPa layer shows the zonal wind to be slightly overestimated while the meridional wind MB is near 0. The inflow region low-level wind speeds are under predicted much more so than low-level non-inflow region wind speeds (Fig. 3.7d). Outflow wind speed MB is similar to non-outflow MB (Fig. 3.7f). The large MES is once again present within upper-levels of anvil regions (Fig. 3.7g).

Another environmental parameter conducive for convection includes vertical wind shear. The RMSDs of Sfc-700 hPa and Sfc-500 hPa wind shear are 5.9 m s^{-1} and 4.5 m s^{-1}, respectively (Table 3.1). Magnitudes of MB for both layers are quite small (-0.8 m s^{-1} and -0.3 m s^{-1}, respectively). The large RMSD and small MB imply a large variance among samples. Model analyses reveal steep shear gradients near convection (not shown), which would induce large variances when spatial errors are present. Of all near-storm environment regions, inflow regions have the largest RMSDs for both Sfc-700 hPa and Sfc-500 hPa wind shear. All other regions are very comparable to the overall values previously mentioned. The MBs of all regions except inflow are comparable as well. Inflow Sfc-700 hPa MB is notably larger in magnitude (negative value) since the meridional winds analyses have a notable northerly bias.

Region	Sfc-700 hPa count	Sfc-700 hPa RMSD	Sfc-700 hPa MB	Sfc-500 hPa count	Sfc-500 hPa RMSD	Sfc-500 MB
All	80	5.9	-0.8	70	4.5	-0.3
Inflow	17	7.2	-4.2	11	6.8	-1.3
Non-inflow	63	5.2	-0.2	59	4.3	-0.4
Outflow	15	5.0	-0.3	14	4.1	-0.4
Non-outflow	65	6.1	-1.1	56	5.1	-0.3
Anvil	57	6.0	-0.4	47	5.2	0.1
Non-anvil	23	5.7	-2.0	23	4.4	-1.1

Table 3.1. Sfc-700 hPa and Sfc-500 hPa wind shear RMSD and MB for all upsondes and each individual near-storm environment region. All RMSDs and MBs are in m s^{-1}. The number of shear observations within each region is listed last.

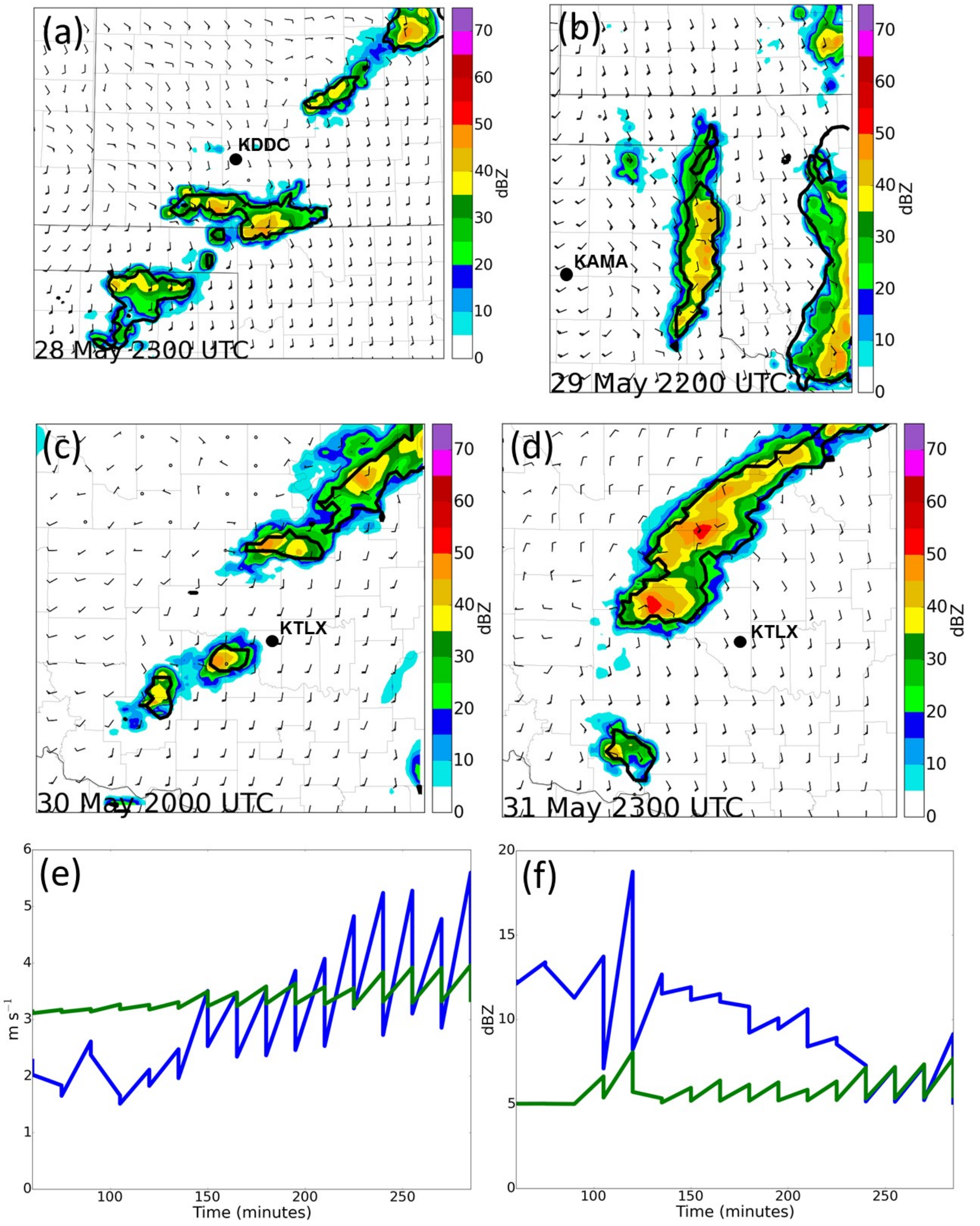

Figure 3.1. Examples of low-level ensemble mean analysis reflectivity and surface winds in knots (barbs) with observed 20 dBZ reflectivity outlined with solid black line, at 0.5^{o} tilt by the designated radar, (a) 2300 UTC 28 May (KDDC), (b) 2200 UTC 29 May (KAMA), (c) 2000 UTC 20 May (KTLX), (d) 2300 UTC 31 May (KTLX). Example radial velocity (e) and reflectivity (f) sawtooth diagrams show ensemble mean prior and posterior RMSE (blue) and ensemble total spread (green) from 28 May with time (minutes) after storm-scale assimilation begins.

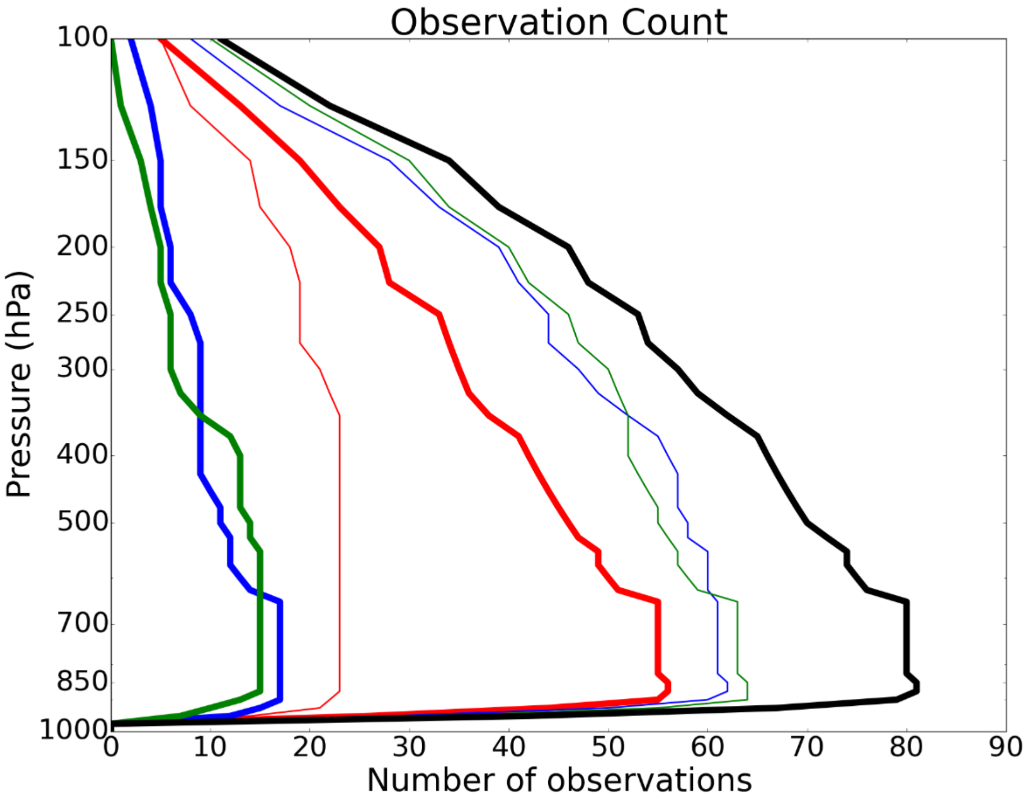

Figure 3.2. Number of MPEX upsonde samples with height 28-31 May. All (black), inflow (thick blue), non-inflow (thin blue), outflow (thick green), non-outflow (thin green), anvil (thick red), and non-anvil (thin red).

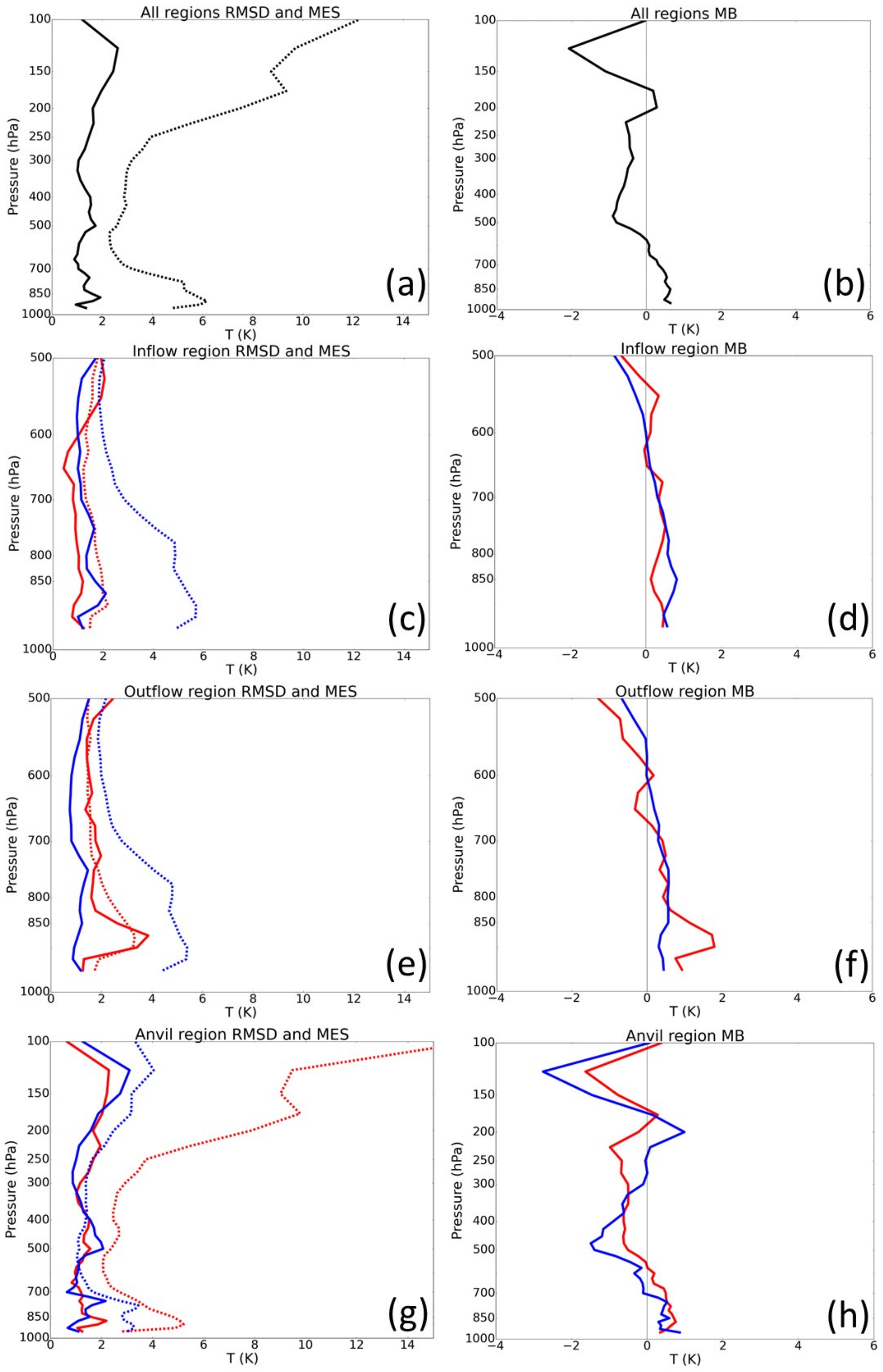

Figure 3.3. Vertical profiles of temperature (T) root mean square difference (RMSD, solid), mean ensemble spread (MES, dashed), and mean bias (MB, solid). All upsonde RMSD and MES, 1000-100 hPa (a), all upsonde MB, 1000-100 hPa (b), inflow (red) and non-inflow (blue) RMSD and MES, 1000-500 hPa (c), inflow (red) and non-inflow (blue) MB, 1000-500 hPa (d), outflow (red) and non-outflow (blue) RMSD and MES, 1000-500 hPa (e), outflow (red) and non-outflow (blue) MB, 1000-500 hPa (f), anvil (red) and non-anvil (blue) RMSD and MES, 1000-100 hPa (g), anvil (red) and non-anvil (blue) MB, 1000-100 hPa (h).

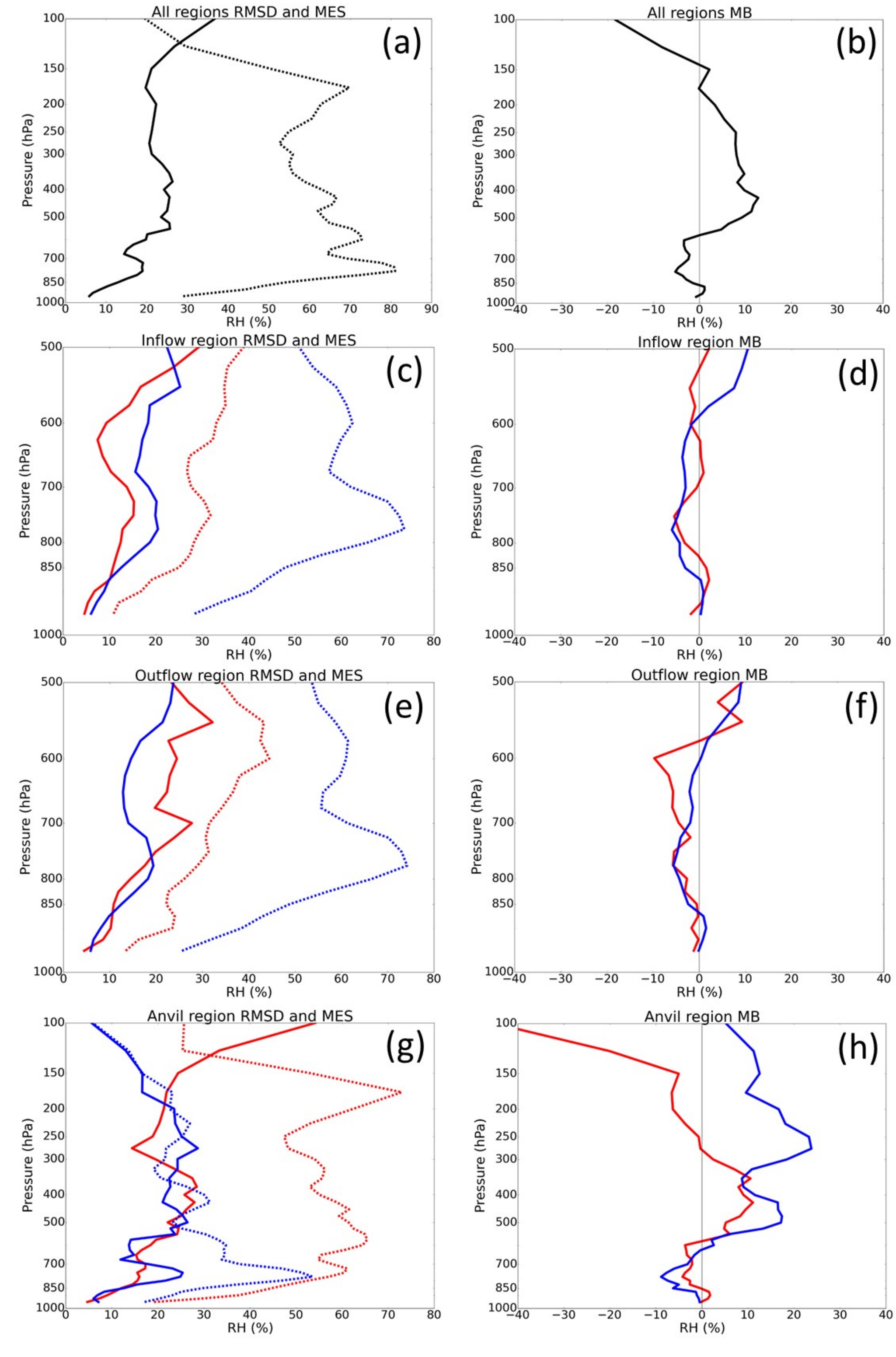

Figure 3.4. As in Fig. 3.3, but for relative humidity (RH).

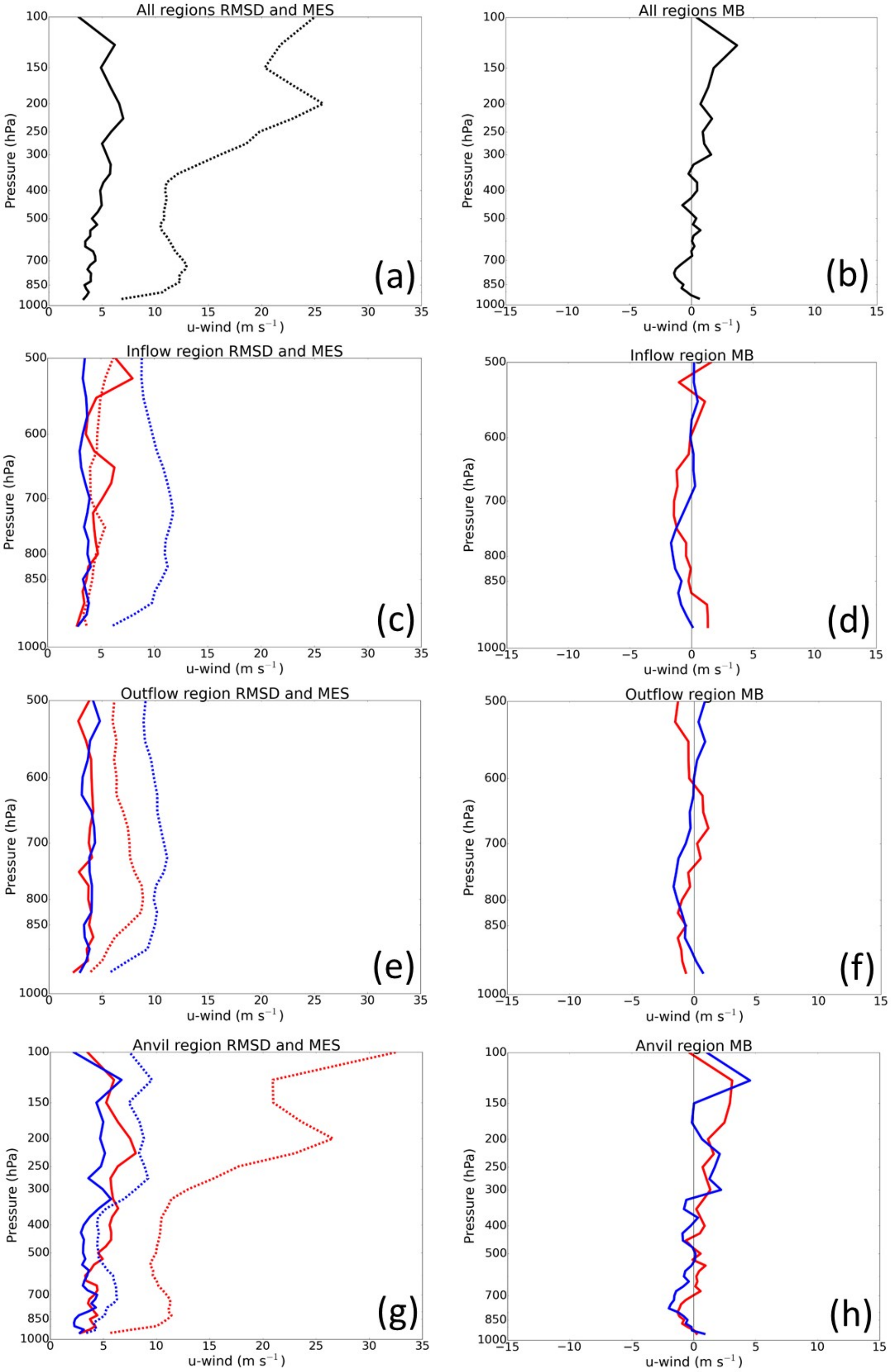

Figure 3.5. As in Fig. 3.3, but for zonal winds (u-wind).

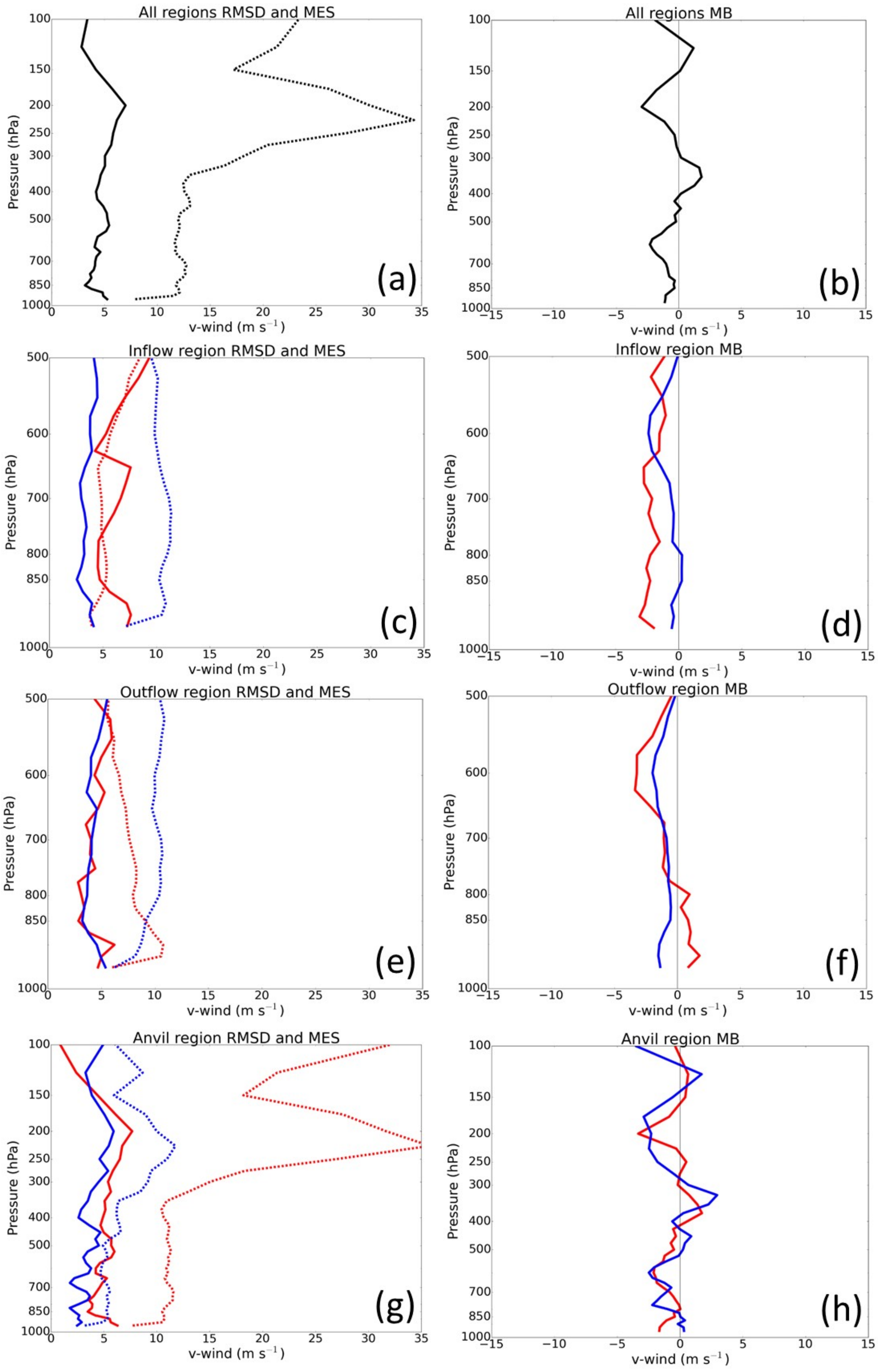

Figure 3.6. As in Fig. 3.3, but for meridional winds (v-wind).

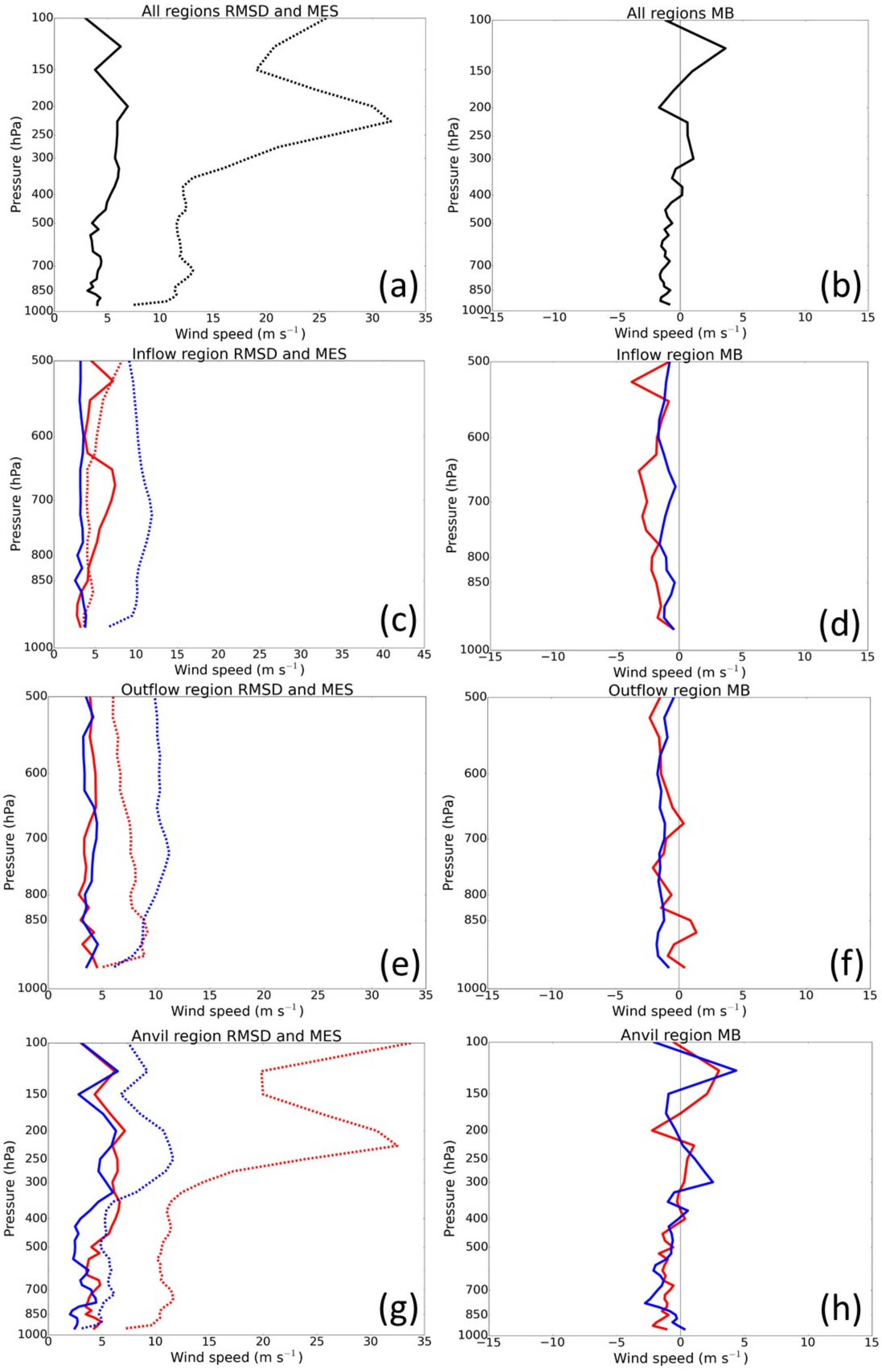

Figure 3.7. As in Fig. 3.3, but for wind speed.

3.2 Bias distributions

Histograms are used to show the distribution of biases for different state fields. At pressure levels where there are large magnitudes of RMSD and/or MB, these distributions may shed light on bias characteristics. Biases of each ensemble member for each sample are calculated for selected variables at specified pressure levels. The resulting bias distribution for 875 hPa temperature is Gaussian-like with a maximum on the positive side of zero and more bias samples > 4 K than < -4 K (Fig. 3.8a).

Another Gaussian distribution is suggested in the relative humidity errors at 750 hPa (Fig. 3.8b). However, the peak of the distribution is near + 5 %. As the magnitude of the MB increases, there are generally more negative samples than their positive counterparts. The 225 hPa zonal wind field reveals a bimodal distribution where one peak is near zero and a second peak is between 5 and 10 m s^{-1} (Fig. 3.8c). It should be noted that there are many samples of extremely large bias magnitude (> 15 m s^{-1}), indicating large differences with some ensemble members. A histogram of 200 hPa meridional wind bias also has a bimodal distribution (Fig. 3.8d). However, the two maximums are near zero and between -5 and -10 m s^{-1}.

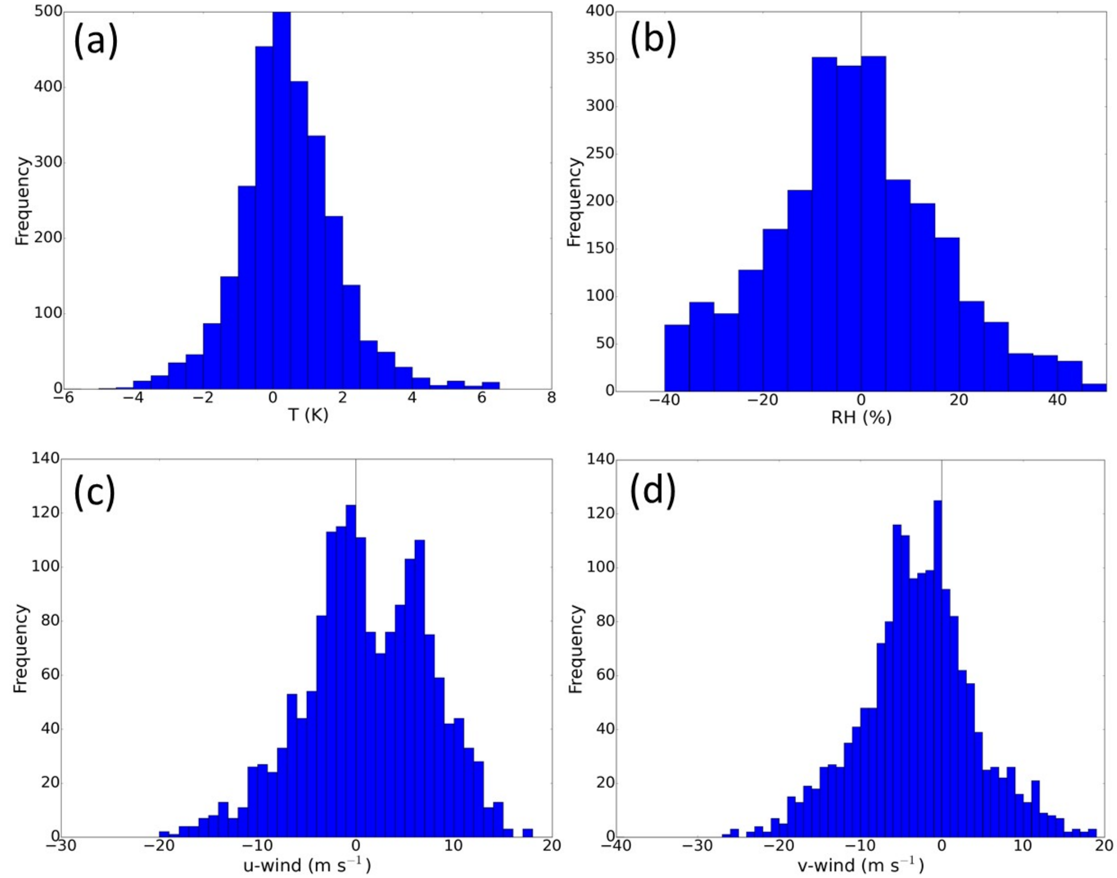

Figure 3.8. Individual ensemble member bias histograms where frequency is number of ensemble member biases over all 81 samples (2,916 total) for (a) 875 hPa temperature with 0.5 K bins, (b) 750 hPa relative humidity, 5% bins, (c) 225 hPa u-wind, 1 m s^{-1} bins, and (d) 200 hPa v-wind, 1 m s^{-1} bins.

3.3 Physics dependent errors

Fig. 3.9 depicts differences in MB and RMSD among ensemble members that differ in their physics as described in Table 1. The nested domain physics has variations in PBL scheme (3) and short-wave/long-wave radiation scheme combinations (2; see Table 2.1). Temperature biases below approximately 600 hPa are largely dependent on PBL scheme (Fig. 3.9a,b). The YSU PBL scheme results in larger warm biases below 850 hPa and smaller warm biases between 850 and 600 hPa compared to the other schemes. When combined with results with relative humidity (Fig. 3.9c,d), where the YSU scheme has a dry bias below 850 hPa and a moist bias above 850 hPa, the data suggest that YSU produces boundary layers that are too deep. Dry biases above 850 hPa for MYJ and MYNN PBL schemes suggest boundary layers that are too shallow (Hong et al. 2006; Coniglio et al. 2013). The MYJ PBL scheme has the smallest bias in temperature and relative humidity below 850 hPa. Members utilizing the Dudhia-RRTM radiation scheme combination also have a slight warm bias compared to its RRTMG scheme counterpart below 850 hPa. However, the Dudhia-RRTM combination is slightly cooler than RRTMG between 850 and 600 hPa. No significant differences in temperature are seen between radiation physics options above 600 hPa.

The effects of PBL schemes (mainly YSU) extend further into the mid-troposphere in all fields except temperature. MYJ has the driest bias between 800 hPa and ~ 550 hPa. Radiation schemes do not have as great of an effect on relative humidity bias. The Dudhia-RRTM combination has a slight dry bias over RRTMG below 850 hPa. Horizontal wind fields are negligibly affected by physics schemes (Figs. 3.9e,f,g,h). However, MYJ PBL scheme seems to have a more negative bias over

YSU and MYNN in mid- to upper-levels within the zonal wind field while causing a more positive bias within the meridional wind field.

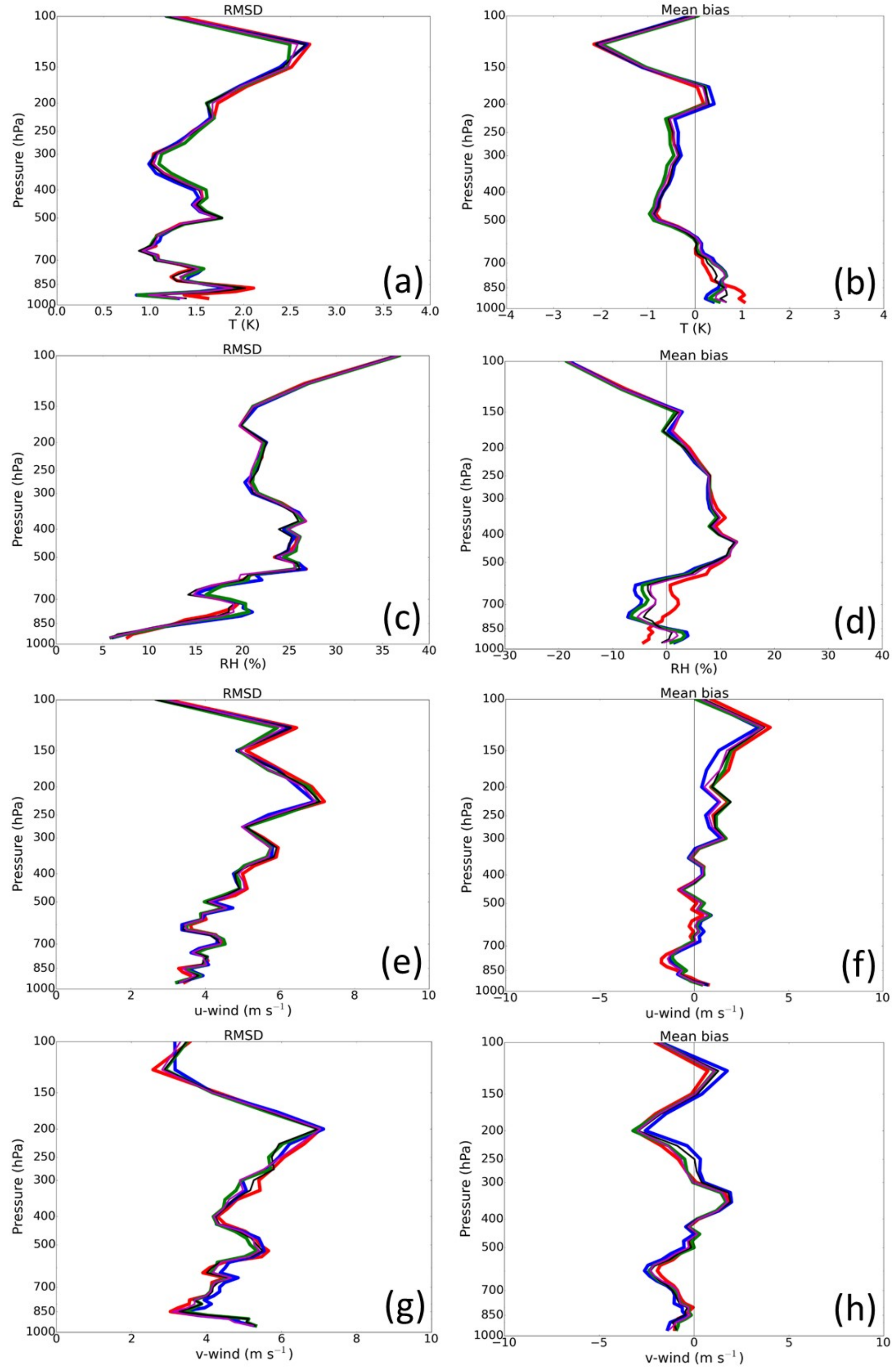

Figure 3.9. RMSD and MB for mean of members with specific physics schemes (YSU PBL – red, MYJ PBL – blue, MYNN PBL – green, Dudhia-RRTM combination – black, RRTMG combination – magenta). Profiles are for temperature RMSD (a), temperature MB (b), relative humidity RMSD (c), relative humidity MB (d), u-wind RMSD (e), u-wind MB (f), v-wind RMSD (g), and v-wind MB (h).

3.4. Near-storm environment forecast errors

Ensemble forecasts are initialized 60 minutes prior to each upsonde launch time. The 60 minute forecasts, valid at the upsonde launch times, are verified using the same methods as the analysis verification (section 3.1). RMSD, MES, and MB are calculated for forecasted near-storm temperature in various near-storm environment regions (Fig. 3.10). Errors only increase slightly for all regions from those of the ensemble analyses. For all regions, the forecasts are warm biased below ~600 hPa (Fig. 3.10b). In the mid-levels, the forecasts are cold biased. The forecasts have a slight warm bias near 200 hPa. Inflow regions' MB is near zero at 850 hPa while non-inflow regions have a warm biases near 1 K (Fig. 3.10d). The warm bias within outflow regions is the most notable feature. For 60 minute forecasts, the RMSD of outflow temperature (Fig. 3.10e) shows large errors just at and below 850 hPa that extend to > 4 K. The outflow MB is very similar to analysis MB where the value is approximately 2 K below 850 hPa. The MES of anvil region temperature is large within the upper troposphere compared to non-anvil regions (Fig. 3.10g). MES is ~10 K at 200 hPa in anvil regions versus ~3 K for non-anvil regions. This is due to steep horizontal gradients temperature in the upper troposphere of anvil regions.

Relative humidity forecast errors are similar to analysis errors as well (Fig. 3.11). RMSD increases around 500 hPa to nearly 25% (Fig. 3.11a). For all regions, the forecasts are predominantly too dry in low- to mid-levels (Fig. 3.11b). The maximum magnitude of this bias is slightly less than 10% between 850 and 700 hPa. This is consistent for inflow, outflow, and anvil regions (Fig. 3.11d,f,h). Within anvil regions, there is substantial MES throughout the troposphere (Fig. 3.11g). This is due to the close proximity to convection where steep gradients in moisture can cause large differences between ensemble members. These gradients are smaller in non-anvil regions, which are mostly pre-convective and far-field soundings (not shown).

Zonal winds errors do not rapidly increase during a 60 minute forecast (Fig. 3.12). The maximum RMSD (~ 5 m s^{-1}) within the column is near 200 hPa (Fig. 3.12a). This is associated with a large MES (> 30 m s^{-1}) at the same level. Within low-levels, the MB reveals a slight westerly bias below 850 hPa but an easterly bias between 850 and 750 hPa (Fig. 3.12b). The westerly bias below 850 hPa and easterly bias from 850 – 700 hPa can be attributed to inflow regions (Fig. 3.12d). The large RMSD and MES near 200 hPa is confined to anvil regions just as in the analyses (Fig. 3.12g).

Meridional winds see larger error growth during a forecast (Fig. 3.13). RMSD oscillates around 5 m s^{-1} between the surface and 500 hPa (Fig. 3.13a). A negative MB exists in the low-levels similar to the analyses (Fig. 3.13b). A large increase in inflow MB (northerly) is seen between these forecasts and analyses (Fig. 3.13d). In the forecasts, the MB has nearly tripled to ~5-6 m s^{-1} compared to the analyses. This result is consistent from the surface to 500 hPa. Within outflow regions, the low-levels have southerly biases (Fig. 3.13f). In the upper-levels, anvil regions have a maximum in RMSD near 200 hPa (Fig. 3.13g), due to the large MES at the same level, where slight differences in storm locations result in large MES.

Wind speed errors are strongly affected by meridional wind errors, especially within inflow regions (Fig. 3.14). Inflow region wind speed MB also triples when compared to analysis MB (Fig. 3.14c). The difference between outflow and non-outflow wind speed MB is larger in comparison to analyses (Fig. 3.14f). Outflow wind speed

MB is positive while non-outflow MB is negative (primarily due to the inclusion of inflow upsondes). Anvil region RMSD and MES is affected by the large errors in both zonal and meridional winds in the upper troposphere (Fig. 3.14g).

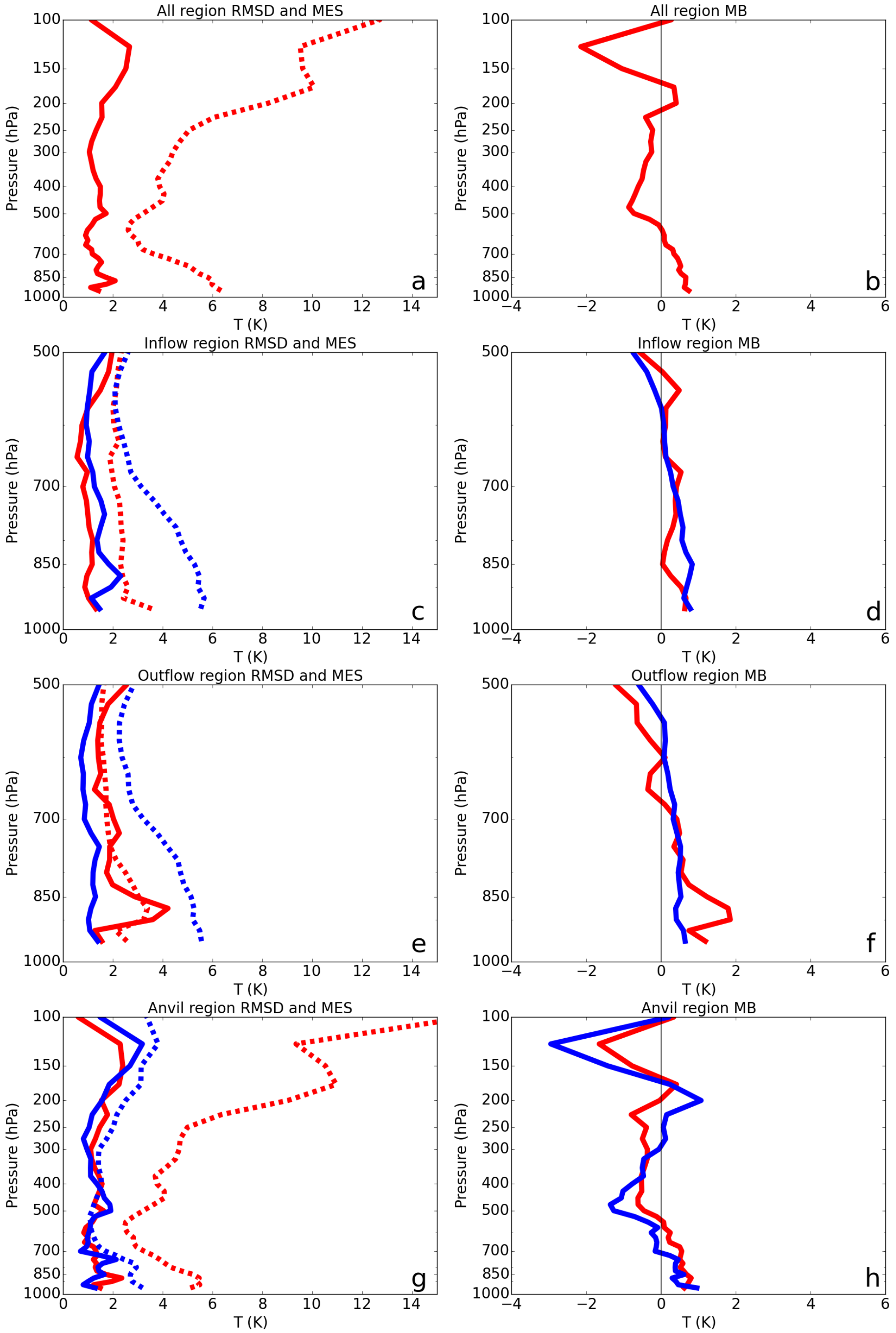

Fig. 3.10. Vertical profiles of one-hour forecast temperature (T) root mean square difference (RMSD, solid), mean ensemble spread (MES, dashed), and mean bias (MB, solid). All upsonde RMSD and MES, 1000-100 hPa (a), all upsonde MB, 1000-100 hPa (b), inflow (red) and non-inflow (blue) RMSD and MES, 1000-500 hPa (c), inflow (red) and non-inflow (blue) MB, 1000-500 hPa (d), outflow (red) and non-outflow (blue) RMSD and MES, 1000-500 hPa (e), outflow (red) and non-outflow (blue) MB, 1000-500 hPa (f), anvil (red) and non-anvil (blue) RMSD and MES, 1000-100 hPa (g), anvil (red) and non-anvil (blue) MB, 1000-100 hPa (h).

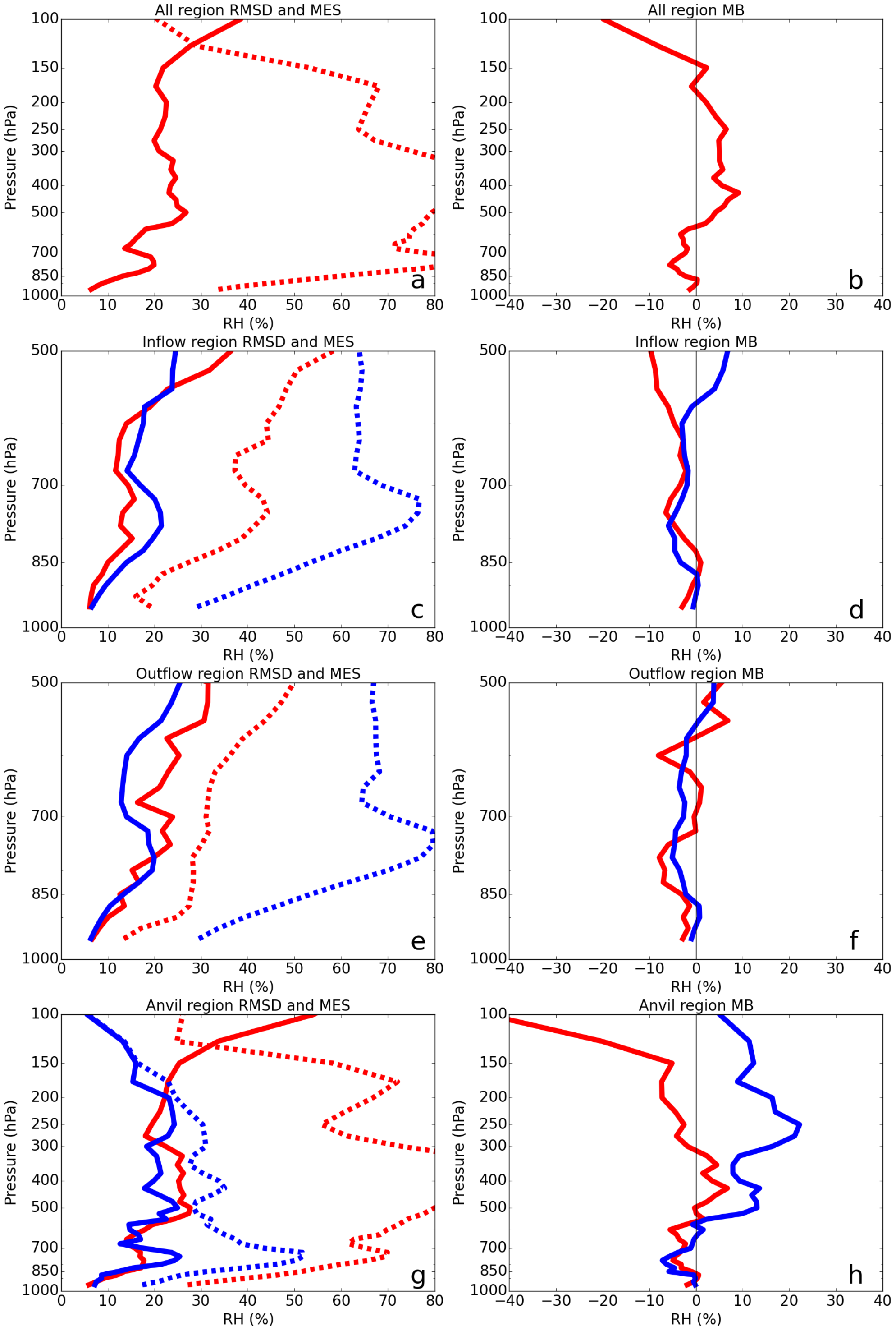

Fig. 3.11. As in Fig. 3.10, but for relative humidity (RH).

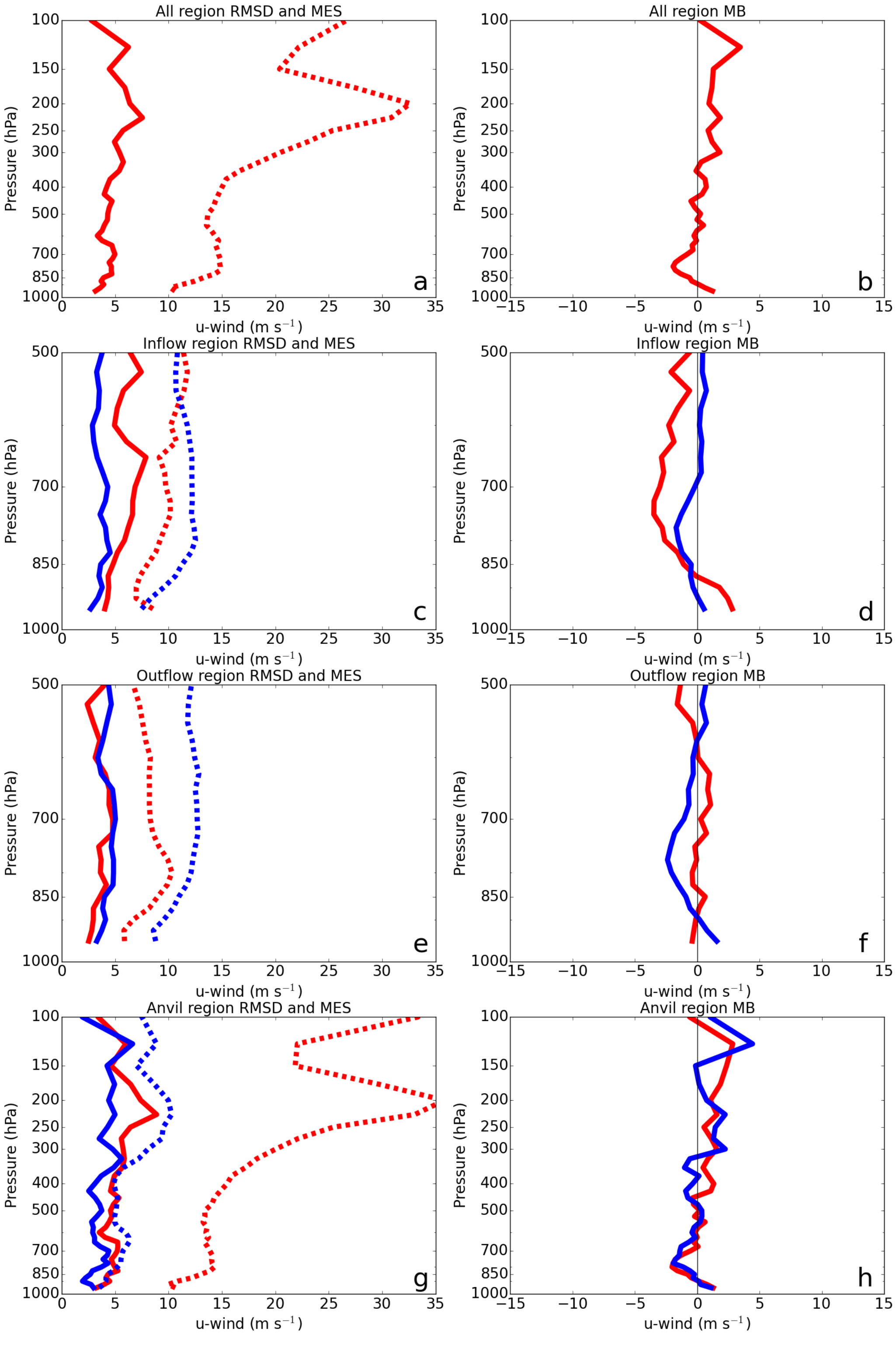

Fig. 3.12. As in Fig. 3.10, but for zonal winds (u-wind).

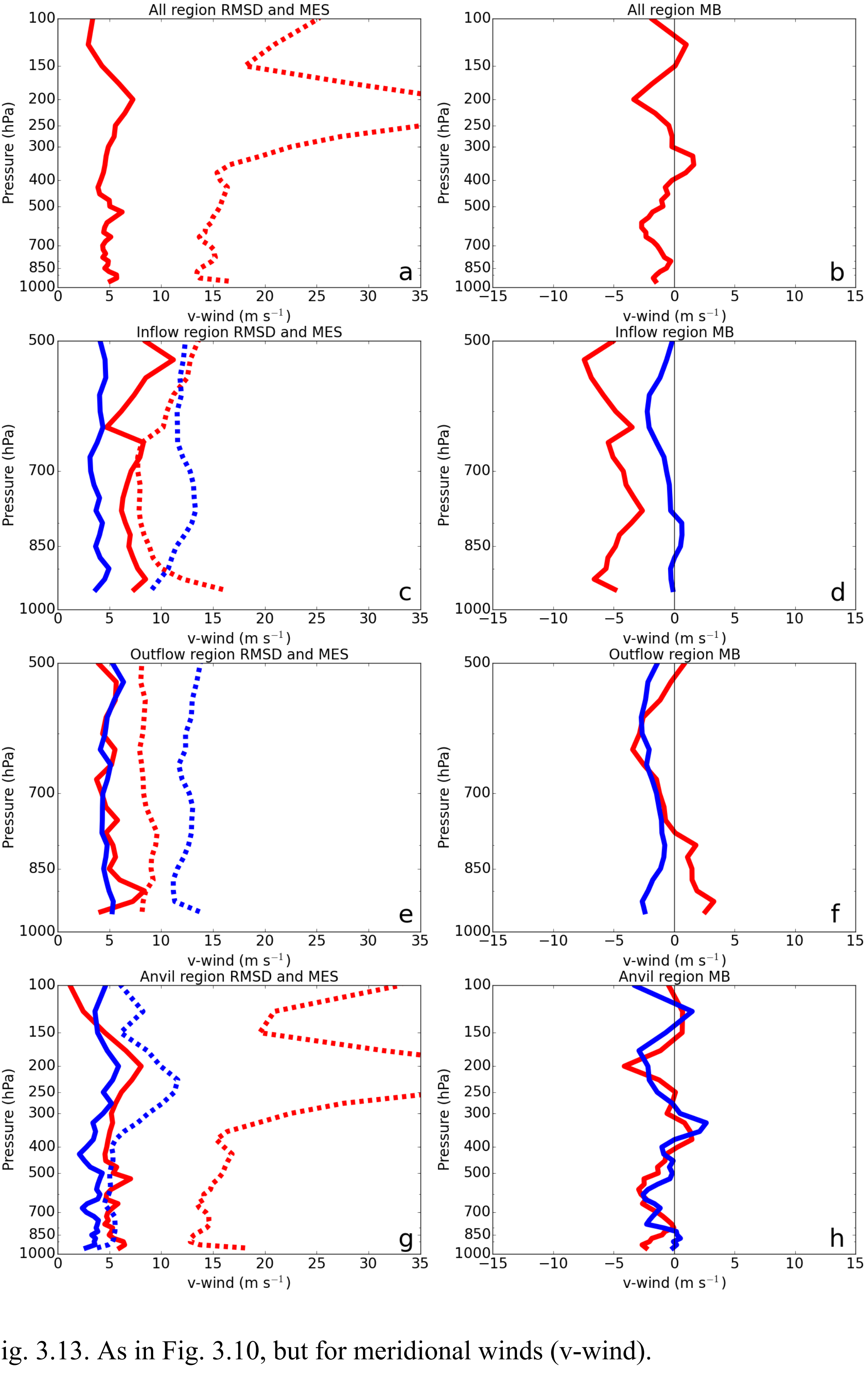

Fig. 3.13. As in Fig. 3.10, but for meridional winds (v-wind).

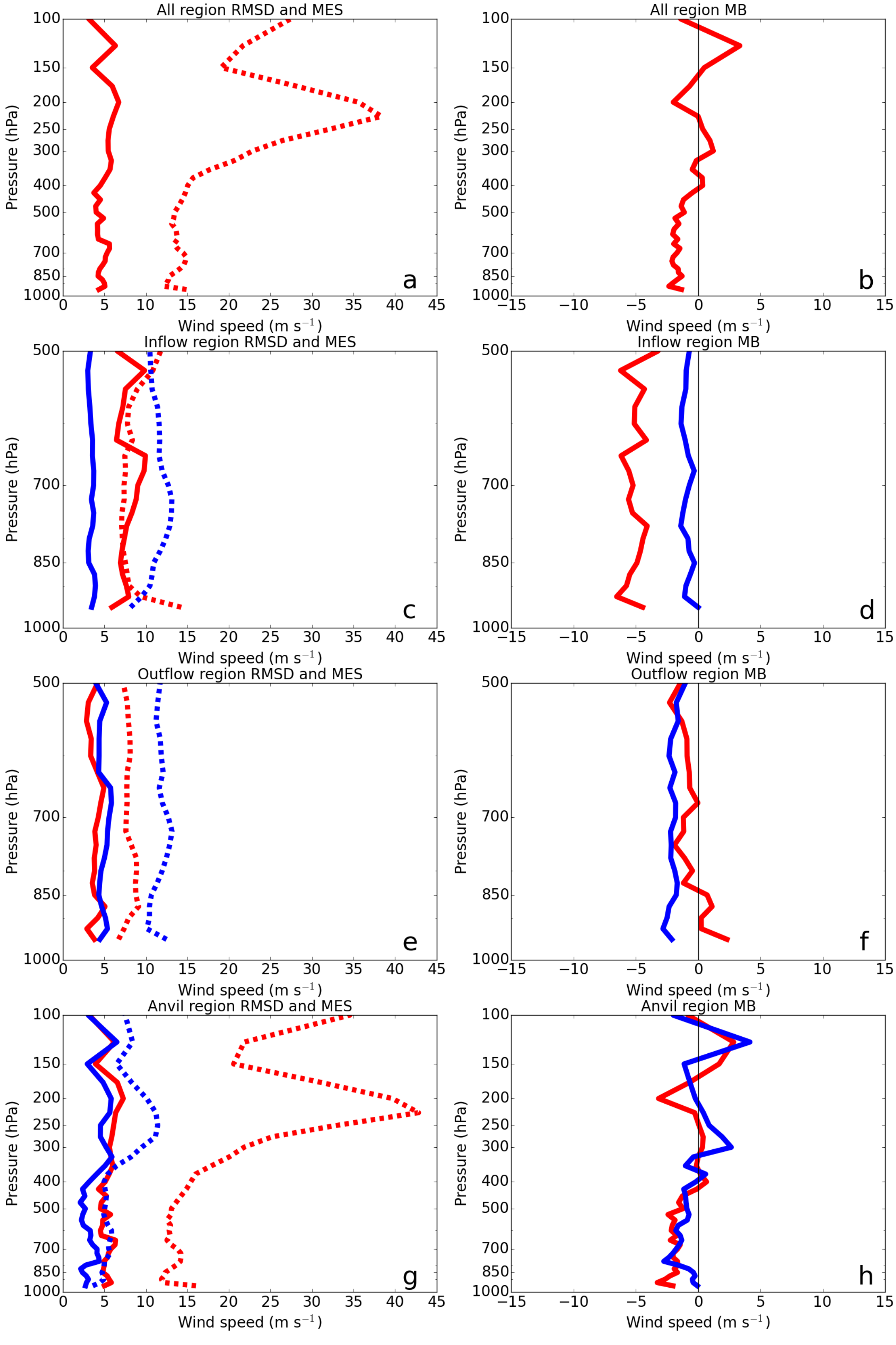

Fig. 3.14. As in Fig. 3.10, but for wind speed

3.5. Discussion and conclusions

Over this four-day period, a total of 81 upsondes were released nearby deep convection in a variety of storm-relative locations. The decreasing sample size with height obviously weakens the conclusions made within the upper troposphere, especially in near-storm environment regions with small sample sizes. Nonetheless, the special MPEX observations revealed that WRF-ARW ensemble mean analyses at CAM grid spacing agree reasonably well with the observed convective near-storm environments over this four-day sequence, with some notable exceptions.

1) A large variance in analysis temperature bias is implied by a maximum of RMSD in temperature just below 850 hPa. This is likely in part a result of model analyses improper handling of capping inversions at the top of the PBL (not shown), which were present in many sounding datasets. The choice of PBL schemes is found to greatly impact the low-level temperature analyses. This has previously been presented by Coniglio et al. (2013) where model temperatures in pre-convective environments are highly dependent on PBL scheme.
2) The outflow region upsondes reveal a large warm bias in the analyses near 850 hPa. Further inspection of individual soundings show that the ensemble analyses have warmer temperatures than observed, a result consistent with the conclusions of Engerer et al. (2008). Since cold pools are important to the evolution of deep convection (Rotunno et al. 1988; Weisman and Rotunno 2004), this result deserves further attention as it could impact forecast accuracy.

3) The negative temperature MB in upper-levels is a result of horizontal temperature gradients near the tropopause not being accurately captured by the analyses. Errors in horizontal temperature gradient placements cause RMSD and MB magnitudes to increase. Overall, near-storm temperatures are well depicted in the ensemble analyses considering the lack of conventional mesoscale temperature profile observations.

4) Relative humidity MB is consistently between +/- 10 % below 500 hPa in all regions nearby deep convection. However, relative humidity RMSD increases with height and is above 20% by 500 hPa. The mid-level relative humidity errors appear to be due to smooth ensemble analyses and errors in dry and moist layer vertical positions. A propagation of error analysis created by the partial derivatives of a function can reveal the impacts of variable errors on the function (Ku 1966). The inflow moisture error at 850 hPa (mixing ratio bias of ~ $+7.2 \times 10^{-4}$ kg kg^{-1}) combined with error in 850 hPa temperature leads to an 850 hPa equivalent potential temperature (θ_e) bias of ~ +2 K, where ~ 1.9 K of the bias is due to moisture error alone. The model has more latent heating due to this error, which increases updraft speeds.

5) Inflow meridional wind MB below 700 hPa is near -3 m s^{-1}, indicating that inflow wind speeds are underestimated in the ensemble analyses. A propagation of error calculation (Ku 1966) for Sfc-500 hPa vertical wind shear given an inflow meridional surface wind bias of ~ -4.8 m s^{-1} reveals that this error only contributes to -0.16 m s^{-1} of the inflow shear bias. Thus,

the majority of wind shear error likely originates from mid-level (500 hPa) wind error. This notion deserves further study.

6) Within the upper-troposphere between 300 and 150 hPa, both horizontal wind components have large RMSDs. Upper-level wind MB are present in all near-storm environment regions, but are more pronounced within anvil regions, including within the environments downstream of convection. These results suggest the model struggles to accurately depict convective alterations of the upper-levels where winds have a northwesterly directional bias and speeds are under predicted.

Although analysis errors are large in some regions surrounding the observed areas of deep convection, the analyses created by radar and conventional data assimilation of convective near-storm environments agree reasonably well with the upsonde observations, suggesting that model analyses are a trustworthy source for insight into how deep convection alters the nearby environment. Convective-scale model analyses are therefore a suitable tool to assess the mesoscale feedbacks due to convective storms which could affect further convection evolution. However, even more extensive near-storm observations are required to truly evaluate the impact of convection on its surrounding environment, particularly within inflow and outflow regions. Other simulations with varying microphysics schemes would evaluate cold pool strength and depth sensitivity.

Overall, one-hour forecast errors are similar to analysis errors for most variables. This includes the under-prediction of low-level inflow wind speed and cold pool depth. The cold pool depth forecast error is similar in magnitude to the analysis errors, however, the inflow wind speed bias nearly triples from analyses to forecasts. This under-prediction results in weakening storms, as the updrafts will struggle to be maintained, thus hindering the predictability of an individual convective storm.

Chapter 4: Environmental modifications by convection

Using the convective perturbation technique described in Chapter 2, several environmental variable changes due to convection are analyzed using ensemble analyses from 29, 30, and 31 May 2013. These include the impacts of deep convection on vertical wind shear, CAPE, low-level temperature, upper-level winds, and upper-level temperature.

4.1 Vertical wind shear and CAPE perturbations

Vertical wind shear within near storm environments changes rapidly in the presence of deep convection. The first example is from the 29 May MCS that occurred over the Texas Panhandle. The ensemble mean analysis 0-6 km vertical wind shear at various times during convection evolution shows a notable maximum in shear within the wake of the MCS, where low-level winds are predominantly easterly in the outflow region (Fig. 4.1). The changes in 0-6 km shear since 2100 UTC clearly illustrate the enhancement of shear within the outflow, where shear increases by nearly 25 m s^{-1} in some locations (Fig. 4.2). Shear changes ahead of the MCS are difficult to interpret given the convective system to the east within Oklahoma that also modifies the wind shear.

Brooks et al. (1994) demonstrate how SRH is modified within the inflow of an idealized supercell simulation out to distances of several tens of km. For the present study, 0-6 km vertical wind shear convective perturbations in supercell inflow regions are analyzed. The ensemble mean analysis 0-6 km shear for both the 30 and 31 May supercells in central Oklahoma (Figs. 4.3,4.4) depicts steep gradients in shear within the vicinity of the convection (denoted by reflectivity contours) particularly in the 31 May case (Fig. 4.4c,d) where shear increases to the south of the supercell. The inflow shear maximums are less pronounced in the 30 May case and appear to not extend very far away from the storm (Fig. 4.3).

The convection perturbation technique is applied to 0-6 km vertical wind shear for the 30 and 31 May simulated supercells. Changes in shear due to convection on 30 May indicates that the shear enhances to the southeast of the target supercell in central Oklahoma by magnitudes less than 10 m s^{-1} (Fig. 4.5). Shear is also enhanced by greater magnitudes (~10-12 m s^{-1}) within the lingering cold pools of storms. The enhancement of inflow shear to the south and southeast of the storm is nearly double these values in the 31 May case (Fig. 4.6), in which the inflow shear increases by 15-20 m s^{-1} over a 90 minute period and extends outward from the storm to near the southern Oklahoma border (Fig. 4.6c).

The values and distribution of CAPE is also altered by convection in all three cases. The most obvious effect is the reduction of CAPE in areas where cold pools form (discussed more fully in the next section). The 29 May case has notable CAPE reduction in the wake of the target MCS (Figs. 4.7 and 4.8), with CAPE decreasing by approximately 2000 J kg^{-1} over 90 minutes within the outflow. There is also a decrease in CAPE ahead of this MCS due to the second to the east in Oklahoma. The cold pool reduced CAPE in the wake of this eastern MCS likely contributes in part to the target line’s demise (not shown).

The supercells of 30 and 31 May also modify the CAPE field surrounding the storms. Ensemble mean analysis CAPE on 30 May have maximum values generally located to the east of the target supercell approaching 2000 J kg^{-1} (Fig. 4.9). The short-term changes in CAPE due to convection show some enhancement to the east of the convection as well as CAPE decreases to the north and west of the target supercell from the wakes of the surface cold pools (Fig. 4.10).

The values of CAPE during the 31 May event were much higher, exceeding 4000 J kg^{-1} in some locations (Fig. 4.11). The maximum corridor of CAPE is located to the east and south of the supercell. This maximum moves to the west over the 90 minute period displayed. The change in CAPE (Fig. 4.12) reveals that the storm is responsible for the enhancement of CAPE to its south with increases over 1000 J kg^{-1}. As expected, CAPE also decreases within the storm as well as to the west due to low-level, cool outflow. This magnitude is similar in size to that seen in Brooks et al. (1994), although the size of the enhanced CAPE region on 31 May is much larger than found in Brooks et al. (1994).

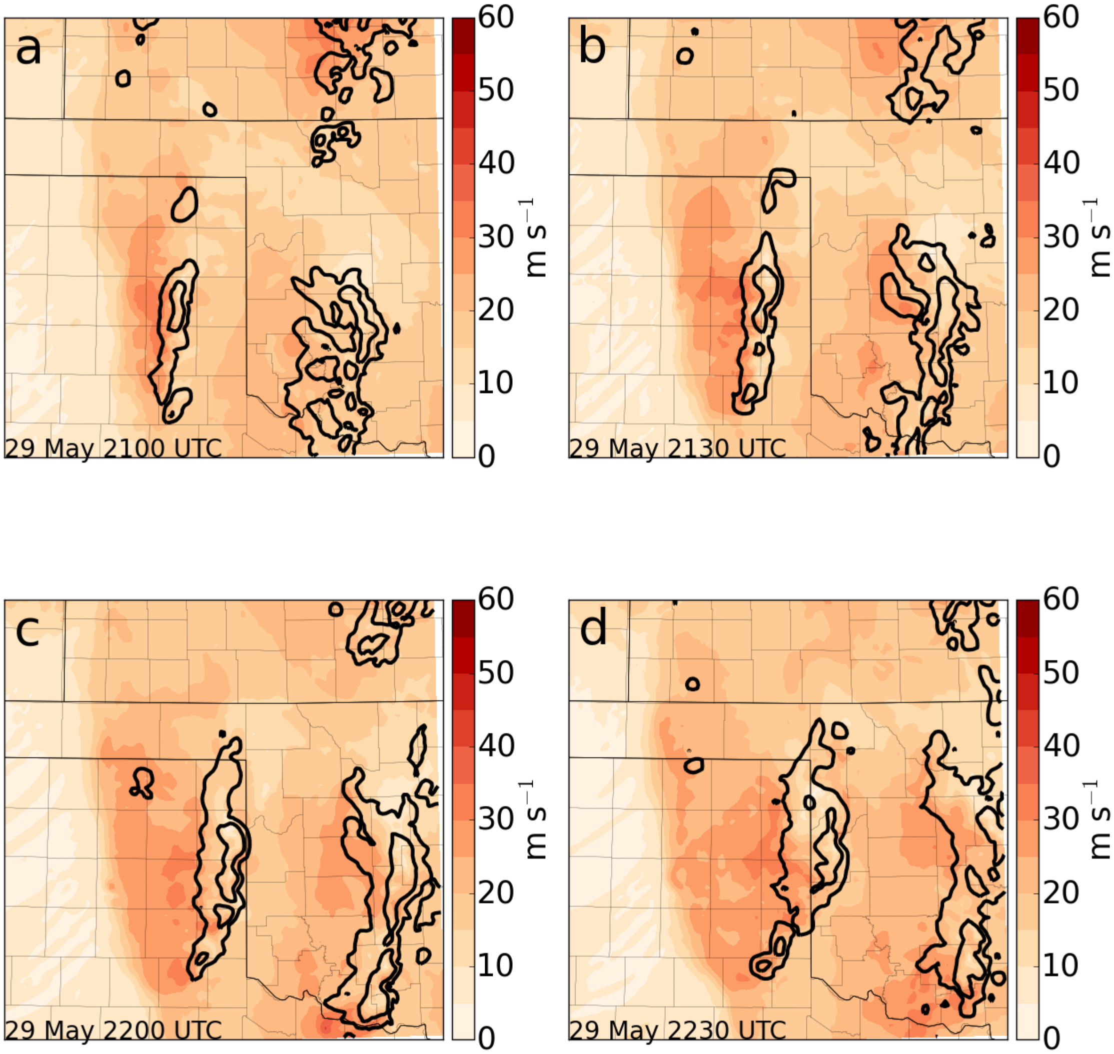

Figure 4.1. Ensemble mean analysis 0-6 km vertical wind shear in m s^{-1} (filled) and low-level reflectivity (black contours) on 29 May 2013 at (a) 2100 UTC (b) 2130 UTC (c) 2200 UTC (d) 2230 UTC

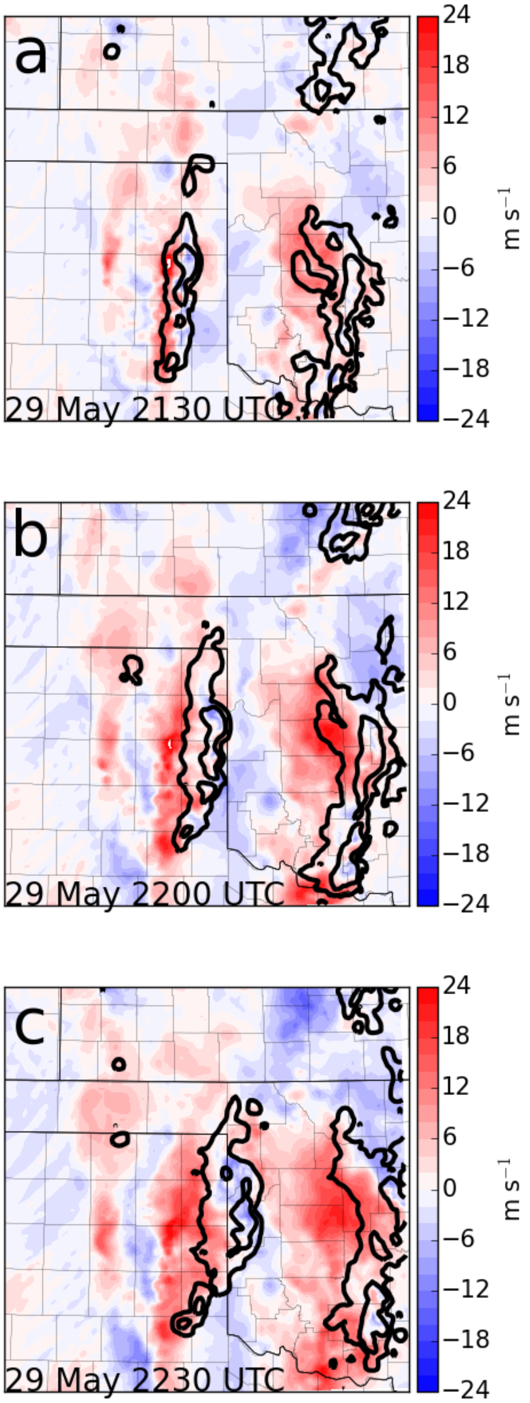

Figure 4.2. 29 May 2013 ensemble mean analysis 0-6 km vertical wind shear difference in m s^{-1} from 2100 UTC due to convection (filled) and low-level reflectivity at (a) 2130 UTC (b) 2200 UTC (c) 2230 UTC.

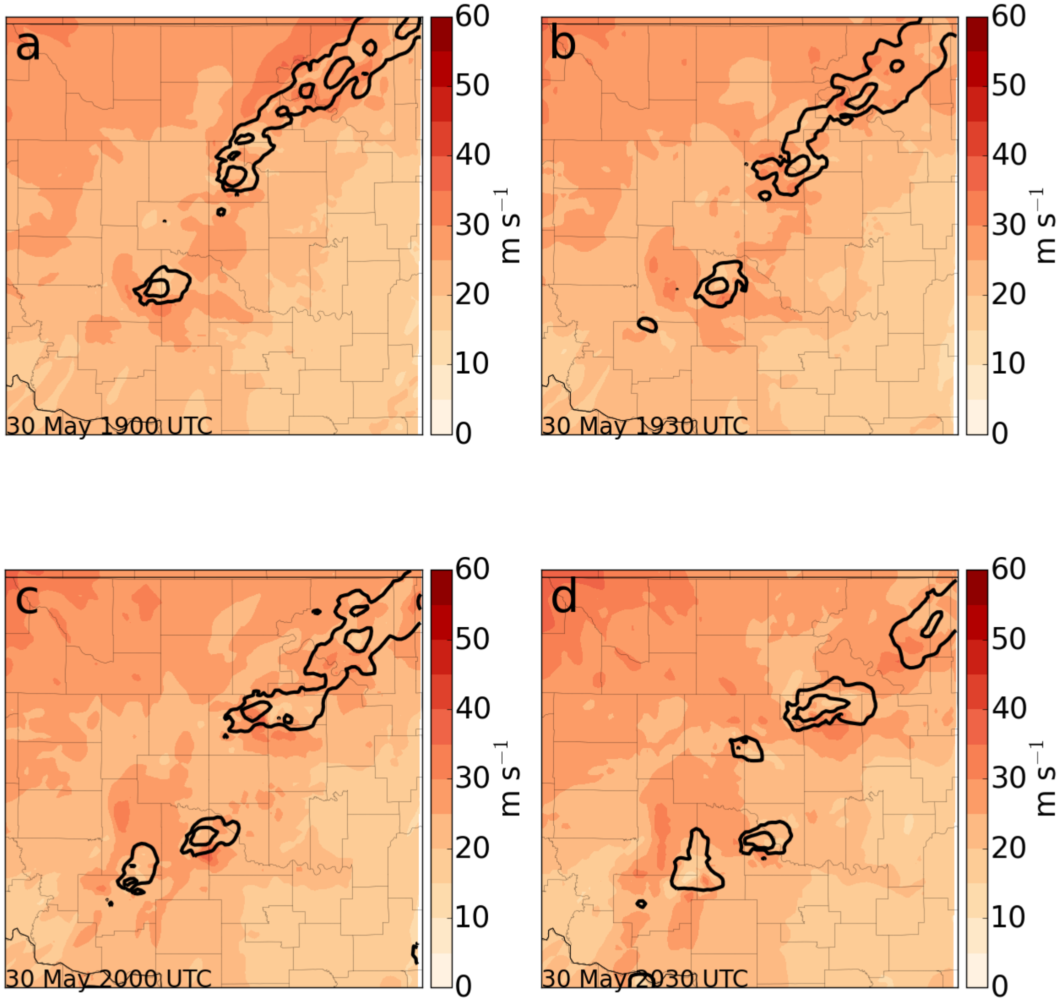

Figure 4.3. Ensemble mean analysis 0-6 km vertical wind shear in m s^{-1} (filled) and low-level reflectivity (black contours) on 30 May 2013 at (a) 1900 UTC (b) 1930 UTC (c) 2000 UTC (d) 2030 UTC.

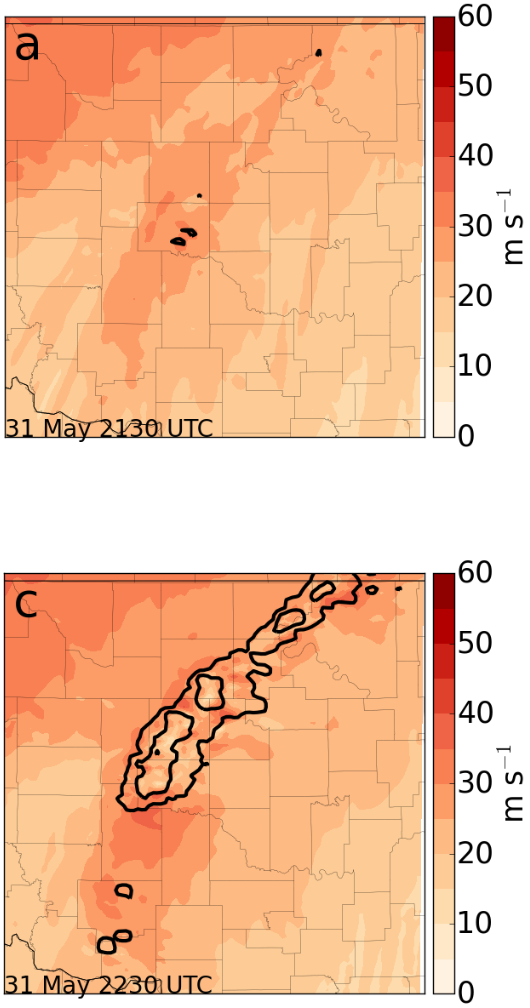

Figure 4.4. Ensemble mean analysis 0-6 km vertical wind shear in m s^{-1} (filled) and low-level reflectivity (black contours) on 31 May 2013 at (a) 2130 UTC (b) 2200 UTC (c) 2230 UTC (d) 2300 UTC.

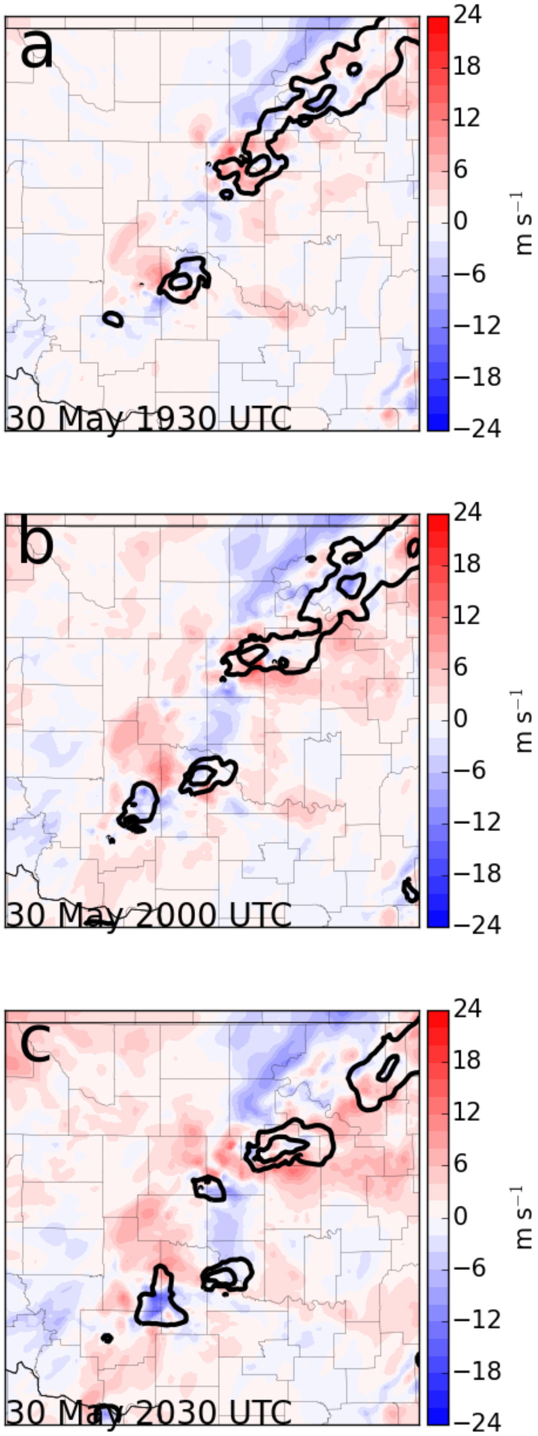

Figure 4.5. 30 May 2013 ensemble mean analysis 0-6 km vertical wind shear difference in m s^{-1} from 1900 UTC due to convection (filled) and low-level reflectivity at (a) 1930 UTC (b) 2000 UTC (c) 2030 UTC.

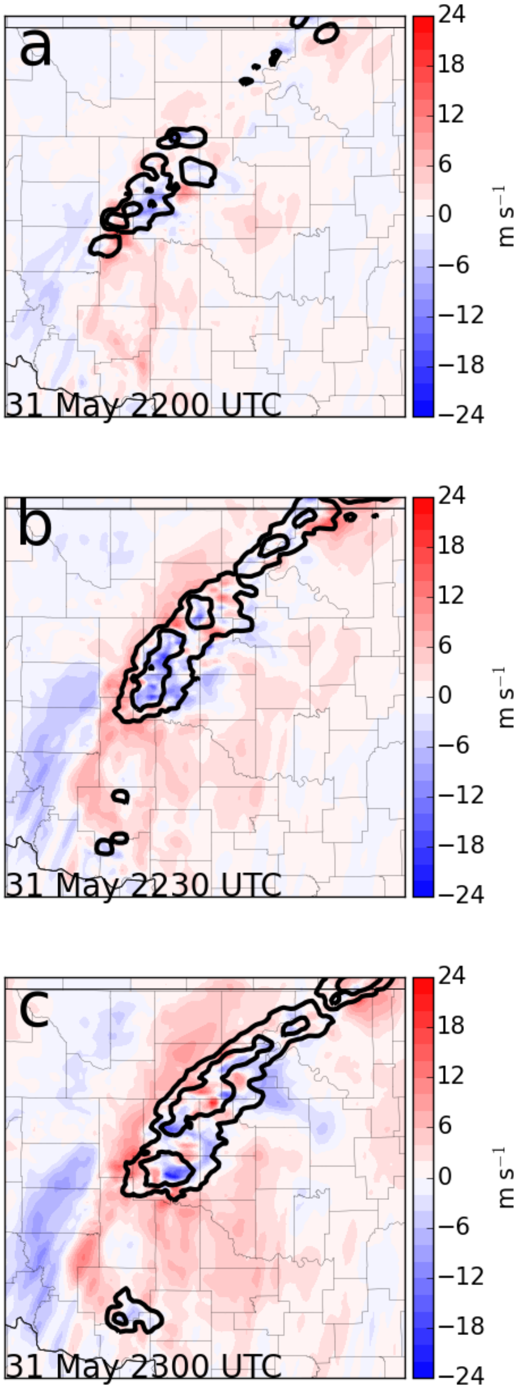

Figure 4.6. 31 May 2013 ensemble mean analysis 0-6 km vertical wind shear difference in m s^{-1} from 2130 UTC due to convection (filled) and low-level reflectivity at (a) 2200 UTC (b) 2230 UTC (c) 2300 UTC.

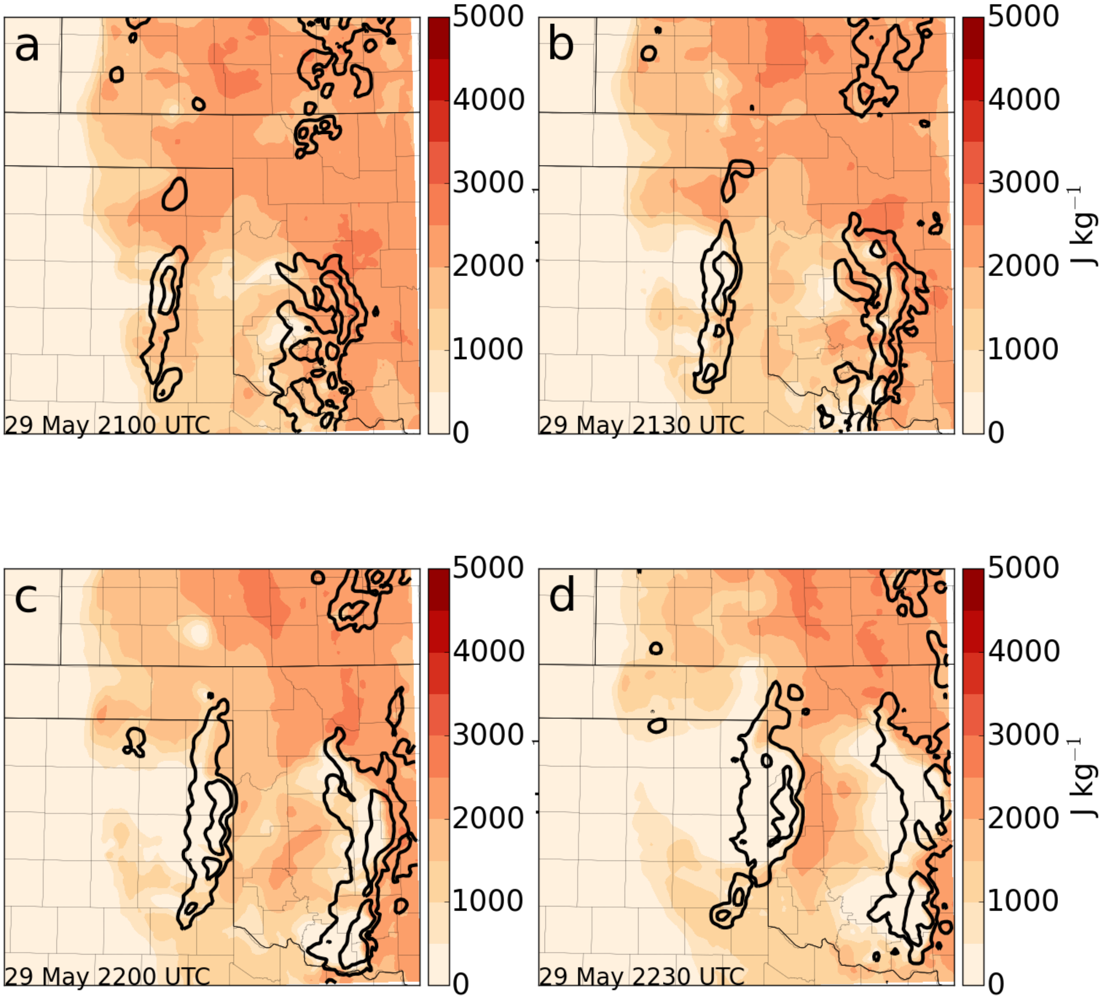

Figure 4.7. Ensemble mean analysis CAPE in J kg^{-1} (filled) and low-level reflectivity (black contours) on 29 May 2013 at (a) 2100 UTC (b) 2130 UTC (c) 2200 UTC (d) 2230 UTC.

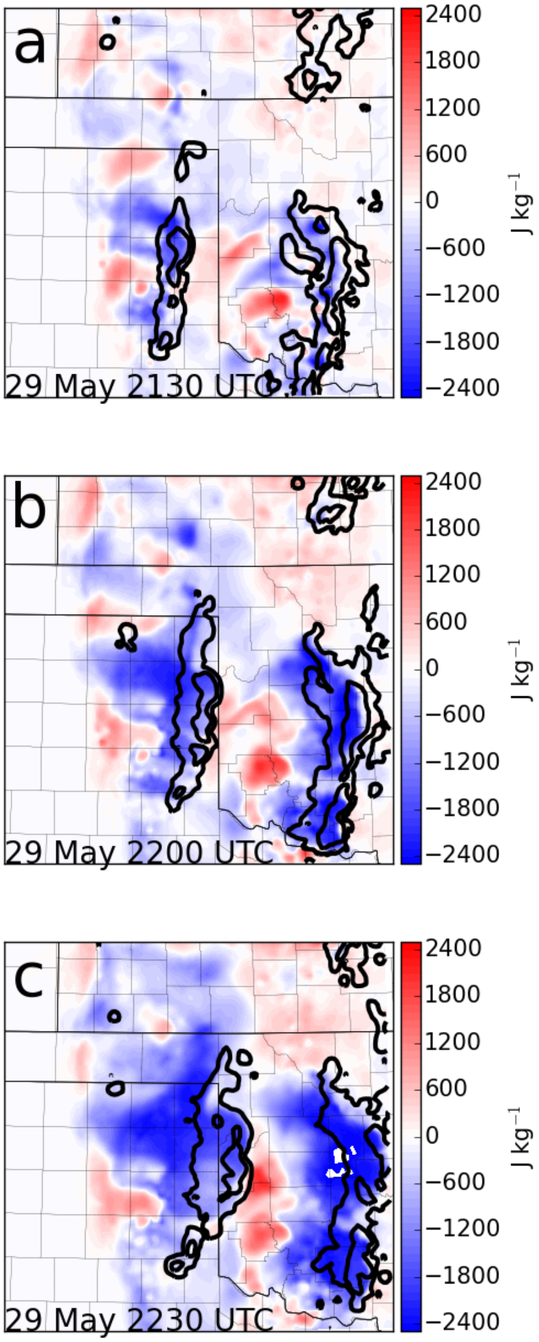

Figure 4.8. 29 May 2013 ensemble mean analysis CAPE difference in J kg^{-1} from 2100 UTC due to convection (filled) and low-level reflectivity at (a) 2130 UTC (b) 2200 UTC (c) 2230 UTC.

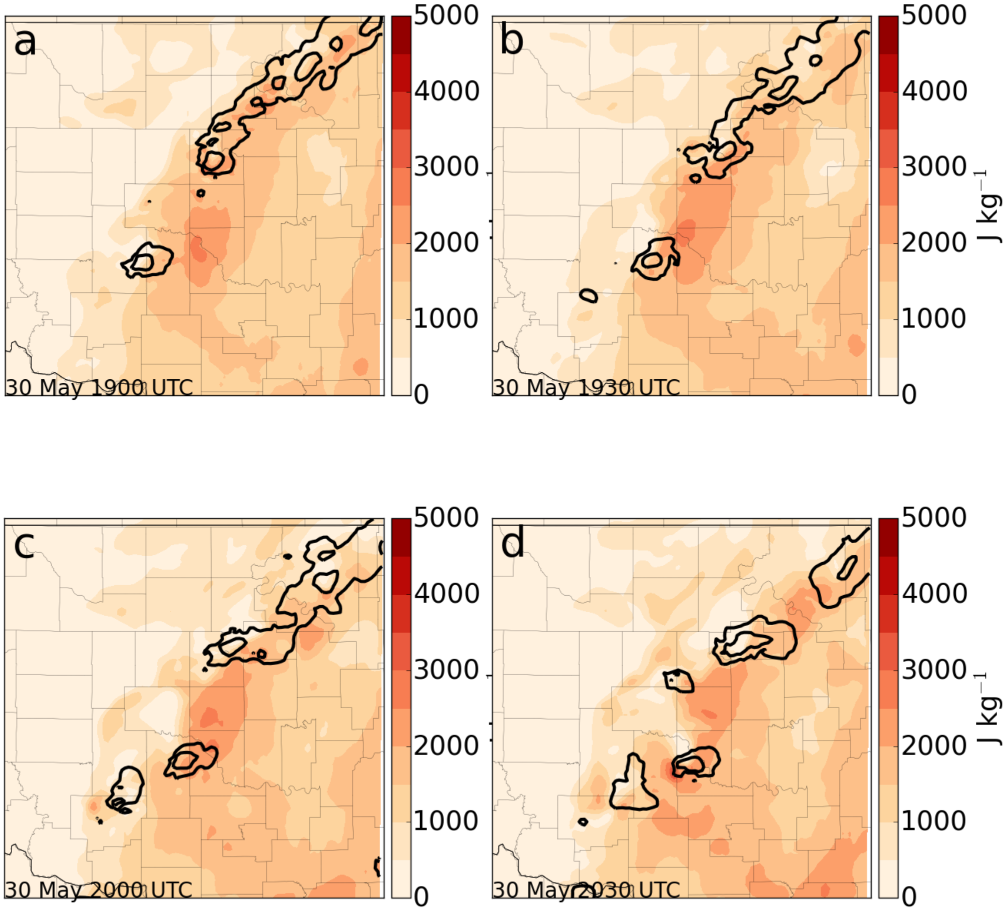

Figure 4.9. Ensemble mean analysis CAPE in J kg^{-1} (filled) and low-level reflectivity (black contours) on 30 May 2013 at (a) 1900 UTC (b) 1930 UTC (c) 2000 UTC (d) 2030 UTC.

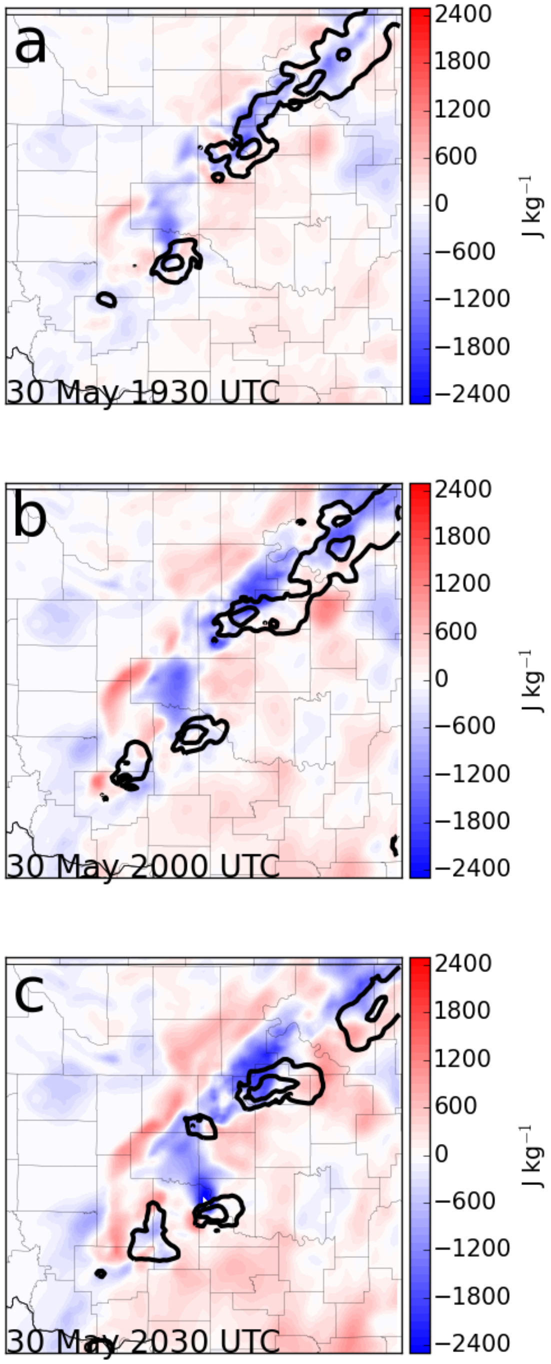

Figure 4.10. 30 May 2013 ensemble mean analysis CAPE difference in J kg^{-1} from 1900 UTC due to convection (filled) and low-level reflectivity at (a) 1930 UTC (b) 2000 UTC (c) 2030 UTC

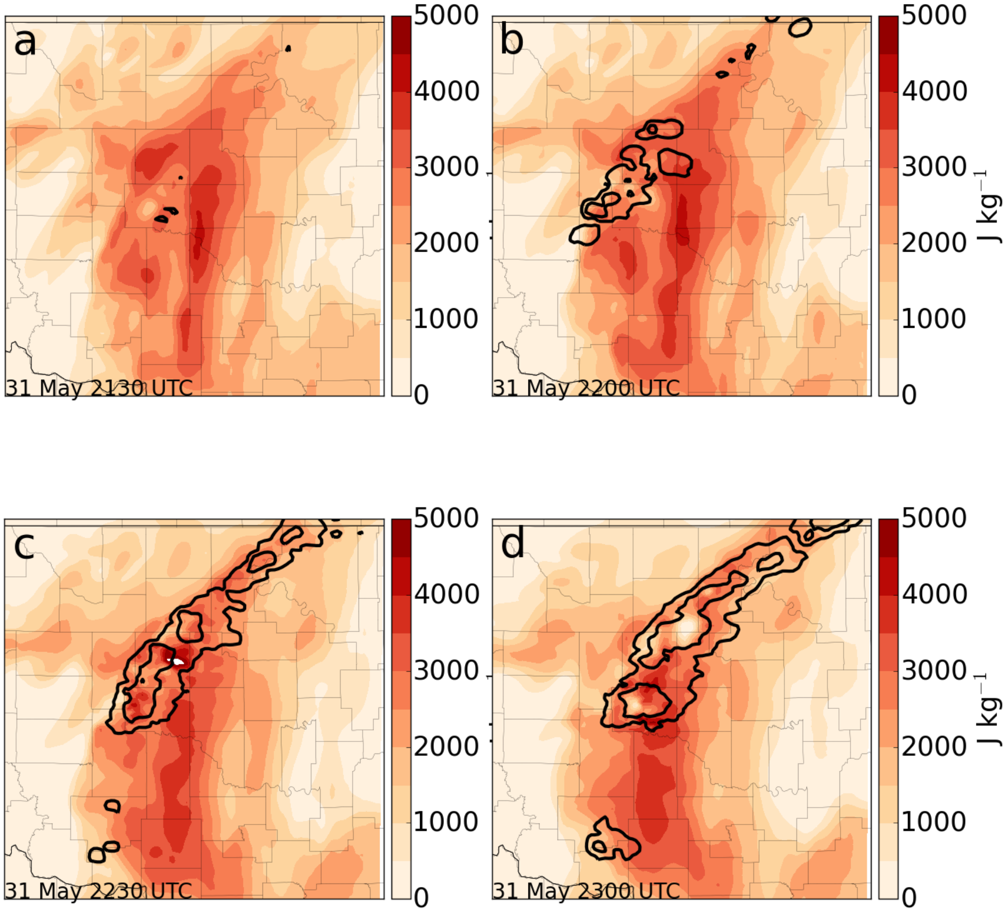

Figure 4.11. Ensemble mean analysis CAPE in J kg^{-1} (filled) and low-level reflectivity (black contours) on 31 May 2013 at (a) 2130 UTC (b) 2200 UTC (c) 2230 UTC (d) 2300 UTC.

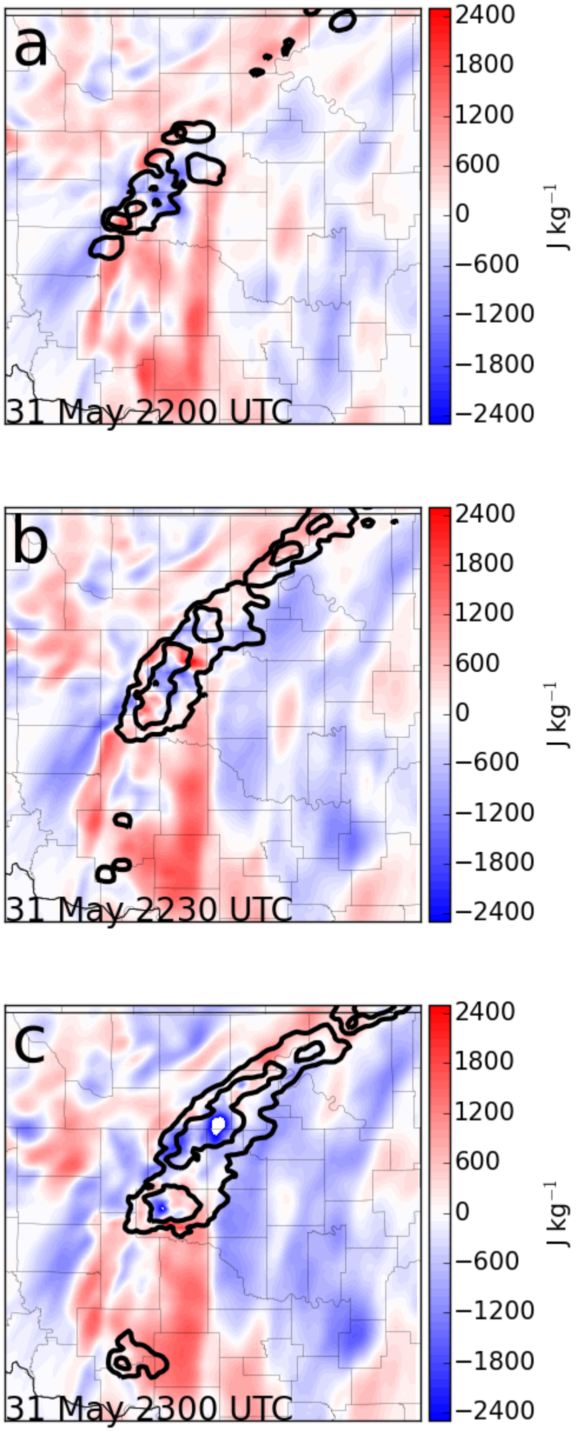

Figure 4.12. 31 May 2013 ensemble mean analysis CAPE difference in J kg^{-1} from 2130 UTC due to convection (filled) and low-level reflectivity at (a) 2200 UTC (b) 2230 UTC (c) 2300 UTC.

4.2 Cold pools

Cold pool development is a storm feature known to impact the surrounding environment (Trapp and Woznicki 2017). Ensemble mean analyses of lowest model level temperature reveal cold pool development in all three cases. The most notable cold pool develops on 29 May in the wake of the MCS in the Texas Panhandle (Fig. 4.13). The cold pool surges to the west, overtaking the warm, dry airmass behind the dryline. The temperature decreases by nearly 10 ^{o}C within the cold pool over short time periods (Fig. 4.14). It should be noted the region of temperature reduction is similar to the region of reduction of CAPE (Fig. 4.8) as expected.

A small cold pool develops on 30 May in the wake of the target supercell, leaving behind a region of cooler temperatures (Figs. 4.15 and 4.16). This cold pool is less evident than the 29 May cold pool, as lowest model level temperatures only decrease by ~5 ^{o}C. The resultant cold pool of the 31 May supercell is much stronger (cooler), where temperatures decrease by ~10 ^{o}C over the period depicted (Figs. 4.17 and 4.18). It is curious that low-level temperature decreases to the south of the supercell (Fig. 4.18c) while CAPE increases in this same region (Fig. 4.12b). The increase in CAPE is likely due to environmental cooling aloft (not shown).

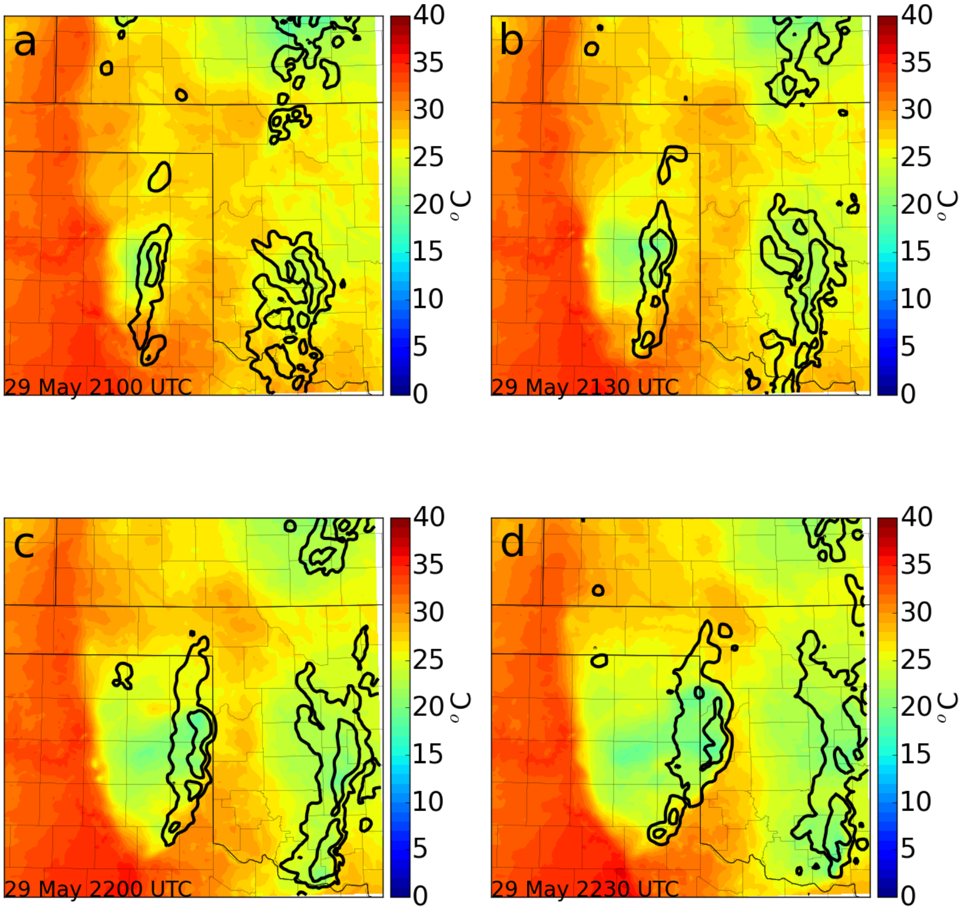

Figure 4.13. Ensemble mean analysis lowest model level temperature in ^{o}C (filled) and low-level reflectivity (black contours) on 29 May 2013 at (a) 2100 UTC (b) 2130 UTC (c) 2200 UTC (d) 2230 UTC.

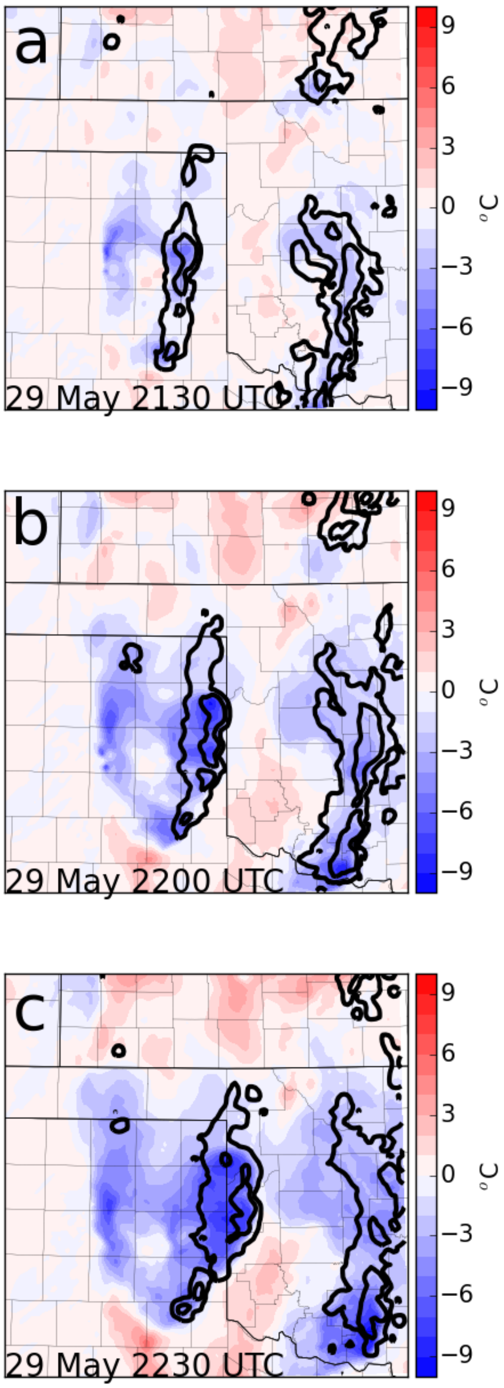

Figure 4.14. 29 May 2013 ensemble mean analysis lowest model level temperature difference in ^{o}C from 2100 UTC due to convection (filled) and low-level reflectivity at (a) 2130 UTC (b) 2200 UTC (c) 2230 UTC.

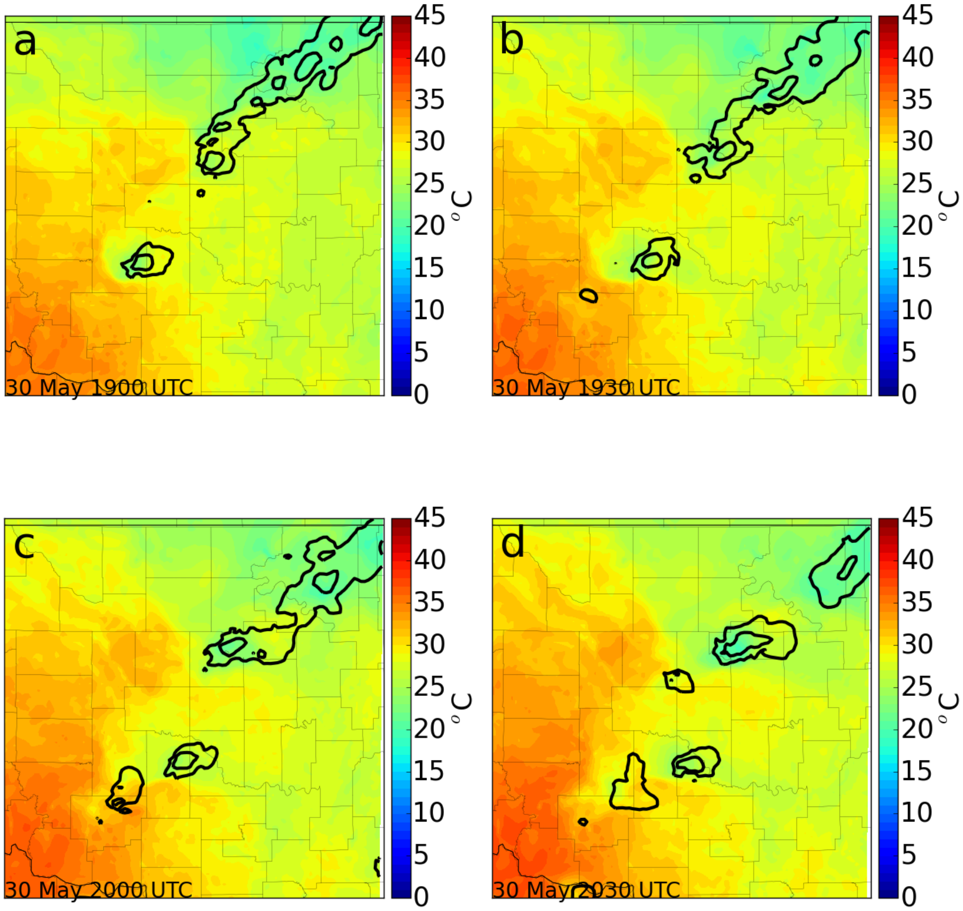

Figure 4.15. Ensemble mean analysis lowest model level temperature in ^{o}C (filled) and low-level reflectivity (black contours) on 30 May 2013 at (a) 1900 UTC (b) 1930 UTC (c) 2000 UTC (d) 2030 UTC.

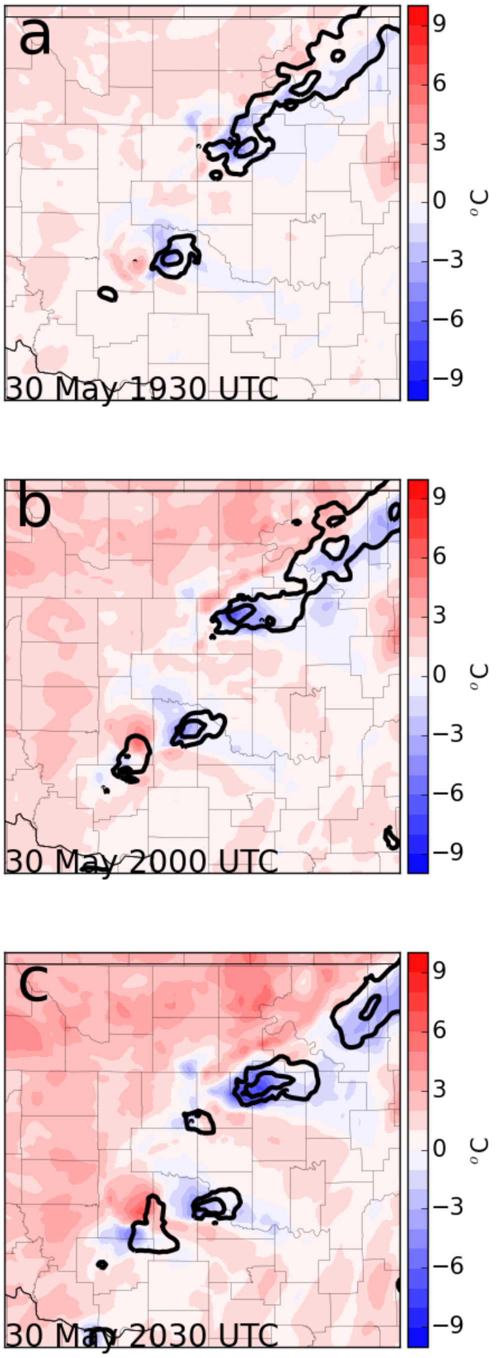

Figure 4.16. 30 May 2013 ensemble mean analysis lowest model level temperature difference in ^{o}C from 1900 UTC due to convection (filled) and low-level reflectivity at (a) 1930 UTC (b) 2000 UTC (c) 2030 UTC.

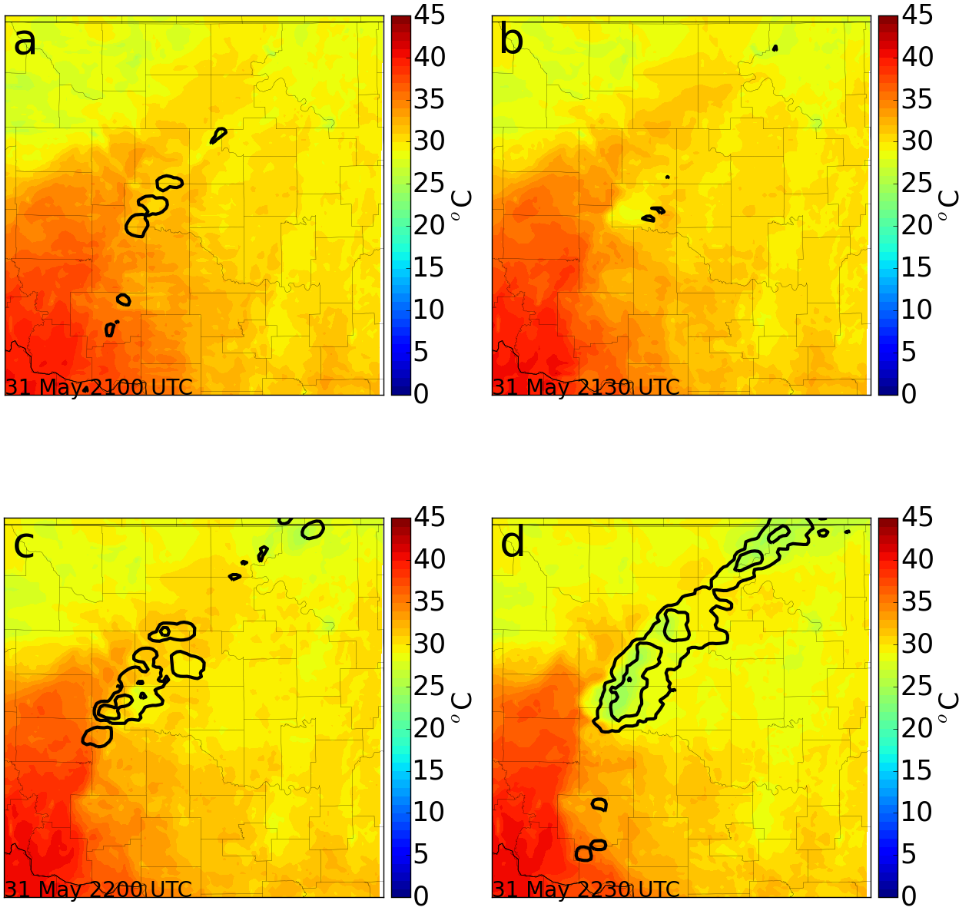

Figure 4.17. Ensemble mean analysis lowest model level temperature in °C (filled) and low-level reflectivity (black contours) on 31 May 2013 at (a) 2130 UTC (b) 2200 UTC (c) 2230 UTC (d) 2300 UTC.

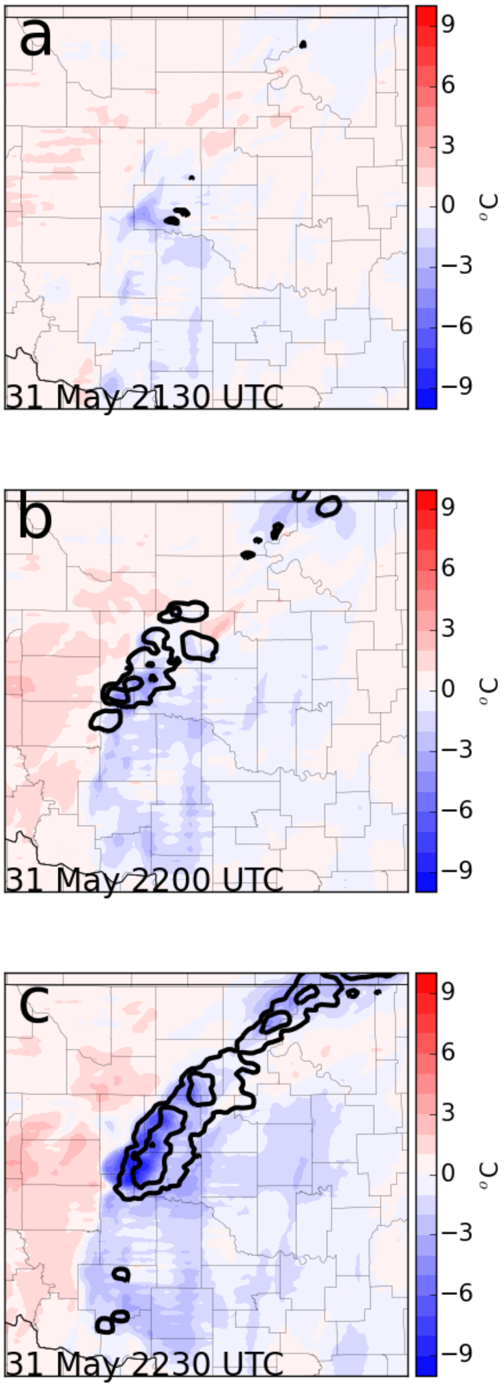

Figure 4.18. 31 May 2013 ensemble mean analysis lowest model level temperature difference in °C from 2130 UTC due to convection (filled) and low-level reflectivity at (a) 2200 UTC (b) 2230 UTC (c) 2300 UTC.

4.3 Upper troposphere

Impacts by convection also occur within the upper troposphere. On 29 May, the MCS was influenced by an upper-level vorticity maximum seen to the west of the anvil. (Fig. 4.19). The changes in anvil wind speeds are somewhat disorganized, but there appears to be a distinct, coherent region of acceleration to the northeast of the anvil and deceleration to the south and southeast over this 90 minute period (Fig. 4.20). With the background environmental flow being southerly, these changes in wind speed are consistent with upper-level storm outflow. These wind speed increases could possibly enhance synoptic-scale jet streaks, which would affect further convection development. On 30 May, the winds decelerate within the anvil region of the supercell (Figs. 4.21 and 4.22), where the upper-level flow was predominantly zonal. This deceleration is likely due to stagnation points on the upwind side of storms.

Upper-level deceleration is also seen on the upwind side of the 31 May supercell (Figs. 4.23 and 4.24). This event also features zonal upper-level flow and weak large-scale forcing. Wind accelerates toward the downwind side of the anvil, potentially enhanced by strong upper-level outflow from the updraft. This enhancement extends across the remainder of the anvil to the east and is even visible outside the anvil (Fig. 4.24c).

The 250 hPa temperature generally increases within the MCS anvil on 29 May. This warmed air also extends outside the anvil region (Fig. 4.26c). Convection has little effect on 250 hPa temperature on 30 May as temperatures within the anvil region do not drastically change over the displayed time period. However, the more intense convection on 31 May has significant upper-level warming (> 5 ^{o}C) within the anvil region (Figs. 4.29 and 4.30) similar to that seen with the 29 May MCS . This warming also extends outside the anvil region which contradicts Perkey and Maddox (1985) where cooling is noted at 200 hPa due to vertical motions and adiabatic cooling. However, warming is noted within the mid-troposphere due to latent heat release.

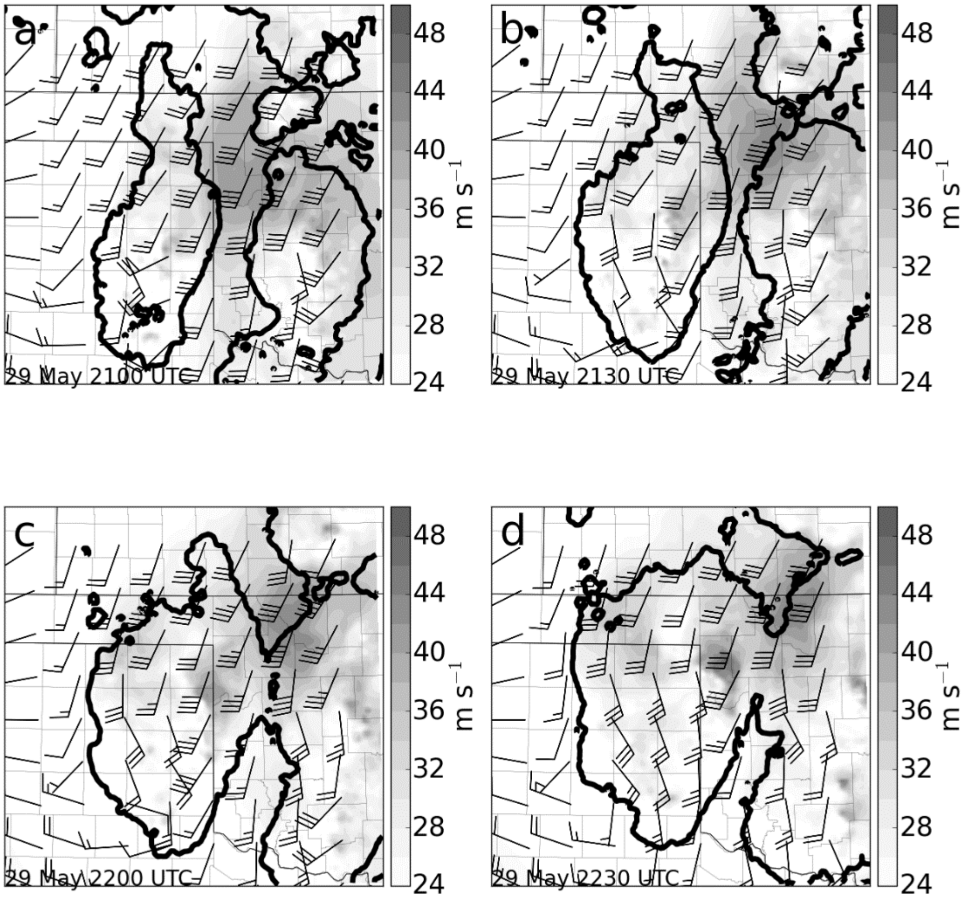

Figure 4.19. Ensemble mean analysis 250 hPa wind speed (shaded) in m s^{-1} and wind barbs on 29 May 2013 at (a) 2100 UTC (b) 2130 UTC (c) 2200 UTC (d) 2230 UTC. The ensemble analysis cloud outline is denoted by the thick black line and is determined using the method described by Kerr et al. (2015).

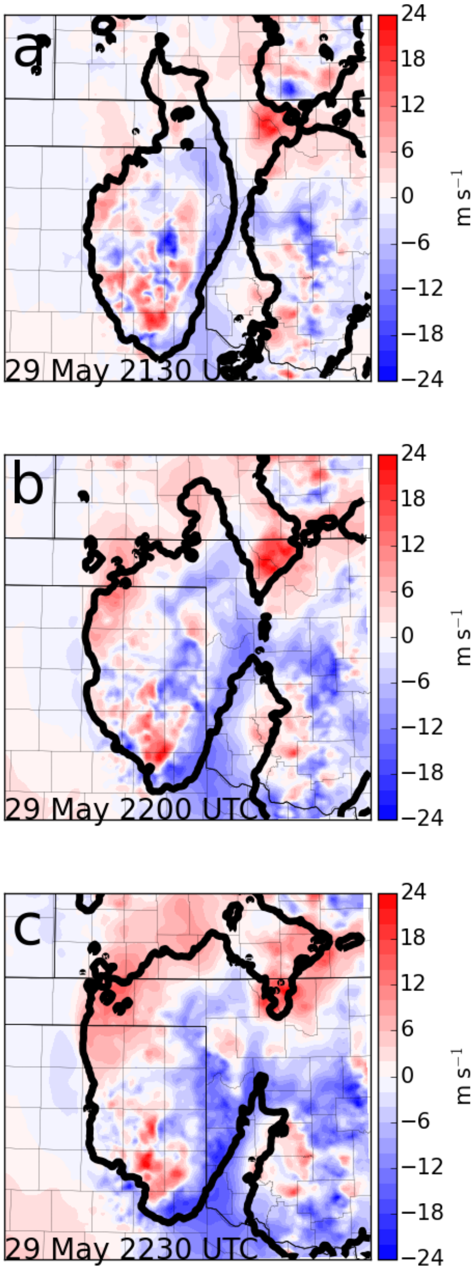

Figure 4.20. Ensemble mean analysis 250 hPa wind speed difference in m s^{-1} from 29 May 2100 UTC (filled) and cloud outline (thick black line) at (a) 2130 UTC (b) 2200 UTC (c) 2230 UTC.

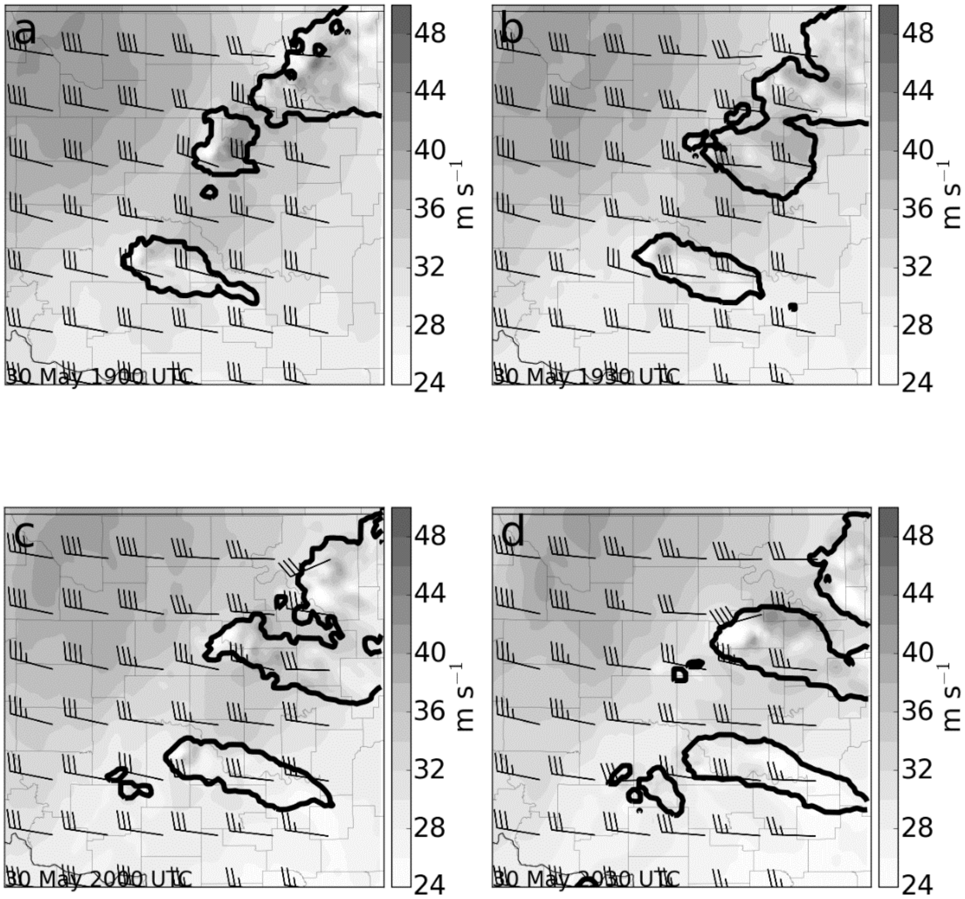

Figure 4.21. Ensemble mean analysis 250 hPa wind speed (shaded) in m s^{-1} and wind barbs on 30 May 2013 at (a) 1900 UTC (b) 1930 UTC (c) 2000 UTC (d) 2030 UTC. The ensemble analysis cloud outline is denoted by the thick black line and is determined using the method described by Kerr et al. (2015).

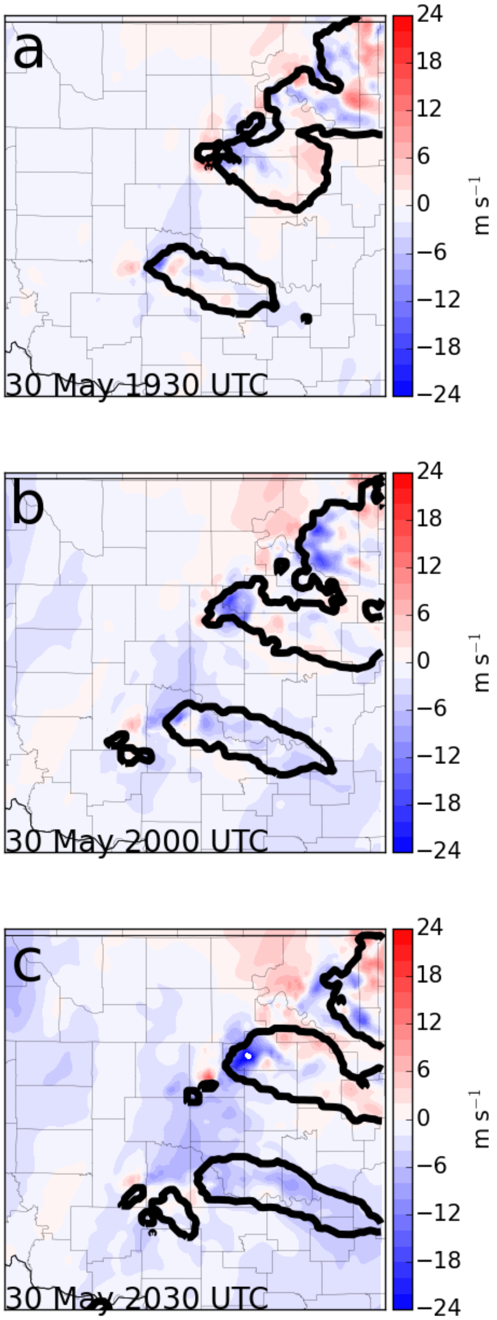

Figure 4.22. Ensemble mean analysis 250 hPa wind speed difference in m s^{-1} from 30 May 1900 UTC (filled) and cloud outline (thick black line) at (a) 1930 UTC (b) 2000 UTC (c) 2030 UTC.

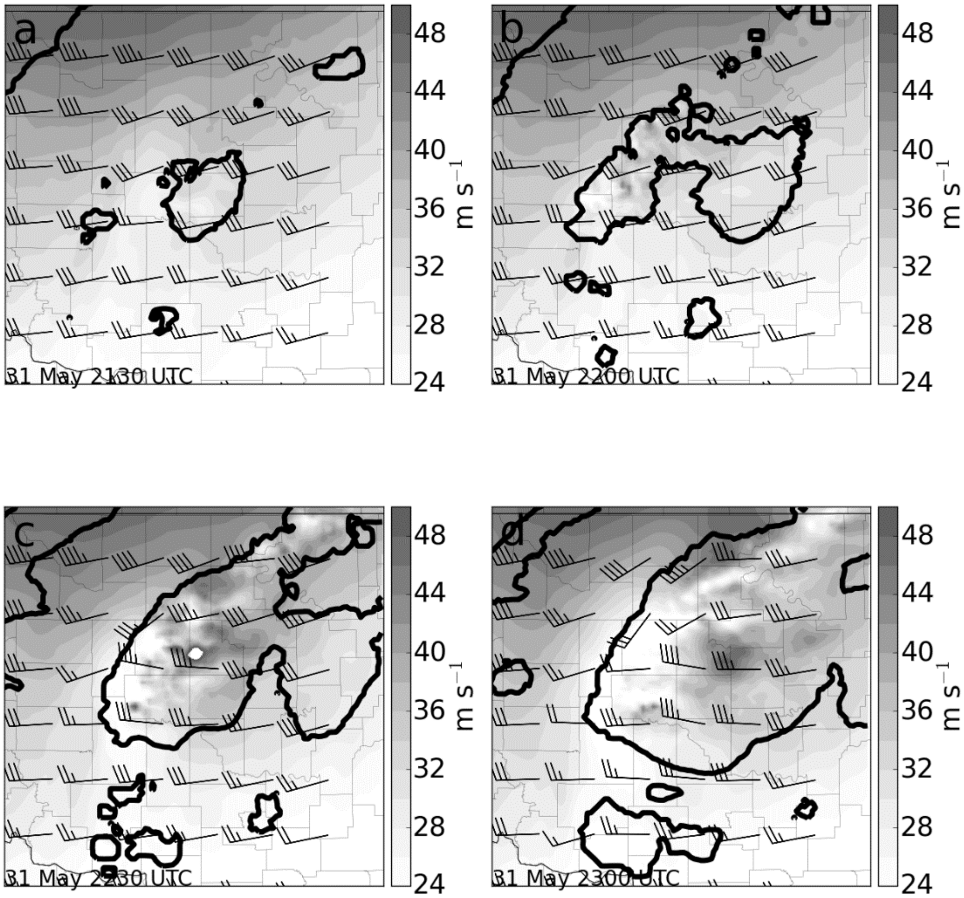

Figure 4.23. Ensemble mean analysis 250 hPa wind speed (shaded) in m s^{-1} and wind barbs on 31 May at (a) 2130 UTC (b) 2200 UTC (c) 2230 UTC (d) 2300 UTC. The ensemble analysis cloud outline is denoted by the thick black line.

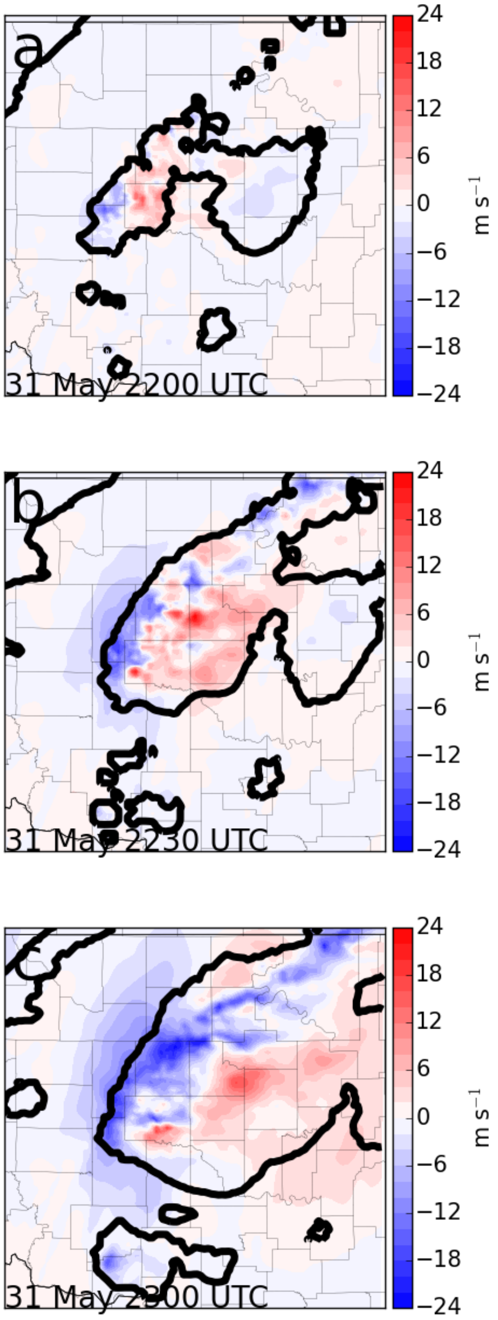

Figure 4.24. Ensemble mean analysis 250 hPa wind speed difference in m s^{-1} from 31 May 2130 UTC (filled) and cloud outline (thick black line) at (a) 2200 UTC (b) 2230 UTC (c) 2300 UTC.

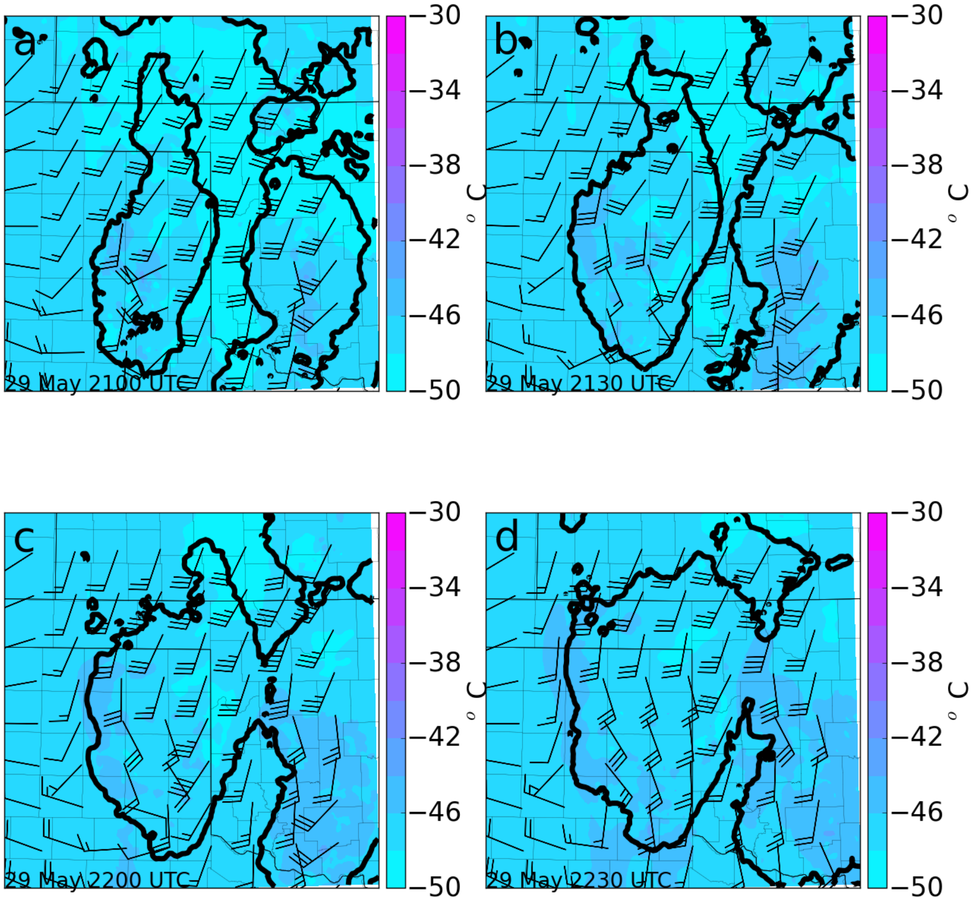

Figure 4.25. Ensemble mean analysis 250 hPa temperature in ^{o}C (shaded) and wind barbs on 29 May 2013 at (a) 2100 UTC (b) 2130 UTC (c) 2200 UTC (d) 2230 UTC. The ensemble analysis cloud outline is denoted by the thick black line.

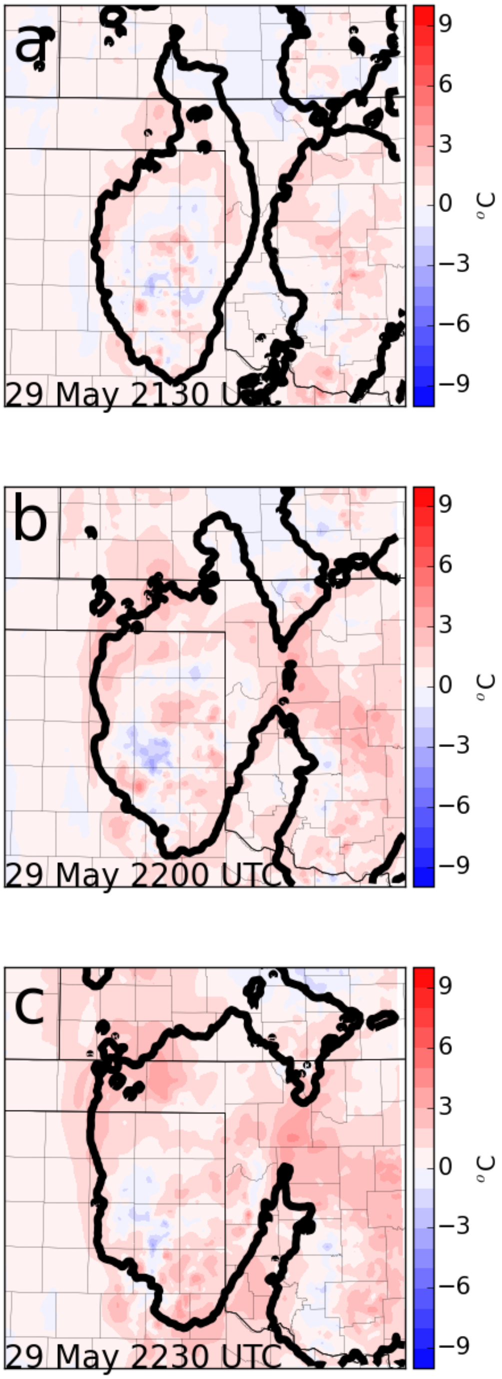

Figure 4.26. Ensemble mean analysis 250 hPa temperature difference in ^{o}C from 29 May 2100 UTC (filled) and cloud outline (thick black line) at (a) 2130 UTC (b) 2200 UTC (c) 2230 UTC.

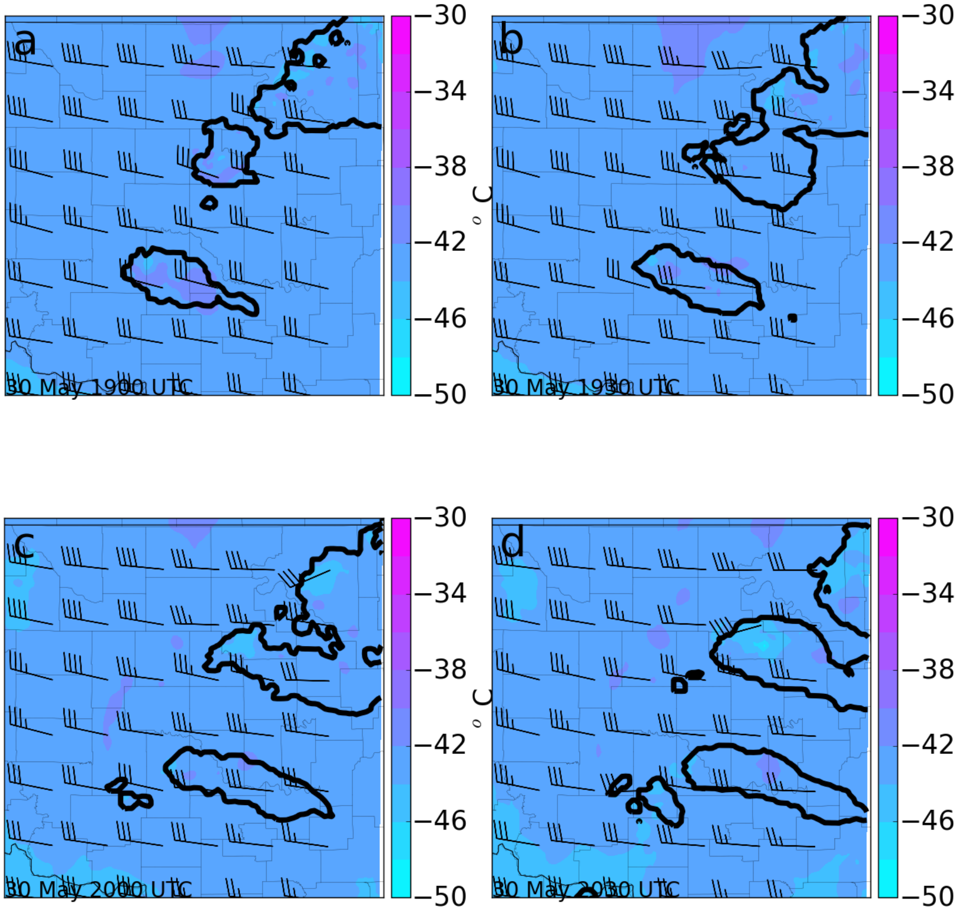

Figure 4.27. Ensemble mean analysis 250 hPa temperature in °C and wind barbs on 30 May 2013 at (a) 1900 UTC (b) 1930 UTC (c) 2000 UTC (d) 2030 UTC. The ensemble analysis cloud outline is denoted by the thick black line.

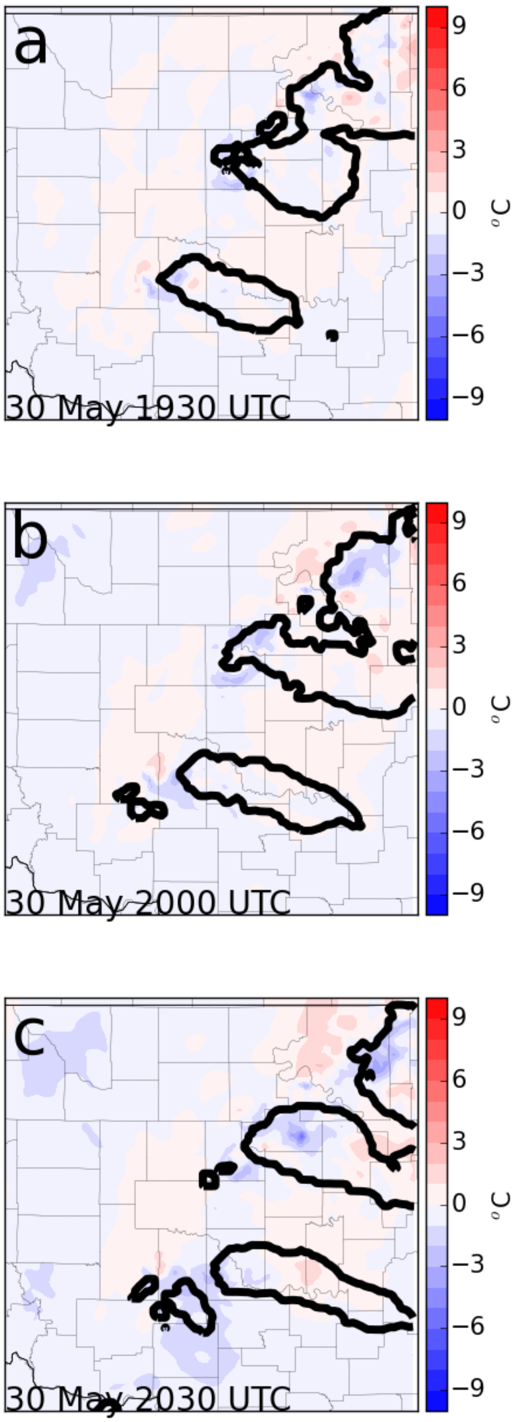

Figure 4.28. Ensemble mean analysis 250 hPa temperature difference in °C from 30 May 1900 UTC (filled) and cloud outline (thick black line) at (a) 1930 UTC (b) 2000 UTC (c) 2030 UTC.

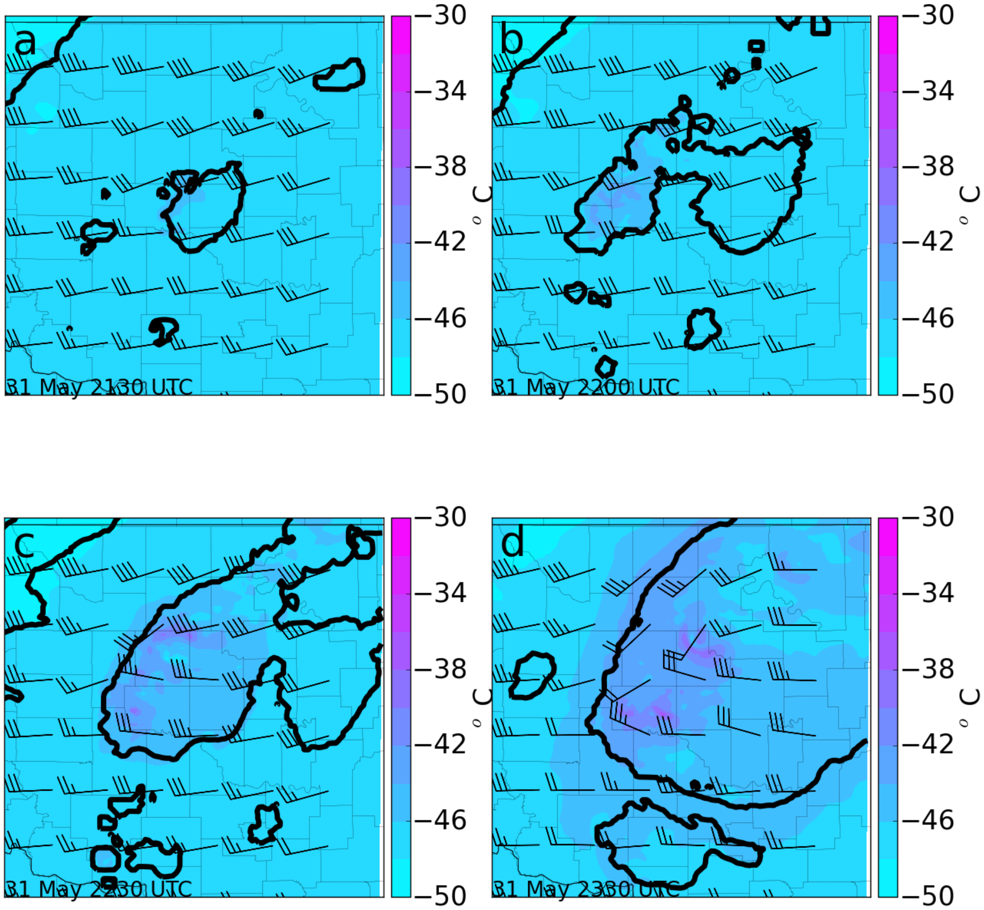

Figure 4.29. Ensemble mean analysis 250 hPa temperature in ^{o}C and wind barbs on 31 May at (a) 2130 UTC (b) 2200 UTC (c) 2230 UTC (d) 2300 UTC. The ensemble analysis cloud outline is denoted by the thick black line.

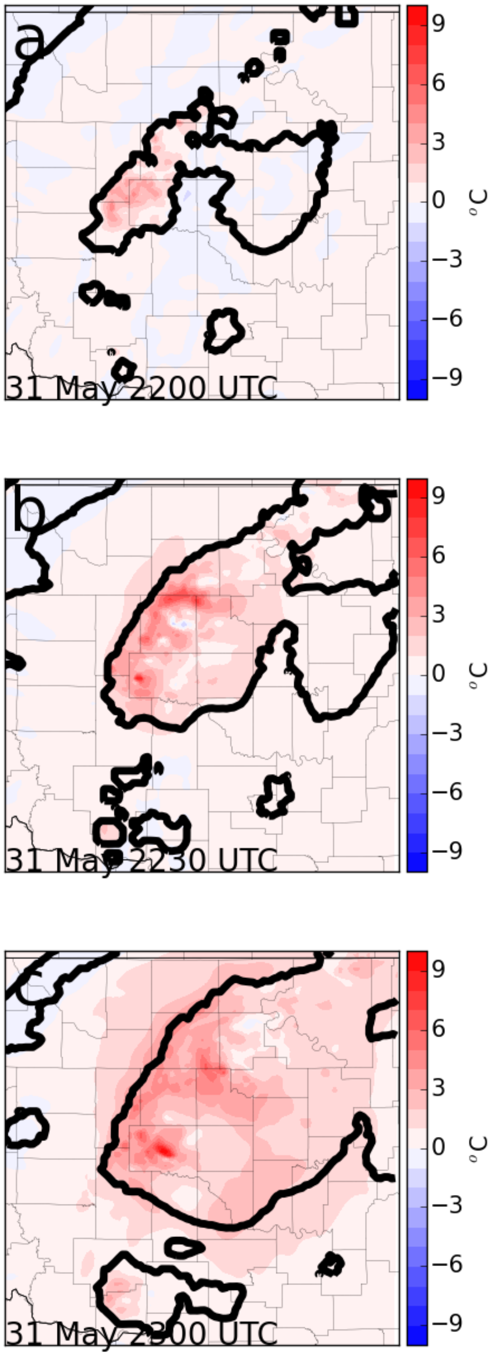

Figure 4.30. Ensemble mean analysis 250 hPa temperature difference in °C from 31 May 2130 UTC (filled) and cloud outline (thick black line) at (a) 2200 UTC (b) 2230 UTC (c) 2300 UTC.

4.4 Discussion and conclusions

These results further support the notion that convection can have significant impacts on the surrounding environment. This is particularly evident for environmental wind shear and CAPE. Closer examination of the model output indicates that shear increases within supercell inflow regions due to an enhanced pressure gradient (not shown). For the 29 May MCS, shear enhances in the wake of the storm because of the easterly outflow. CAPE also is enhanced within supercell inflow regions, where environmental cooling aloft is the main contributor to this effect. In the wake of the MCS, CAPE decreases in association with cold pool formation.

Cold pool development is most notable in the 29 and 31 May cases. The 30 May supercell cold pool was not as large or cold relative to the environment. The cold pool of the 29 May MCS to the east of the target MCS interferes with the target MCS's intensity and longevity, revealing how storm-storm interactions can affect convection development and evolution. Convection also influences the upper-tropospheric winds by slowing environmental winds on the upwind side. Winds also are enhanced within upper-level outflow. These effects may alter the synoptic-scale flow and potentially affect convection evolution on subsequent days (Stensrud 1996).

Future studies should investigate these effects in other cases as well as effects on other environmental variables. In the next chapter, the effects of some of these modifications on further convection evolution are analyzed.

Chapter 5: Ensemble sensitivity analysis (ESA) applied to convective-scale forecasts

ESA is applied to ensemble forecasts on 29, 30, and 31 May. Since this analysis is applied to forecasts of individual thunderstorms, storm variables are used as forecast metrics (e.g., radar reflectivity, updraft helicity, accumulated rainfall, etc.) while near-storm environment variables are used as initial condition metrics (e.g., vertical wind shear, low- and mid-level moisture, etc.) via the technique outlined in Chapter 2. Table 5.1 lists the metrics used on each day along with the corresponding figure number that displays the resulting sensitivities.

5.1 29 May MCS results

Several forecast metrics relevant to an MCS are used in an ESA as listed in Table 5.1. All forecasts on this day are initialized at 2130 UTC in order to allow sufficient storm spin-up via radar data assimilation beginning at 1700 UTC (Table 2.2). Sensitivity of storm-averaged reflectivity (> 20 dBZ) to 850 hPa wind speed reveals a negative sensitivity just east of the initial condition storm location (Fig. 5.1). Magnitudes of sensitivity exceed 0.5 dBZ (m s^{-1})$^{-1}$ in this region for both a one hour forecast (Fig. 5.1a) and two hour forecast (Fig. 5.1c). These sensitivities indicate that slower wind speeds in these areas (which are generally downstream of the initial condition storm location) will result in higher storm-averaged reflectivity. A notable area of positive sensitivity is present to the west of the convective system, associated with the eastward moving dryline in the Texas Panhandle. These results suggest faster winds behind the dryline will lead to increased averaged reflectivity of the target storm.

Application of statistical significance test (Fig. 5.1b,d) eliminates nearly all of the sensitivities, suggesting that they may be a result of ensemble sampling error.

Forecast average reflectivity is also sensitive to initial condition 850 hPa temperature (Fig. 5.2). Reflectivity is predominantly positively sensitive to 850 hPa temperature, with sensitivity values approaching 2 dBZ $(^{o}C)^{-1}$ in areas that are east of the initial storm location. This means that warmer 850 hPa temperatures are associated with greater forecast average reflectivity. Application of the significance test reveals broad areas of positive sensitivity (Fig. 5.2b,d). Reflectivity sensitivity to 850 hPa water vapor mixing ratio also shows positive sensitivity within the inflow region to the east and southeast of the MCS (Fig. 5.3a,c). The sensitivities to temperature and moisture suggest that larger CAPE to the east of the storm yields larger reflectivity. Large negative sensitivities are noted to the west behind the dryline, suggesting that drier air results in higher average reflectivity, perhaps suggesting that a more intense dryline would influence storm intensity. Reflectivity is also found to be sensitive to the zonal component vertical wind shear over various depths. In the case of 0-1 km shear (hereafter SHR01), reflectivity is positively sensitive within the inflow region of the initial condition storm location and positively sensitive to SHR01 behind the dryline (Fig. 5.4). For 0-3 km shear (hereafter SHR03), reflectivity is also positively sensitive ahead of the MCS (Fig. 5.5).

For this MCS case, the low-level outflow winds are predominantly zonal. Since a goal of short-term convection forecasts is to better predict potential hazards to lives and property, sensitivities of forecast lowest model level zonal winds (hereafter LLWs) to various environmental variables are explored. LLWs are sensitive to SHR01 behind the dryline where sensitivities exceed 1.0 (Fig. 5.6). LLWs are negatively sensitive to SHR01 within the inflow region of the MCS, particularly for the two hour forecast (Fig. 5.6c,d). LLWs are also sensitive to 850 hPa temperature (Fig. 5.7). LLWs are positively sensitive slightly ahead of the initial condition storm location but negatively sensitive further east. This may reflect interference with the cold pool of the MCS to the east, where a colder cold pool moving from the east will quickly diminish the target MCS. There are large sensitivities to temperature within the dry airmass as values exceed 1 m s^{-1} $(^{o}C)^{-1}$. LLW sensitivity to 850 hPa water vapor mixing ratio is very small in most locations (Fig. 5.8). However, there is very large negative sensitivity to moisture behind the dryline (< -3 m s^{-1} $(g\ kg^{-1})^{-1}$). These results coupled with temperature sensitivities suggest warmer and drier air behind the dryline have some enhancement effect on low-level, possibly damaging winds.

Day	Forecast metric (*J*)	Initial condition (*x*)	Figure
29 May	Storm-averaged composite radar reflectivity	850 hPa wind speed	5.1
		850 hPa temperature	5.2
		850 hPa water vapor mixing ratio	5.3
		0-3 km wind shear	5.4
		0-1 km wind shear	5.5
	Storm-averaged lowest model level zonal winds	0-1 km wind shear	5.6
		850 hPa temperature	5.7
		850 hPa water vapor mixing ratio	5.8
30 May	Storm-averaged composite radar reflectivity	850 hPa water vapor mixing ratio	5.9
		700 hPa water vapor mixing ratio	5.10
		CAPE	5.11
	Storm-averaged 2-5 km UH	0-6 km wind shear	5.12
		850 hPa wind speed	5.13
		850 hPa temperature	5.14
31 May	Storm-averaged composite radar reflectivity	850 hPa water vapor mixing ratio	5.15
		700 hPa water vapor mixing ratio	5.16
		CAPE	5.17
	Storm-averaged accumulated rainfall	850 hPa water vapor mixing ratio	5.18
		700 hPa water vapor mixing ratio	5.19
	Storm-averaged 2-5 km UH	0-6 km wind shear	5.20
		850 hPa wind speed	5.21
		850 hPa temperature	5.22
	Storm-averaged 0-1 km UH	0-1 km wind shear	5.23

Table 5.1. List of scalar forecast metrics (*J*) and initial condition variables (*x*) for which ESA is applied on each day.

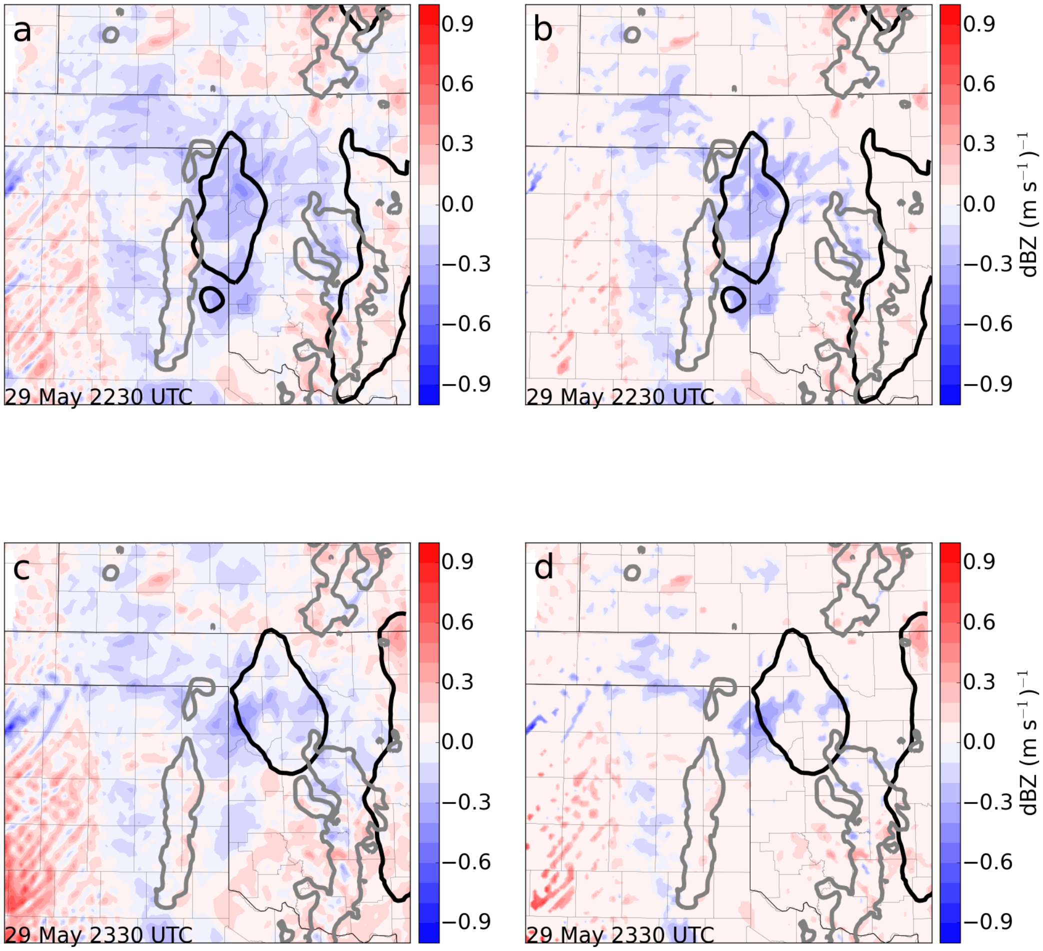

Figure 5.1. 29 May target storm averaged composite reflectivity (> 20 dBZ) sensitivity to initial condition 850 hPa wind speed in dBZ (m s^{-1})$^{-1}$ and ensemble mean forecasted reflectivity (20 dBZ; black contour) and ensemble mean initial condition reflectivity (20 dBZ; gray contour) for forecast times (a) 1-hour, valid 2230 UTC (b) 1-hour with statistical significance test (c) 2-hour, valid 2330 UTC (d) 2-hour with statistical significance test.

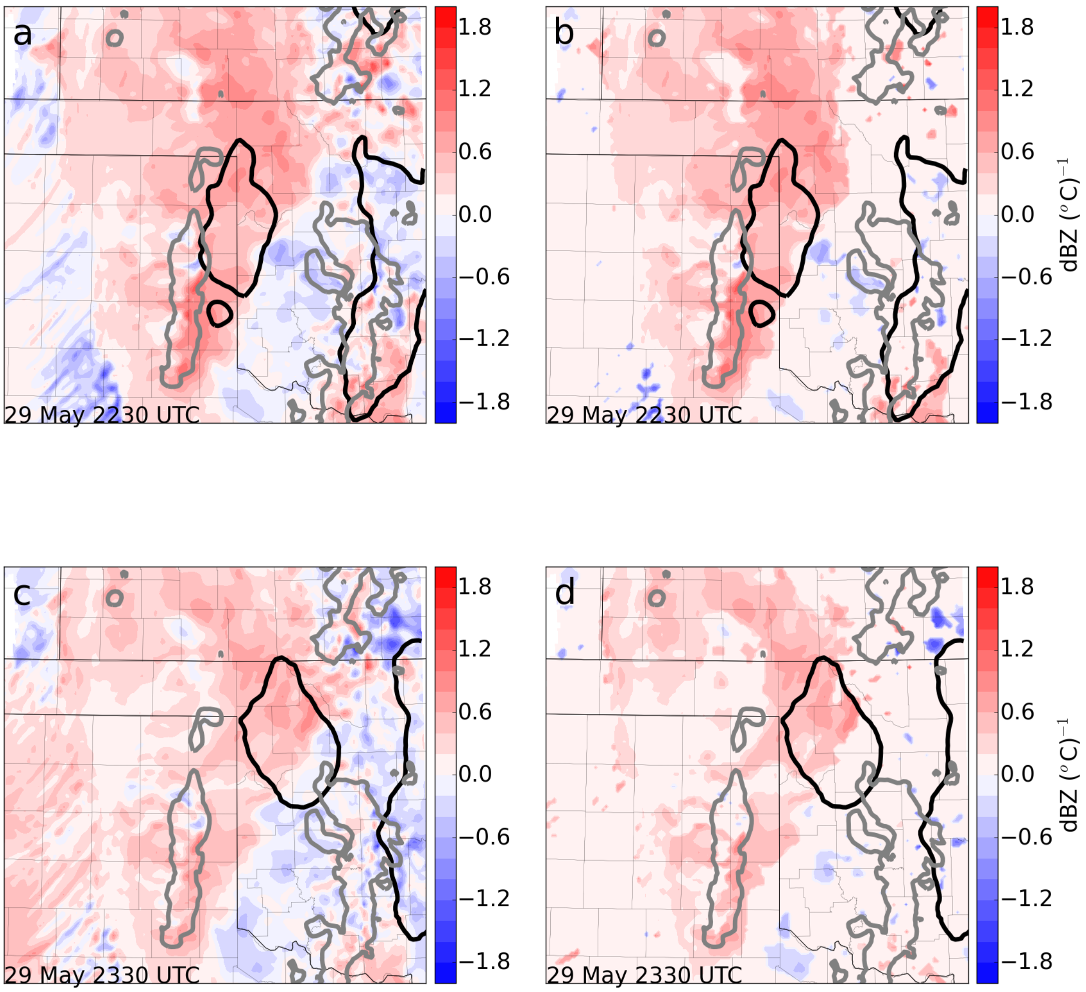

Figure 5.2. 29 May target storm averaged composite reflectivity (> 20 dBZ) sensitivity to initial condition 850 hPa temperature in dBZ (^{o}C)$^{-1}$ and ensemble mean forecasted reflectivity (20 dBZ; black contour) and ensemble mean initial condition reflectivity (20 dBZ; gray contour) for forecast times (a) 1-hour, valid 2230 UTC (b) 1-hour with statistical significance test (c) 2-hour, valid 2330 UTC (d) 2-hour with statistical significance test.

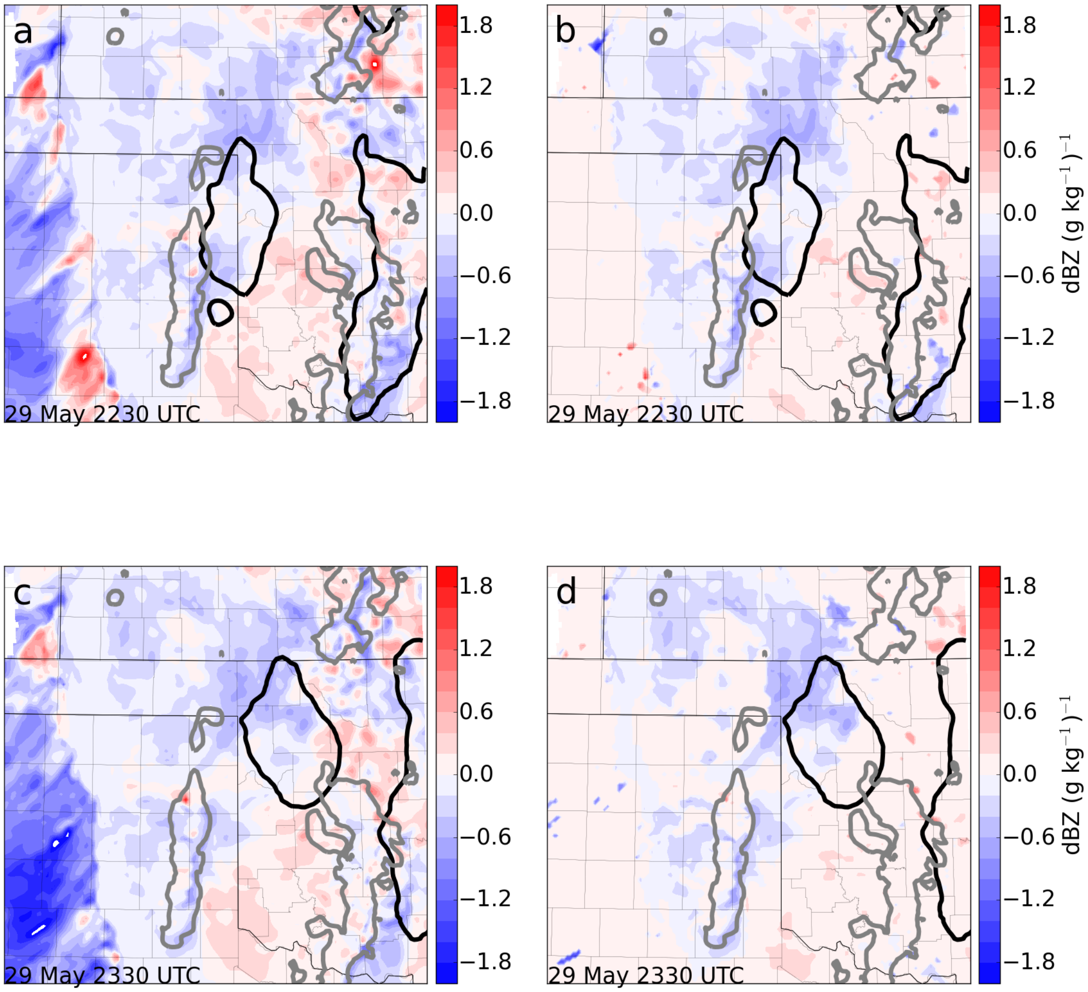

Figure 5.3. 29 May target storm averaged composite reflectivity (> 20 dBZ) sensitivity to initial condition 850 hPa water vapor mixing ratio in dBZ (g kg^{-1})$^{-1}$ and ensemble mean forecasted reflectivity (20 dBZ; black contour) and ensemble mean initial condition reflectivity (20 dBZ; gray contour) for forecast times (a) 1-hour, valid 2230 UTC (b) 1-hour with statistical significance test (c) 2-hour, valid 2330 UTC (d) 2-hour with statistical significance test.

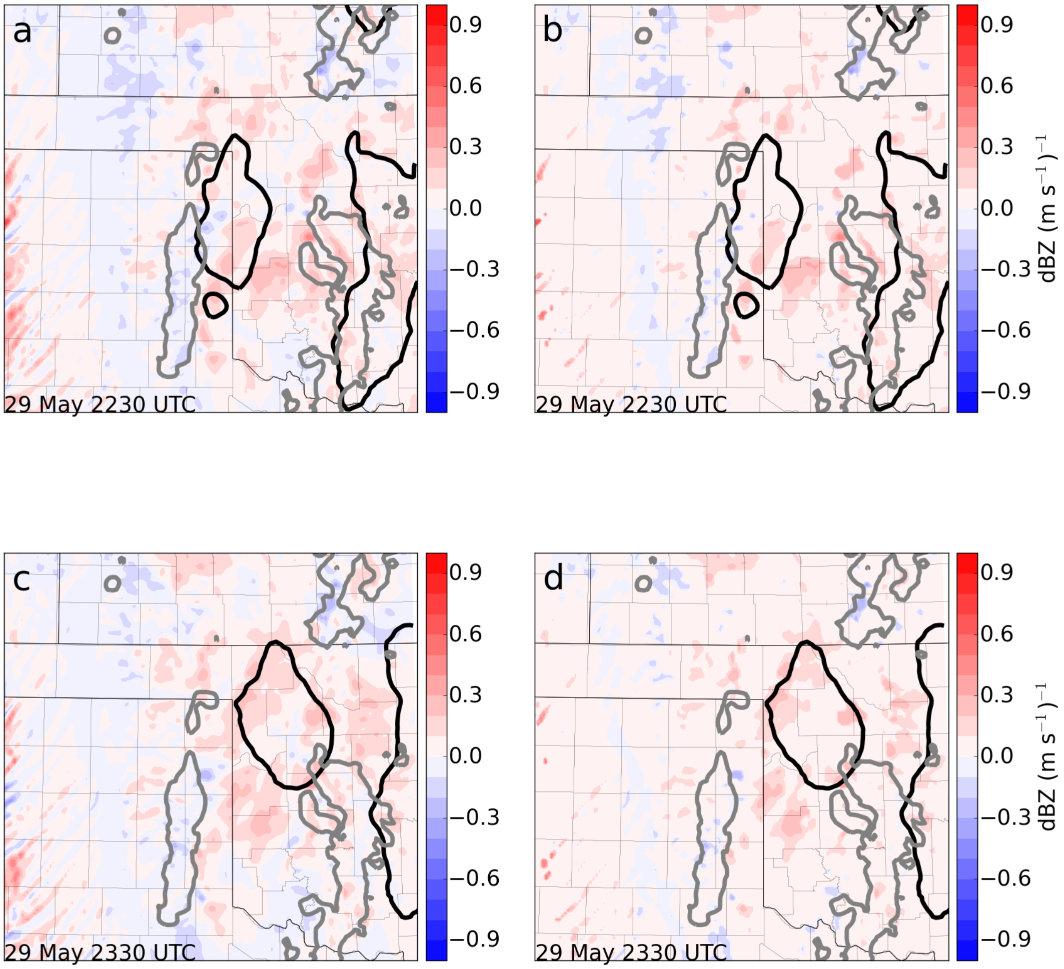

Figure 5.4. 29 May target storm averaged composite reflectivity (> 20 dBZ) sensitivity to initial condition SHR01 in dBZ (m s^{-1})$^{-1}$ and ensemble mean forecasted reflectivity (20 dBZ; black contour) and ensemble mean initial condition reflectivity (20 dBZ; gray contour) for forecast times (a) 1-hour, valid 2230 UTC (b) 1-hour with statistical significance test (c) 2-hour, valid 2330 UTC (d) 2-hour with statistical significance test.

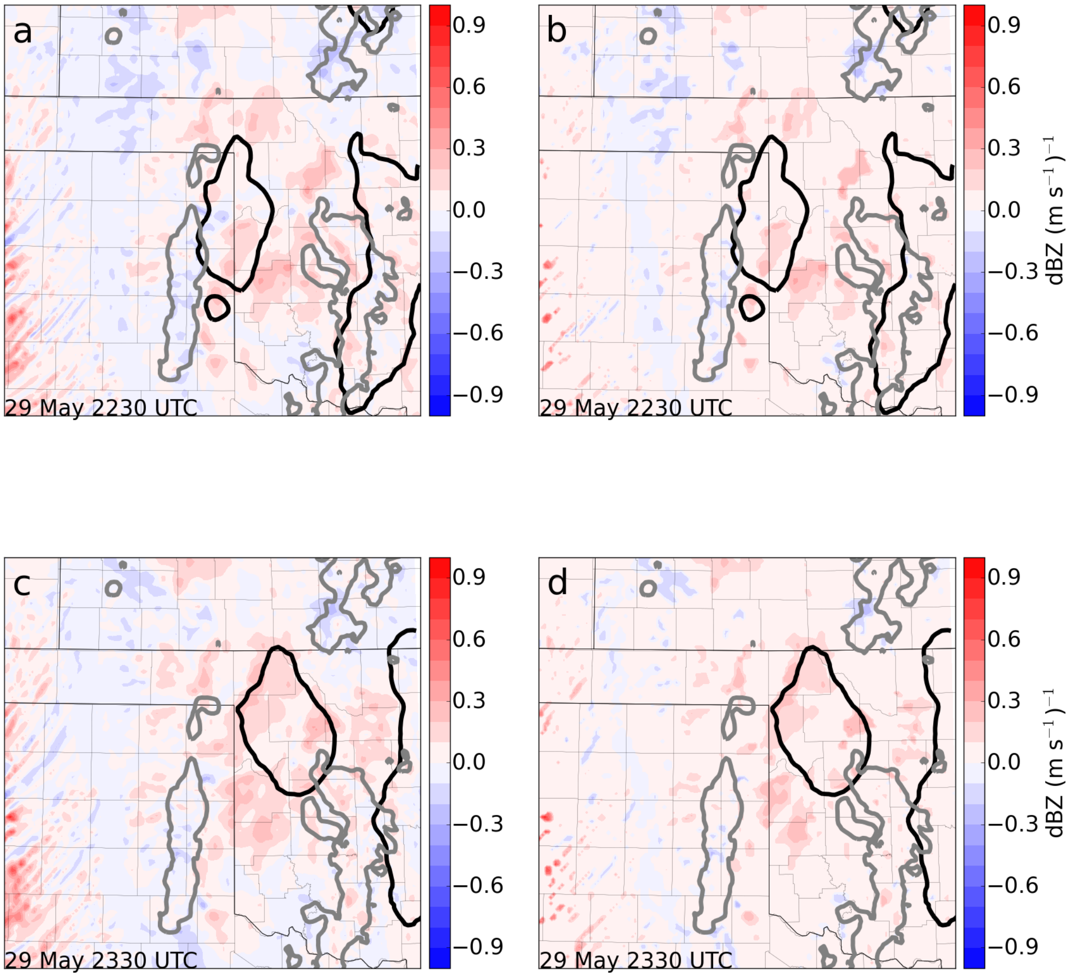

Figure 5.5. 29 May target storm averaged composite reflectivity (> 20 dBZ) sensitivity to initial condition SHR03 in dBZ (m s^{-1})$^{-1}$ and ensemble mean forecasted reflectivity (20 dBZ; black contour) and ensemble mean initial condition reflectivity (20 dBZ; gray contour) for forecast times (a) 1-hour, valid 2230 UTC (b) 1-hour with statistical significance test (c) 2-hour, valid 2330 UTC (d) 2-hour with statistical significance test.

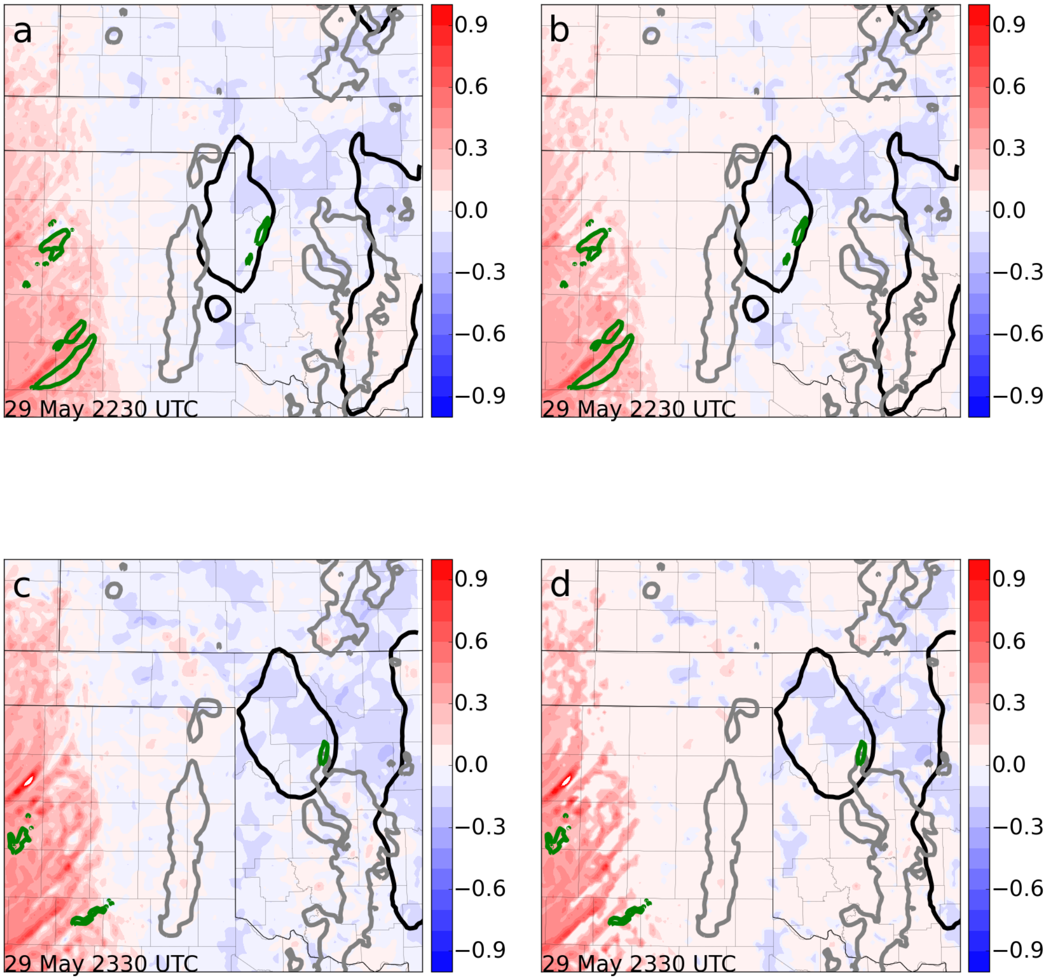

Figure 5.6. 29 May target storm averaged LLW (> 10 m s^{-1}) sensitivity to initial condition SHR01 (unitless) and ensemble mean forecasted reflectivity (20 dBZ; black contour) and LLW (10 m s^{-1}; green contour) and ensemble mean initial condition reflectivity (20 dBZ; gray contour) for forecast times (a) 1-hour, valid 2230 UTC (b) 1-hour with statistical significance test (c) 2-hour, valid 2330 UTC (d) 2-hour with statistical significance test.

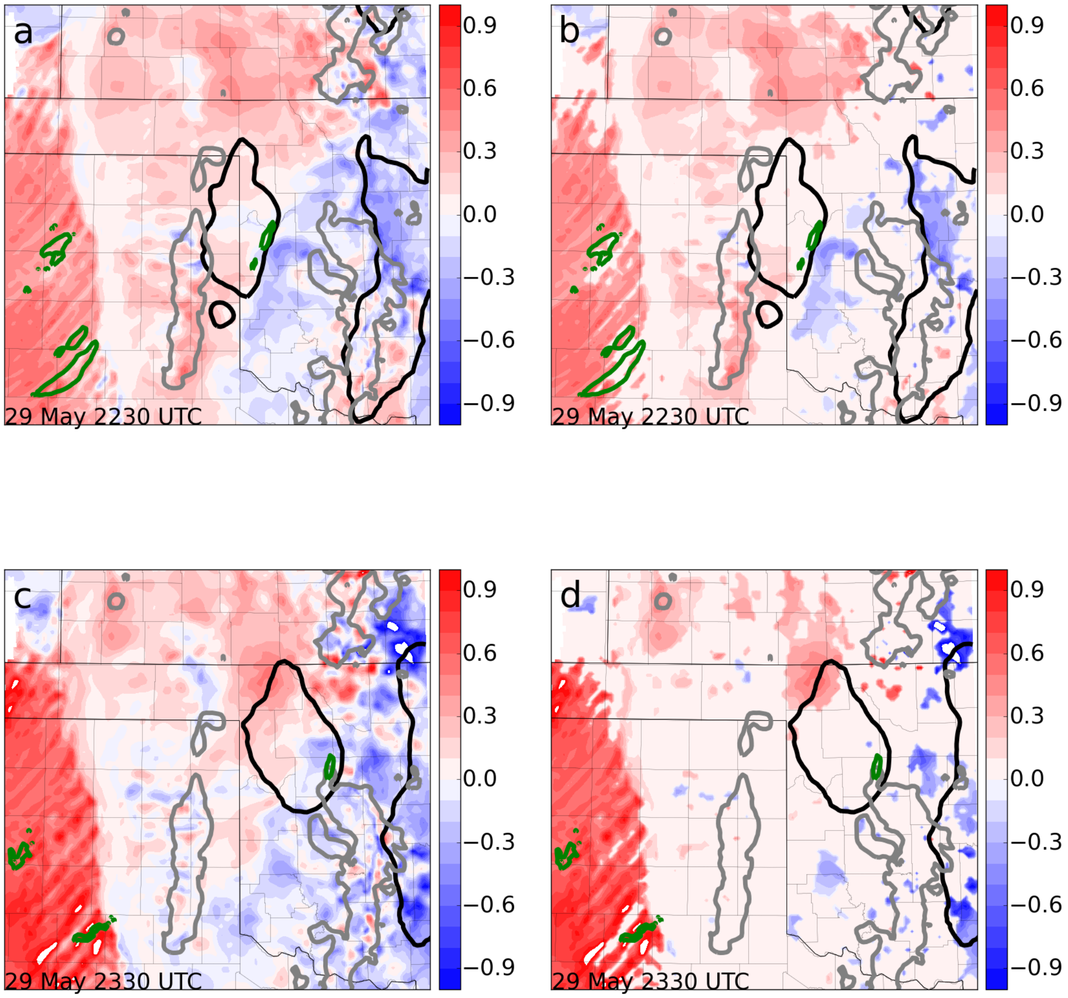

Figure 5.7. 29 May target storm averaged LLW (> 10 m s^{-1}) sensitivity to initial condition 850 hPa temperature in m s^{-1} (^{o}C)$^{-1}$ and ensemble mean forecasted reflectivity (20 dBZ; black contour) and ensemble mean initial condition reflectivity (20 dBZ; gray contour) and LLW (10 m s^{-1}; green contour) for forecast times (a) 1-hour, valid 2230 UTC (b) 1-hour with statistical significance test (c) 2-hour, valid 2330 UTC (d) 2-hour with statistical significance test.

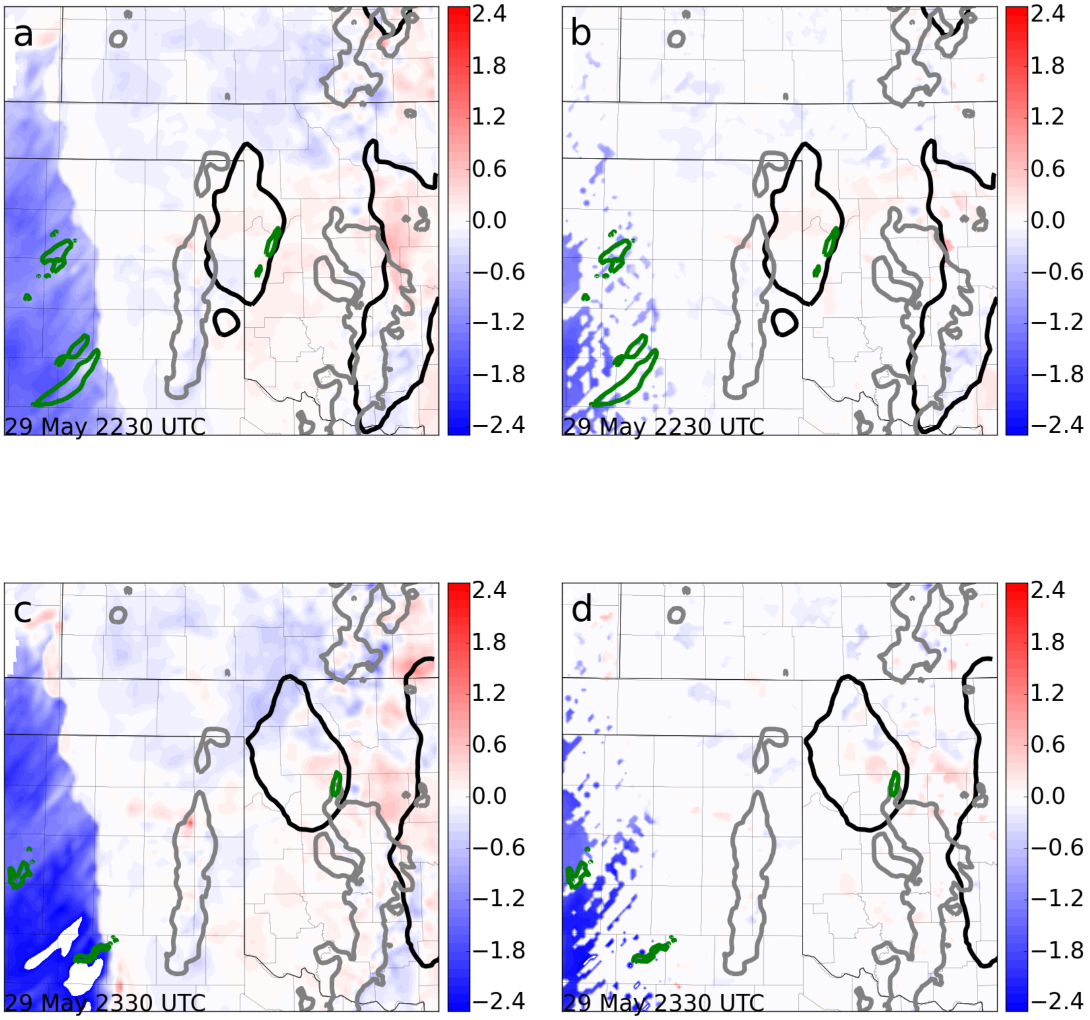

Figure 5.8. 29 May target storm averaged LLW (> 10 m s^{-1}) sensitivity to initial condition 850 hPa water vapor mixing ratio in m s^{-1} (g kg^{-1})$^{-1}$ and ensemble mean forecasted reflectivity (20 dBZ; black contour) and LLW (10 m s^{-1}; green contour) and ensemble mean initial condition reflectivity (20 dBZ; gray contour) for forecast times (a) 1-hour, valid 2230 UTC (b) 1-hour with statistical significance test (c) 2-hour, valid 2330 UTC (d) 2-hour with statistical significance test.

5.2 30 May non-tornadic supercell results

ESA is applied to the non-tornadic supercell in central Oklahoma on 30 May. For this case, 30 and 60 minute forecasts are initialized at 1900 UTC. Storm-averaged composite reflectivity is sensitive to low-level moisture (850 hPa; Fig. 5.9). Reflectivity is positively sensitive to this moisture within the inflow region to the east and southeast of the storm, most notably for a 30 minute forecast. Values are approximately 1 dBZ (g $kg^{-1})^{-1}$ in most locations but exceed 3 dBZ (g $kg^{-1})^{-1}$ to the southeast of the storm for a 30 minute forecast (Fig. 5.9a,b). The results from ESA for reflectivity forecasts to mid-level moisture (700 hPa) are less conclusive (Fig. 5.10). For a one hour forecast, negative sensitivity to moisture appears to the southeast while positive sensitivity is seen in a 30 minute forecast in this same region with the sensitivities elongated in the downwind direction. Surprisingly, reflectivity is not strongly sensitive to CAPE (Fig. 5.11). This may imply the relationship between CAPE and reflectivity is highly nonlinear, such that ESA, constrained by the linear assumption, fails to capture any meaningful relationship (not shown).

Since one characteristic of a supercell is a persistent, rotating updraft, ESA is applied to 2-5 km UH. For this particular supercell, UH values are quite small as some ensemble members only have a maximum UH of 5-10 m^2s^{-2}. Forecast UH is found to be very dependent on initial condition 0-6 km wind shear (hereafter SHR06; Fig. 5.12). Positive sensitivity spans the storm inflow environment to the south and southeast of the storm for both 30 and 60 minute forecasts where values exceed 7 m^2s^{-2} (m $s^{-1})^{-1}$. This suggests larger SHR06 values within the inflow region will yield large average UH for this supercell. UH is also positively sensitive to 850 hPa wind speed, particularly within the inflow region for a 60 minute forecast (Fig. 5.13). In this 60 minute forecast, sensitivity magnitudes exceed 5 m^2s^{-2} $(m\ s^{-1})^{-1}$ within the inflow region. This translates to stronger storm-relative inflow inducing larger UH. UH is also positively sensitive to 850 hPa temperature within the inflow region (Fig. 5.14). Sensitivity values are significantly larger where they exceed 20 m^2s^{-2} $(^oC)^{-1}$. In summary, UH will increase if low-level inflow winds are faster, air is warmer, and 0-6 km shear is greater.

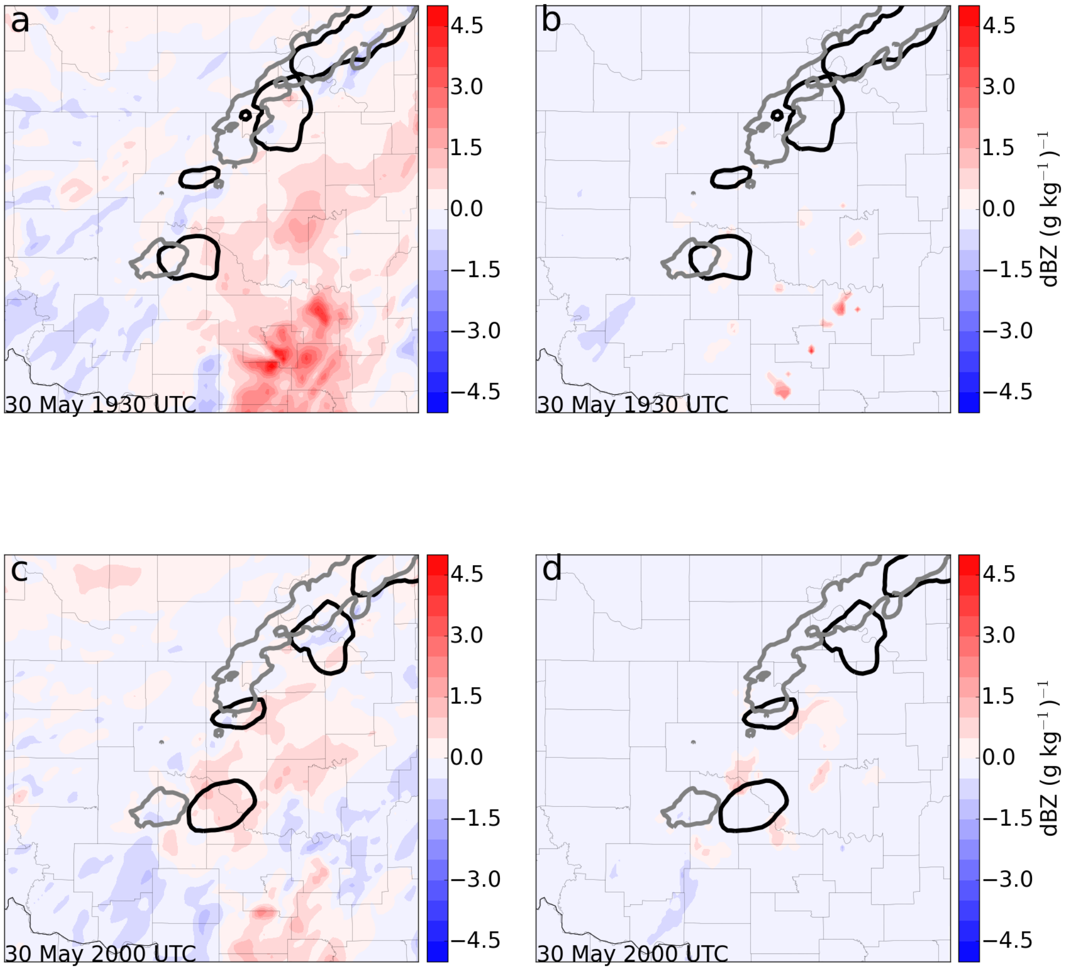

Figure 5.9. 30 May target storm averaged composite reflectivity (> 20 dBZ) sensitivity to initial condition 850 hPa water vapor mixing ratio in dBZ (g kg^{-1})$^{-1}$ and ensemble mean forecasted reflectivity (20 dBZ; black contour) and ensemble mean initial condition reflectivity (20 dBZ; gray contour) for forecast times (a) 30 minutes, valid 1930 UTC (b) 30 minutes with statistical significance test (c) 1-hour, valid 2000 UTC (d) 1-hour with statistical significance test.

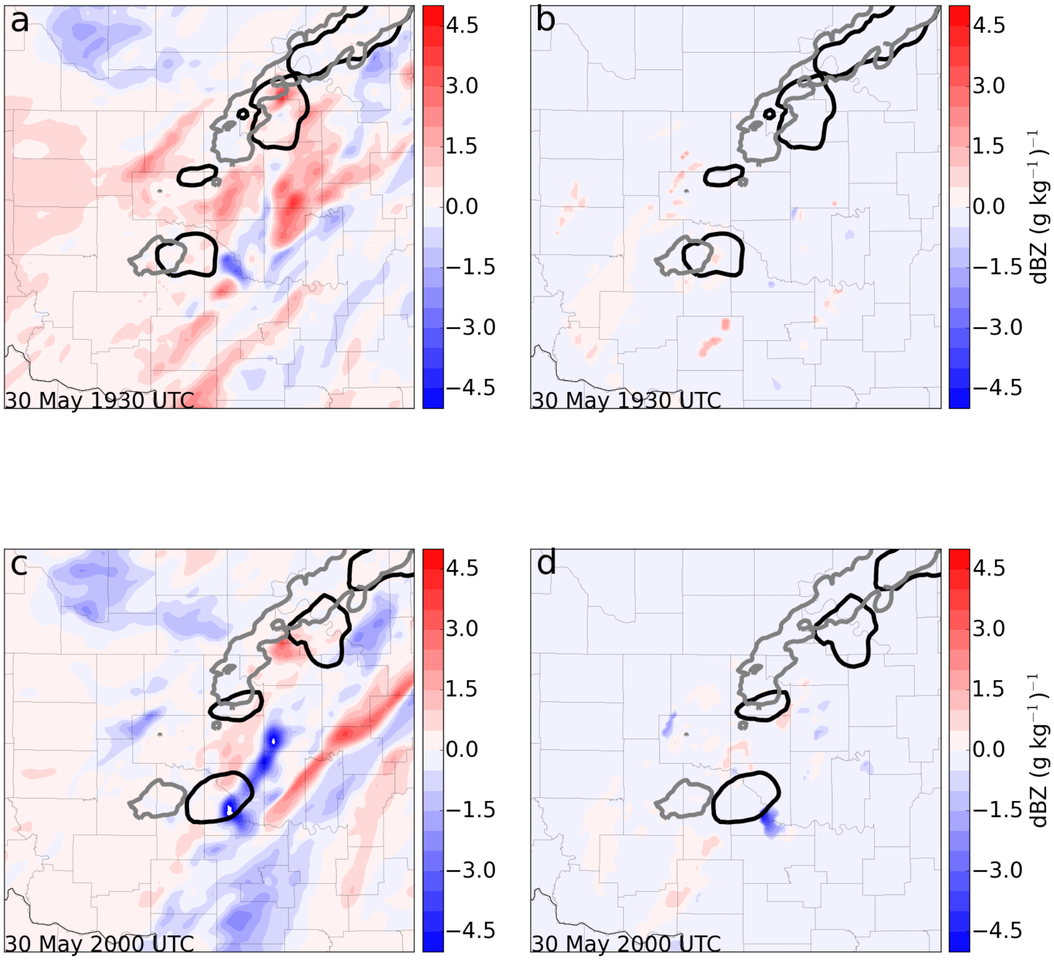

Figure 5.10. 30 May target storm averaged composite reflectivity (> 20 dBZ) sensitivity to initial condition 700 hPa water vapor mixing ratio in dBZ (g kg^{-1})$^{-1}$ and ensemble mean forecasted reflectivity (20 dBZ; black contour) and ensemble mean initial condition reflectivity (20 dBZ; gray contour) for forecast times (a) 30 minutes, valid 1930 UTC (b) 30 minutes with statistical significance test (c) 1-hour, valid 2000 UTC (d) 1-hour with statistical significance test.

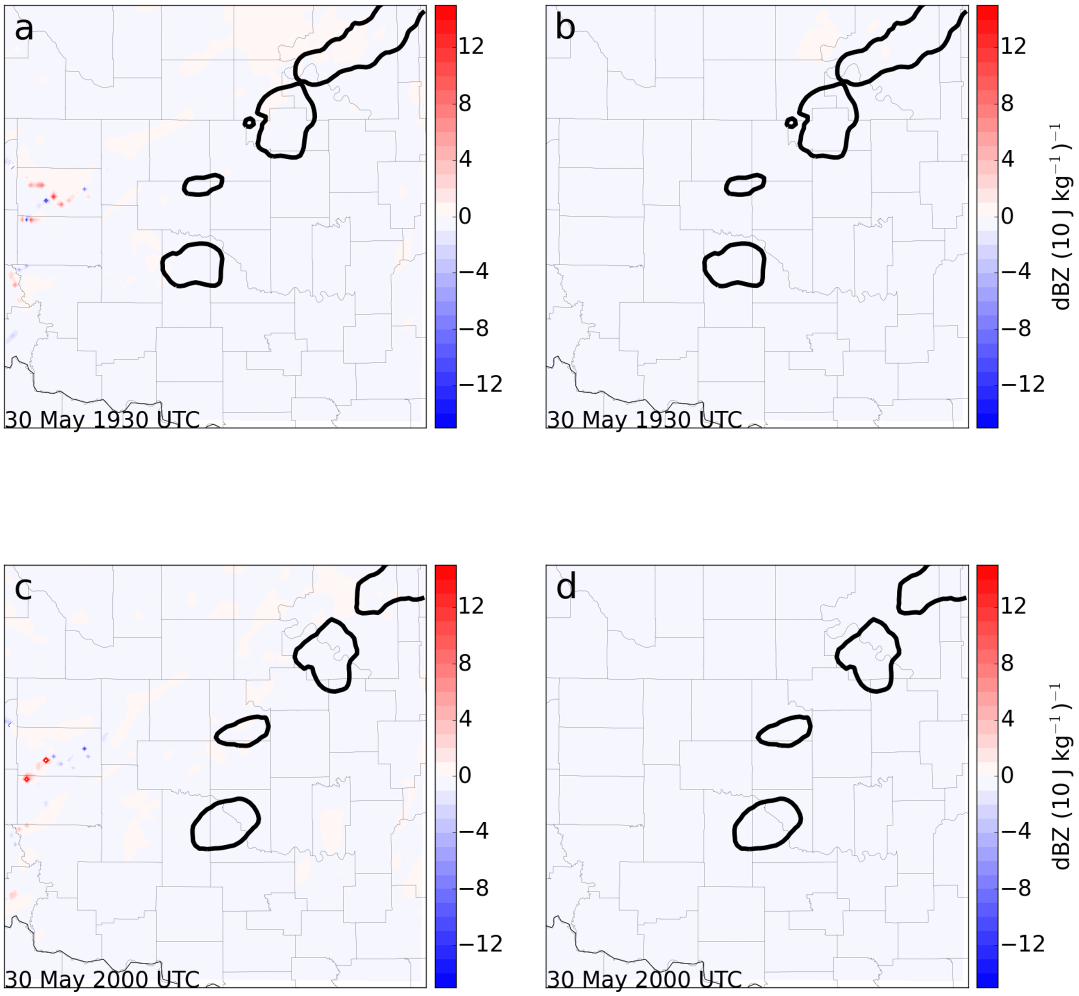

Figure 5.11. 30 May target storm averaged composite reflectivity (> 20 dBZ) sensitivity to initial condition CAPE in dBZ (10 J kg^{-1})$^{-1}$ and ensemble mean forecasted reflectivity (20 dBZ; black contour) for forecast times (a) 30 minutes, valid 1930 UTC (b) 30 minutes with statistical significance test (c) 1-hour, valid 2000 UTC (d) 1-hour with statistical significance test.

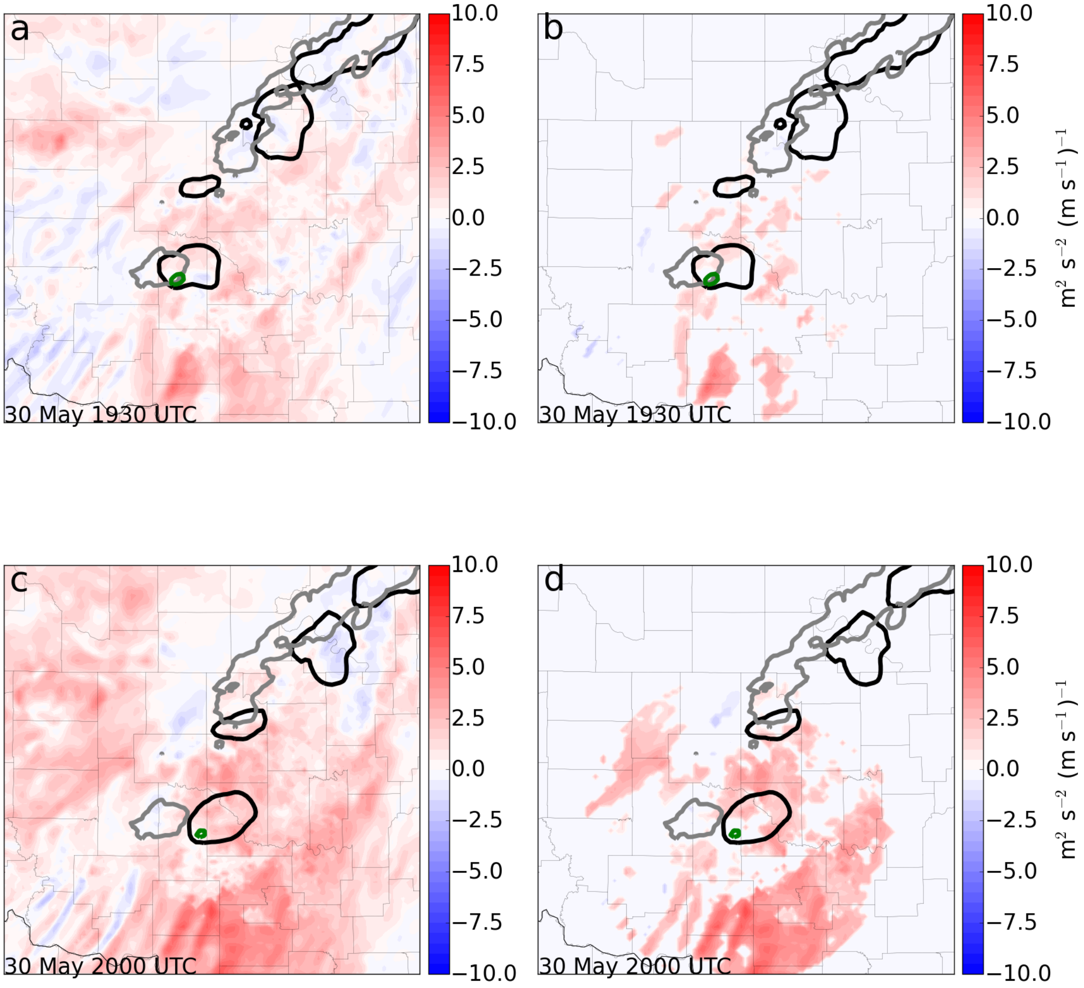

Figure 5.11. 30 May target storm averaged 2-5 km UH (> 5 m^2s^{-2}) sensitivity to initial condition SHR06 in m^2s^{-2} $(m\ s^{-1})^{-1}$ and ensemble mean forecasted reflectivity (20 dBZ; black contour) and 2-5 km UH (5 m^2s^{-2}; green contour) and ensemble mean initial condition reflectivity (20 dBZ; gray contour) for forecast times (a) 30 minutes, valid 1930 UTC (b) 30 minutes with statistical significance test (c) 1-hour, valid 2000 UTC (d) 1-hour with statistical significance test.

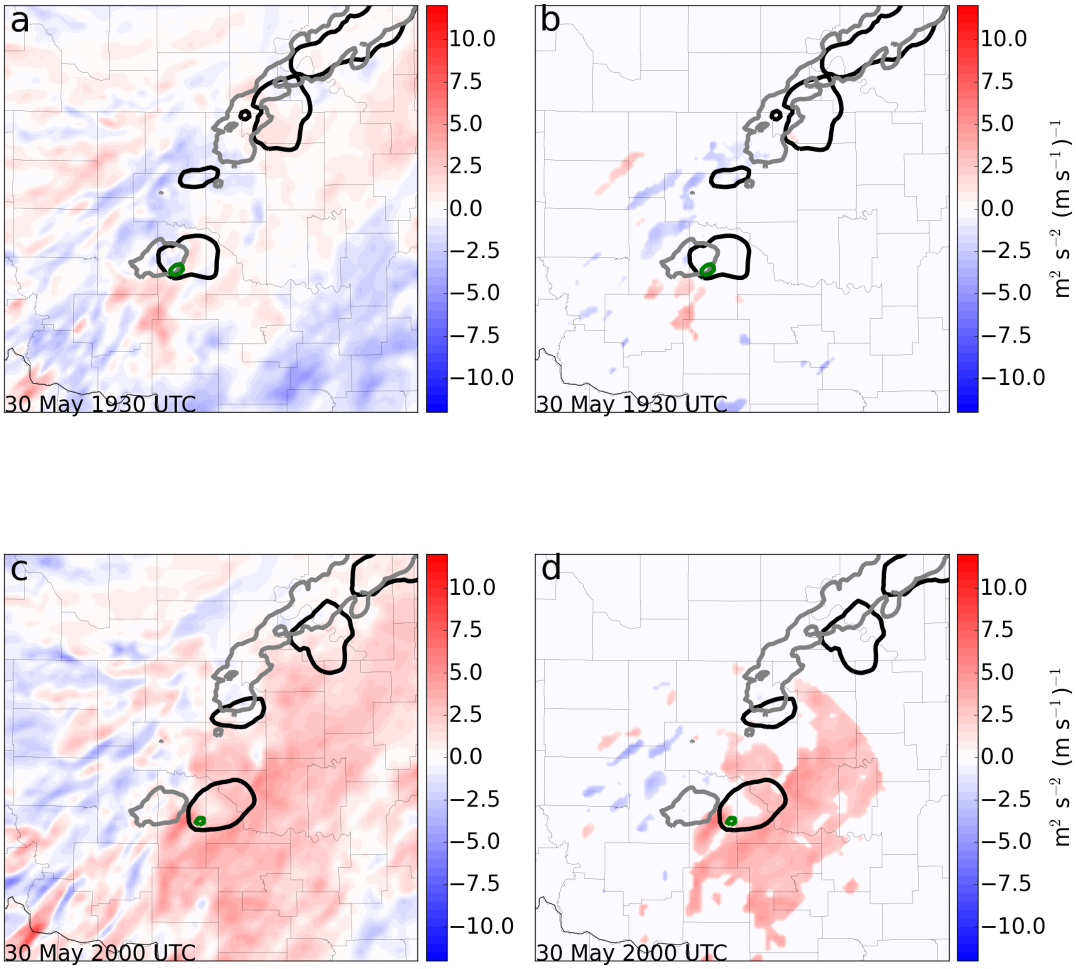

Figure 5.13. 30 May target storm averaged 2-5 km UH (> 5 m^2s^{-2}) sensitivity to initial condition 850 hPa wind speed in m^2s^{-2} ($m s^{-1}$)$^{-1}$ and ensemble mean forecasted reflectivity (20 dBZ; black contour) and 2-5 km UH (5 m^2s^{-2}; green contour) and ensemble mean initial condition reflectivity (20 dBZ; gray contour) and ensemble mean initial condition reflectivity (20 dBZ; gray contour) for forecast times (a) 30 minutes, valid 1930 UTC (b) 30 minutes with statistical significance test (c) 1-hour, valid 2000 UTC (d) 1-hour with statistical significance test.

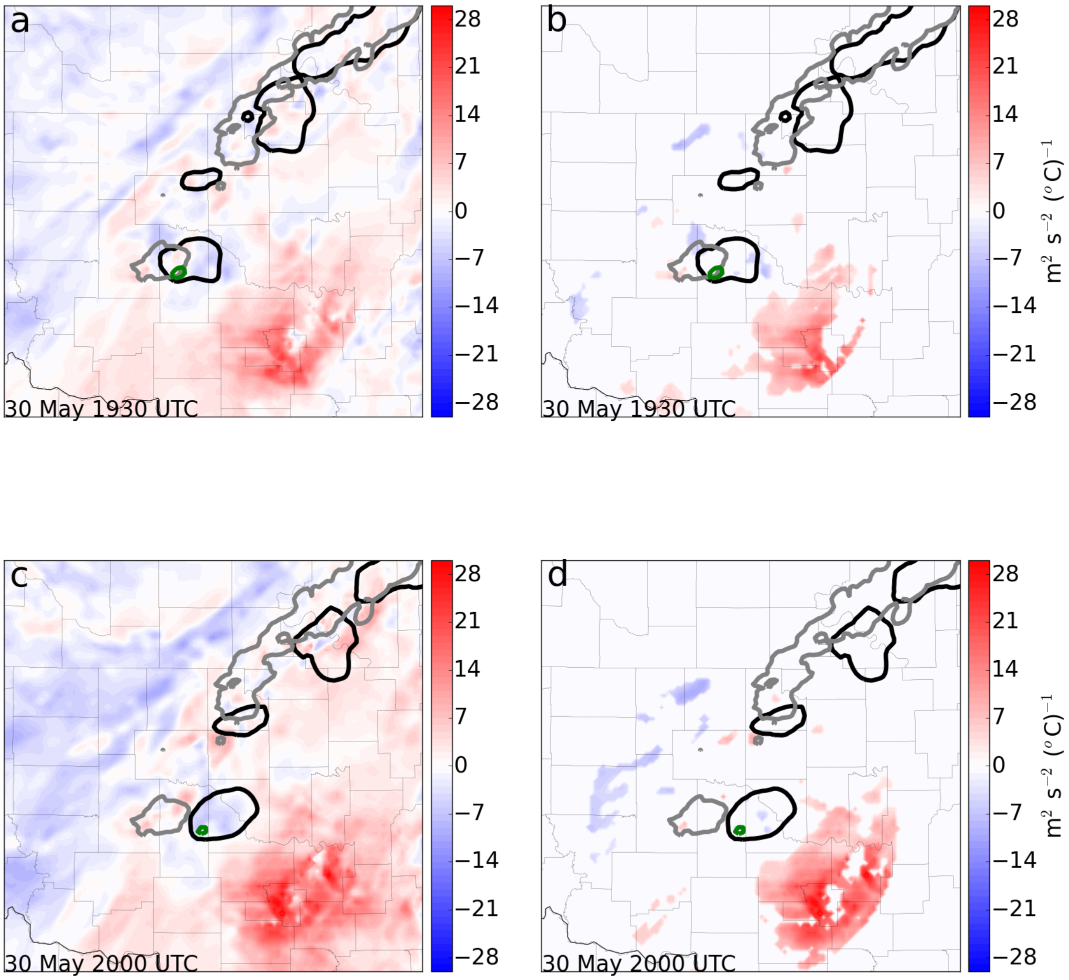

Figure 5.14. 30 May target storm averaged 2-5 km UH (> 5 m^2s^{-2}) sensitivity to initial condition 850 hPa temperature in m^2s^{-2} (^oC)$^{-1}$ and ensemble mean forecasted reflectivity (20 dBZ; black contour) and 2-5 km UH (5 m^2s^{-2}; green contour) and ensemble mean initial condition reflectivity (20 dBZ; gray contour) for forecast times (a) 30 minutes, valid 1930 UTC (b) 30 minutes with statistical significance test (c) 1-hour, valid 2000 UTC (d) 1-hour with statistical significance test.

5.2 31 May tornadic supercell results

As in the 30 May case, positive sensitivity of forecast reflectivity to 850 hPa water vapor mixing ratio is prevalent within the inflow region to the southeast of the supercell in 30, 60, and 90 minute forecasts (Fig. 5.15). Negative sensitivities exist to the west behind the dryline. This result is similar to the 29 May case where drier air behind the dryline is associated with higher average reflectivity. The pattern of reflectivity sensitivity to mid-level moisture (700 hPa mixing ratio) is similar to that of low-level moisture with positive sensitivity to the east and southeast (Fig. 5.16), but the sensitivity magnitudes are much larger. This indicates that small changes in cloud layer moisture have a much larger impact on reflectivity than similar changes in low-level moisture. As on 30 May, reflectivity is not sensitive to CAPE using this method (Fig. 5.17). As previously stated, this may be a result of nonlinearity.

Since the 31 May event produced significant flash flooding, ESA is applied to forecast accumulated rainfall. This reveals positive sensitivity to both low-level (Fig. 5.18) and mid-level (Fig. 5.19) water vapor mixing ratio within the storm's inflow region, again with cloud layer moisture having a larger influence. Ingested water vapor originates from the moist airmass to the east and directly impacts rainfall. For low-level moisture, these sensitivity values approach 2 mm $(g\ kg^{-1})^{-1}$. In the mid-levels, magnitudes are greater (exceeding 4 mm $(g\ kg^{-1})^{-1}$) suggesting mid-level moisture is an important environmental feature to rainfall accumulation. There are negative sensitivities to the southwest within the dry airmass, particularly in the low-levels. Overall, these results are similar to reflectivity sensitivities, which is to be expected.

ESA is also applied to 2-5 km UH beginning with SHR06 (Fig. 5.20). Sizable positive sensitivity exists within the near inflow region for 30 and 60 minute forecasts (Fig 5.20a,c), and these sensitivities are statistically significant (Fig. 5.20b,d). The sensitivity magnitudes decrease for a 90 minute forecast. These results are similar to the 30 May case given positive sensitivity in the inflow region. UH is also positively sensitive to 850 hPa inflow winds for the 30 and 60 minute forecasts (Fig. 5.21). This agrees with the results of the previous day since stronger inflow will result in larger UH. Sensitivity to low-level temperature, however, is not similar to that seen on the previous day (Fig. 5.22). For these forecasts, UH is negatively sensitive to 850 hPa temperature within the inflow region. This result is somewhat unexpected and appears counterintuitive. Model soundings to the south of the storm indicate that a more stable layer has developed and that cooling at 850 hPa would reduce convection inhibition. Sobash et al. (2016) show through verification that 2-5 km UH is a poor surrogate for tornado prediction since it is a measure of mid-level updraft rotation while low-level rotation provides more insight into tornado probabilities. Thus, 0-1 km UH also is chosen as the forecast metric. The sensitivity of 0-1 km UH to 0-1 km wind shear (hereafter SHR01) indicates that 0-1 km UH is directly proportional to SHR01 in a 30 minute forecast with values exceeding 1 m^2s^{-2} $(m\ s^{-1})^{-1}$ (Fig. 5.23). However, there is a sign change from a 30 minute to 1 hour forecast where positive sensitivities at 30 minutes within the inflow region become negative sensitivities at 1 hour. This occurs in other fields as well (e.g., 850 hPa wind speed in Fig. 5.21). To further explore this temporal change in sensitivities, a grid point to the south of the UH maximum was chosen since this is a location where the sensitivity sign changes and is denoted by a black dot in Fig. 5.23. Scatter plots of initial condition SHR01 and forecasted 0-1 km UH reveal the linear regressions for both a 30 and 60 minute forecast (Fig. 5.24). It is apparent that sampling error is the cause of this sign change as a few outliers skew the regression slope from positive (30 minute forecast) to negative (60 minute forecast). This is an example of how ESA can fail due to sampling error, particularly on the convective scale. Other sensitivity scatterplots reveal relationships between environmental initial conditions and forecast metrics (Fig. 5.25).

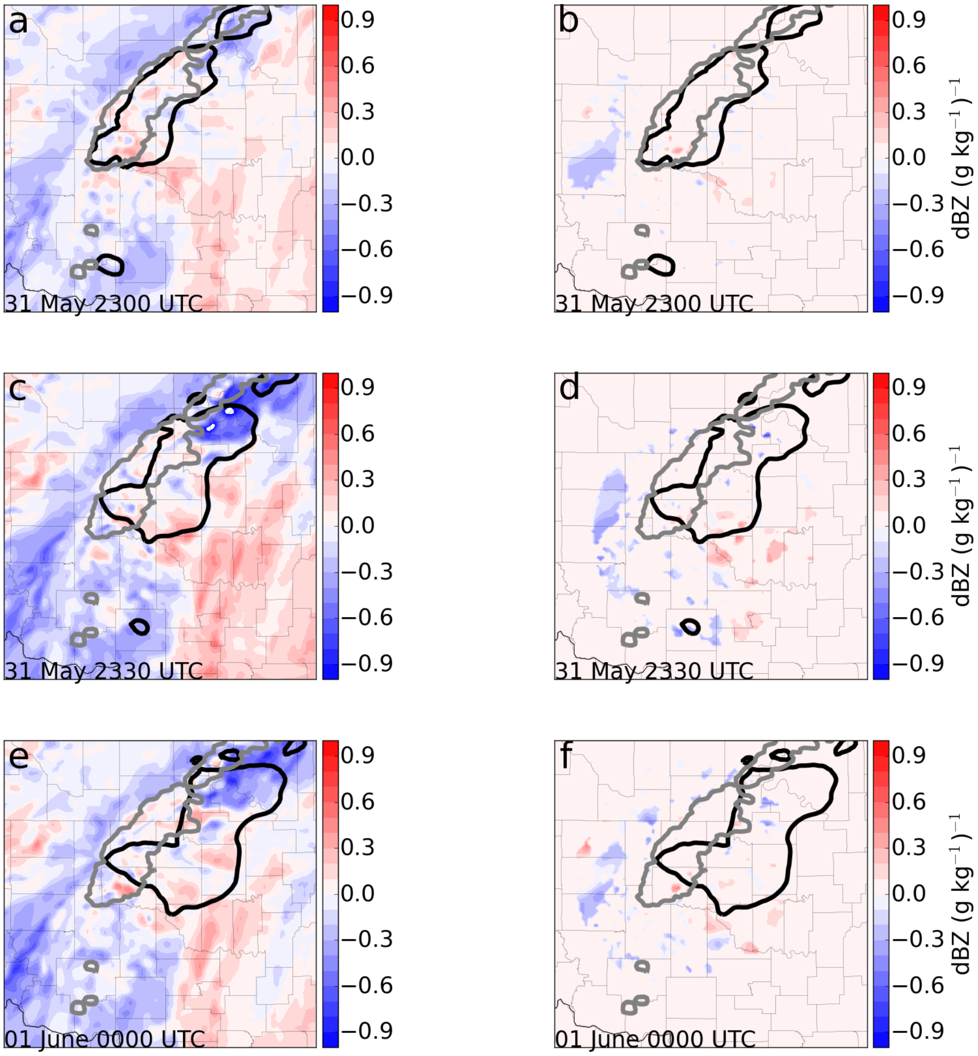

Figure 5.15. 31 May target storm averaged composite reflectivity (> 20 dBZ) sensitivity to initial condition 850 hPa water vapor mixing ratio in dBZ (g kg^{-1})$^{-1}$ and ensemble mean forecasted reflectivity (20 dBZ; black contour) and ensemble mean initial condition reflectivity (20 dBZ; gray contour) for forecast times (a) 30 minutes, valid 2300 UTC (b) 30 minutes with statistical significance test (c) 1-hour, valid 2330 UTC (d) 1-hour with statistical significance test (e) 90 minutes, valid 0000 UTC, 01 June (f) 90 minutes with statistical significance test.

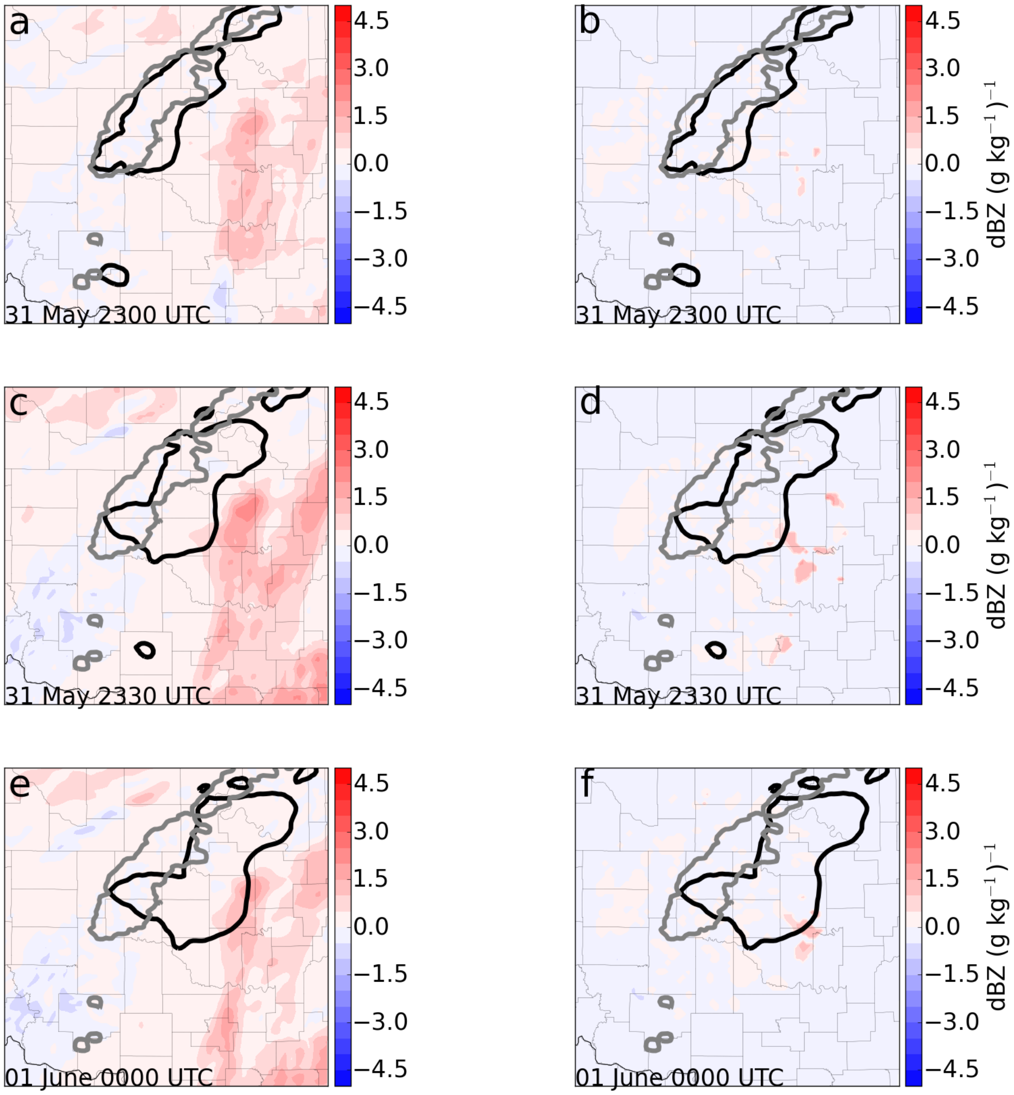

Figure 5.16. 31 May target storm averaged composite reflectivity (> 20 dBZ) sensitivity to initial condition 700 hPa water vapor mixing ratio in dBZ (g kg^{-1})$^{-1}$ and ensemble mean forecasted reflectivity (20 dBZ; black contour) and ensemble mean initial condition reflectivity (20 dBZ; gray contour) for forecast times (a) 30 minutes, valid 2300 UTC (b) 30 minutes with statistical significance test (c) 1-hour, valid 2330 UTC (d) 1-hour with statistical significance test (e) 90 minutes, valid 0000 UTC, 01 June (f) 90 minutes with statistical significance test.

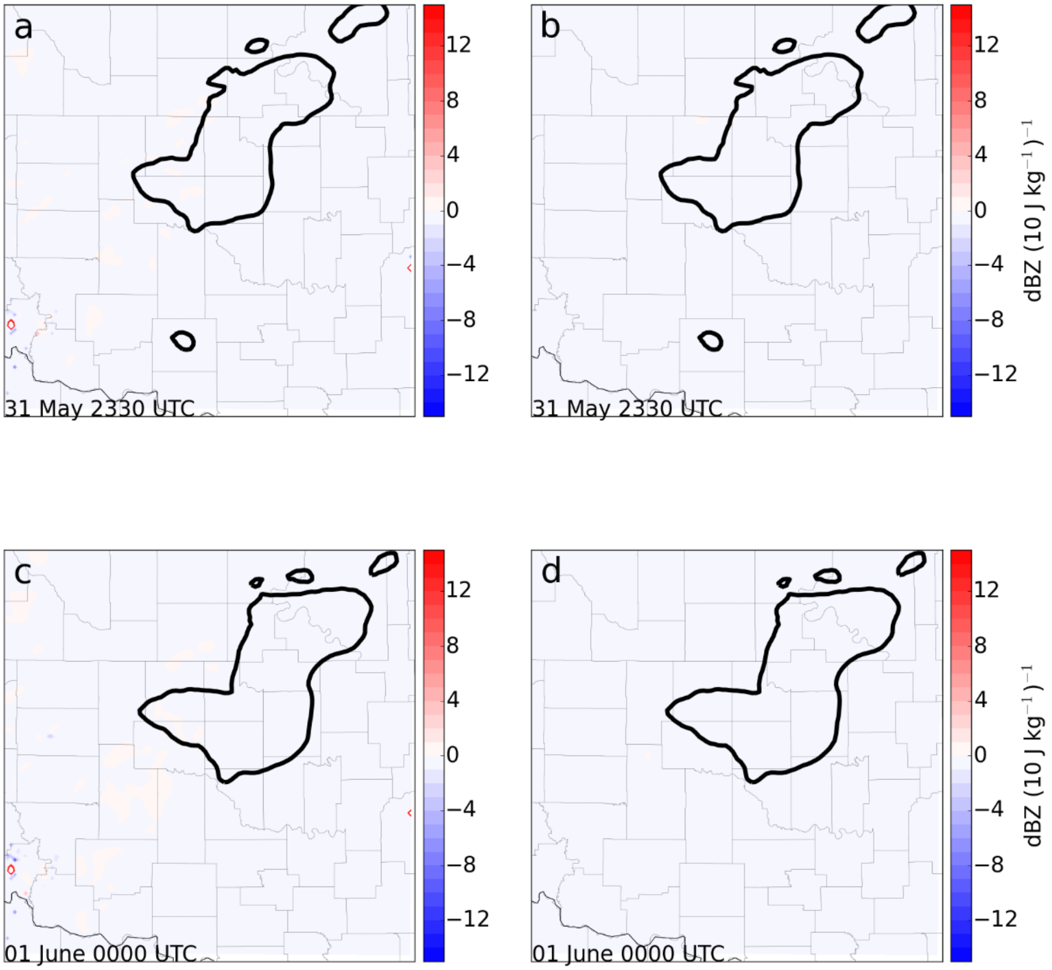

Figure 5.17. 31 May target storm averaged composite reflectivity (> 20 dBZ) sensitivity to initial condition CAPE in dBZ (10 J kg^{-1})$^{-1}$ and ensemble mean forecasted reflectivity (20 dBZ; black contour) for forecast times (a) 1-hour, valid 2330 UTC (b) 1-hr with statistical significance test (c) 90 minutes, valid 0000 UTC, 01 June (d) 90 minutes with statistical significance test.

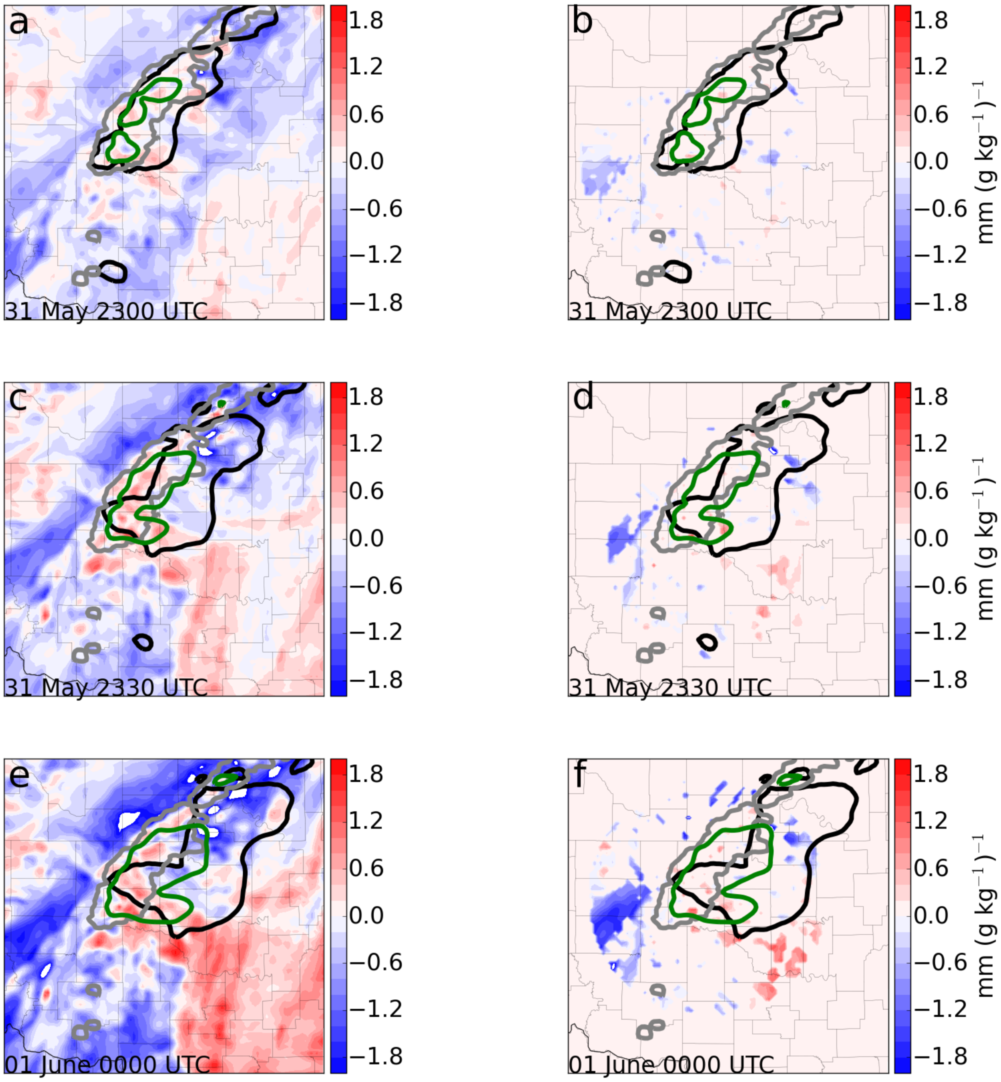

Figure 5.18. 31 May target storm averaged accumulated rainfall (> 10 mm) sensitivity to initial condition 850 hPa water vapor mixing ratio in mm (g kg^{-1})$^{-1}$ and ensemble mean forecasted reflectivity (20 dBZ; black contour) and accumulated rainfall (10 mm; green contour) and ensemble mean initial condition reflectivity (20 dBZ; gray contour) for forecast times (a) 30 minutes, valid 2300 UTC (b) 30 minutes with statistical significance test (c) 1-hour, valid 2330 UTC (d) 1-hour with statistical significance test (e) 90 minutes, valid 0000 UTC, 01 June (f) 90 minutes with statistical significance test.

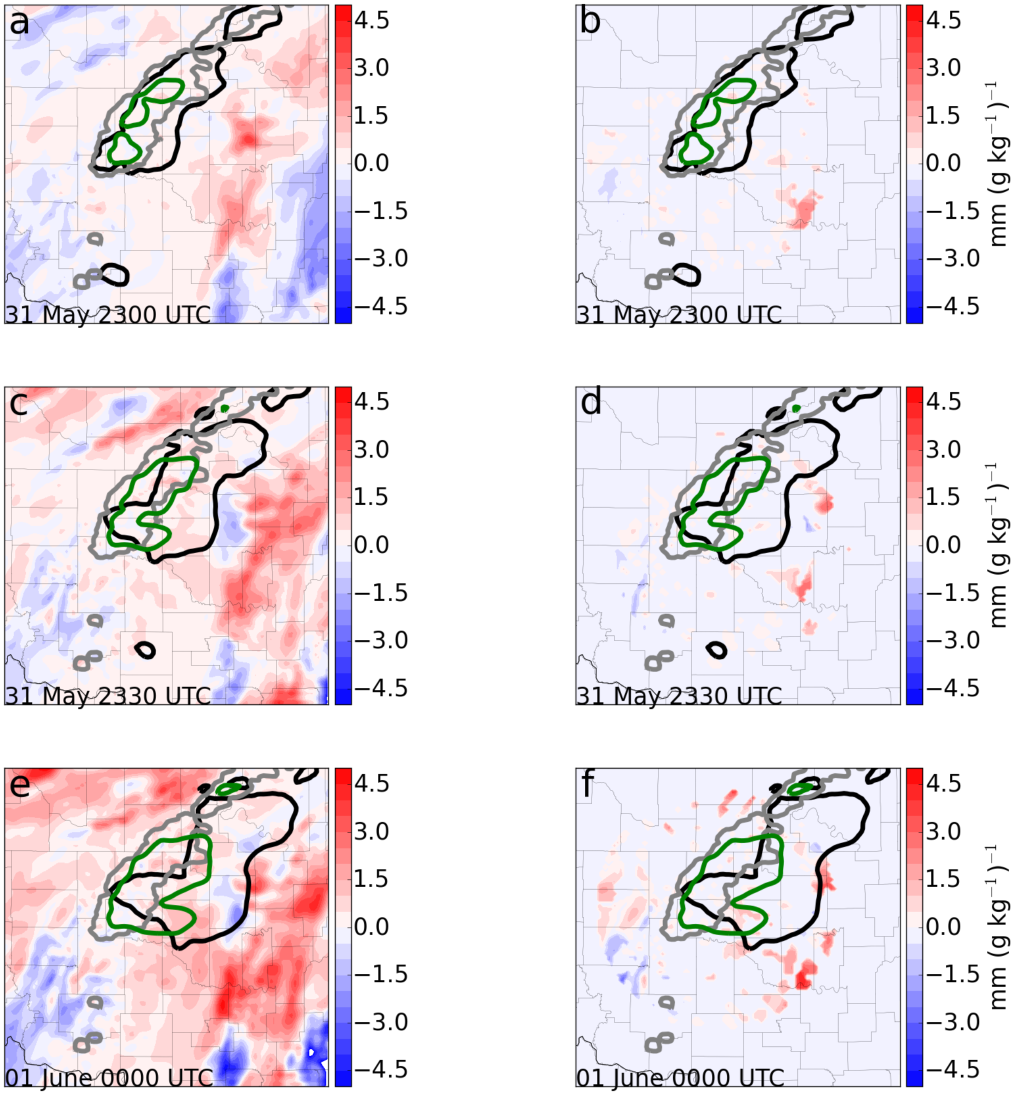

Figure 5.19. 31 May target storm averaged accumulated rainfall (> 10 mm) sensitivity to initial condition 700 hPa water vapor mixing ratio in mm (g kg^{-1})$^{-1}$ and ensemble mean forecasted reflectivity (20 dBZ; black contour) and accumulated rainfall (10 mm; green contour) and ensemble mean initial condition reflectivity (20 dBZ; gray contour) for forecast times (a) 30 minutes, valid 2300 UTC (b) 30 minutes with statistical significance test (c) 1-hour, valid 2330 UTC (d) 1-hour with statistical significance test (e) 90 minutes, valid 0000 UTC, 01 June (f) 90 minutes with statistical significance test.

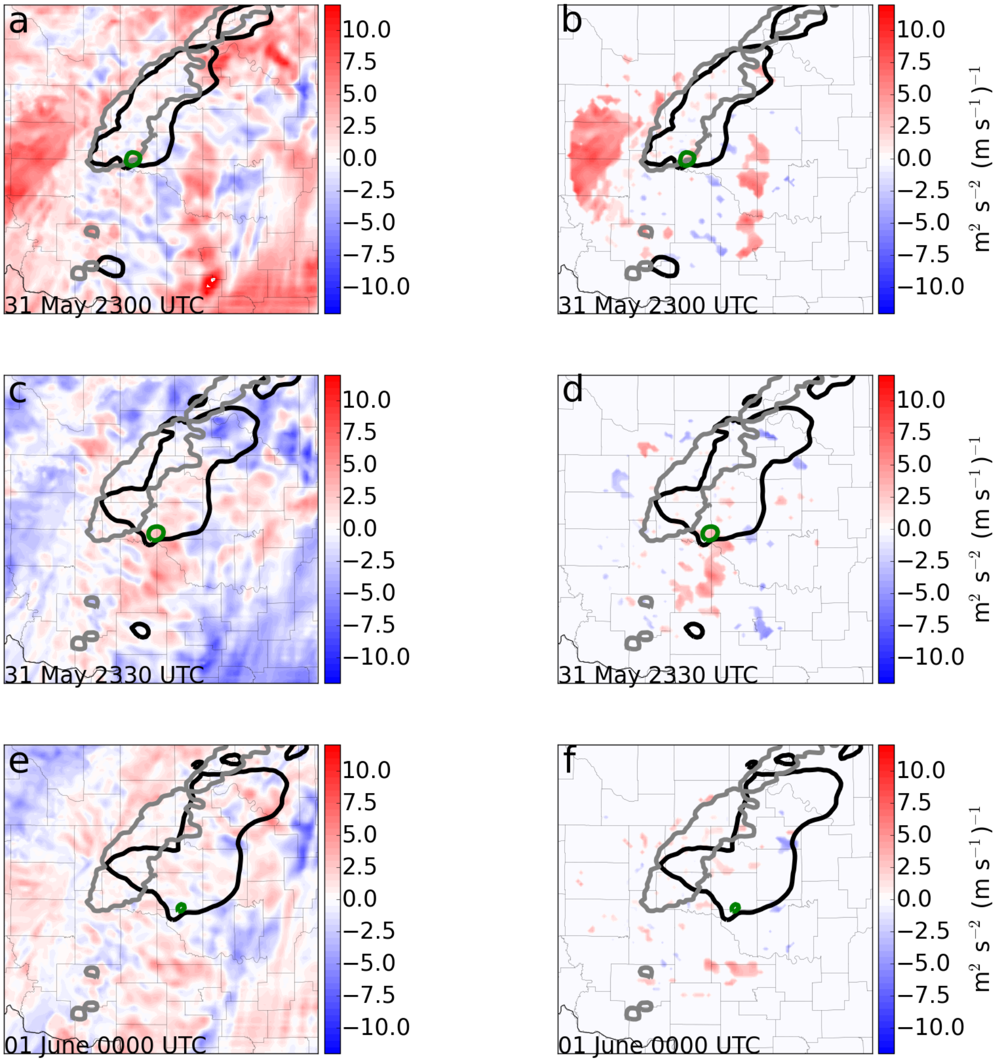

Figure 5.20. 31 May target storm averaged 2-5 km UH (> 75 m^2s^{-2}) sensitivity to initial condition SHR06 in m^2s^{-2} $(m\ s^{-1})^{-1}$ and ensemble mean forecasted reflectivity (20 dBZ; black contour) and 2-5 km UH (75 m^2s^{-2}; green contour) and ensemble mean initial condition reflectivity (20 dBZ; gray contour) for forecast times (a) 30 minutes, valid 2300 UTC (b) 30 minutes with statistical significance test (c) 1-hour, valid 2330 UTC (d) 1-hour with statistical significance test (e) 90 minutes, valid 0000 UTC, 01 June (f) 90 minutes with statistical significance test.

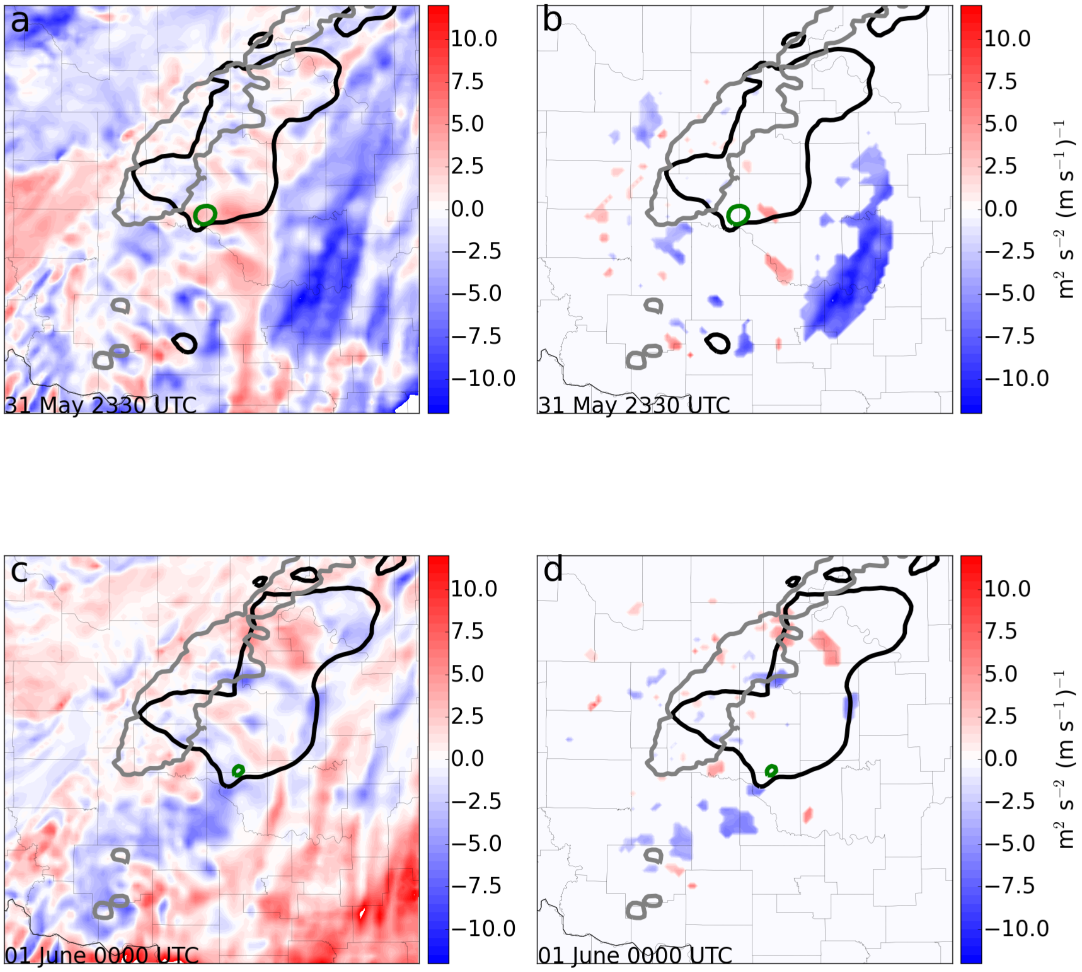

Figure 5.21. 31 May target storm averaged 2-5 km UH (> 75 m^2s^{-2}) sensitivity to initial condition 850 hPa wind speed in m^2s^{-2} (m s^{-1})$^{-1}$ and ensemble mean forecasted reflectivity (20 dBZ; black contour) and 2-5 km UH (75 m^2s^{-2}; green contour) and ensemble mean initial condition reflectivity (20 dBZ; gray contour) for forecast times (a) 1-hour, valid 2330 UTC (b) 1-hour with statistical significance test (c) 90 minutes, valid 0000 UTC, 01 June (d) 90 minutes with statistical significance test.

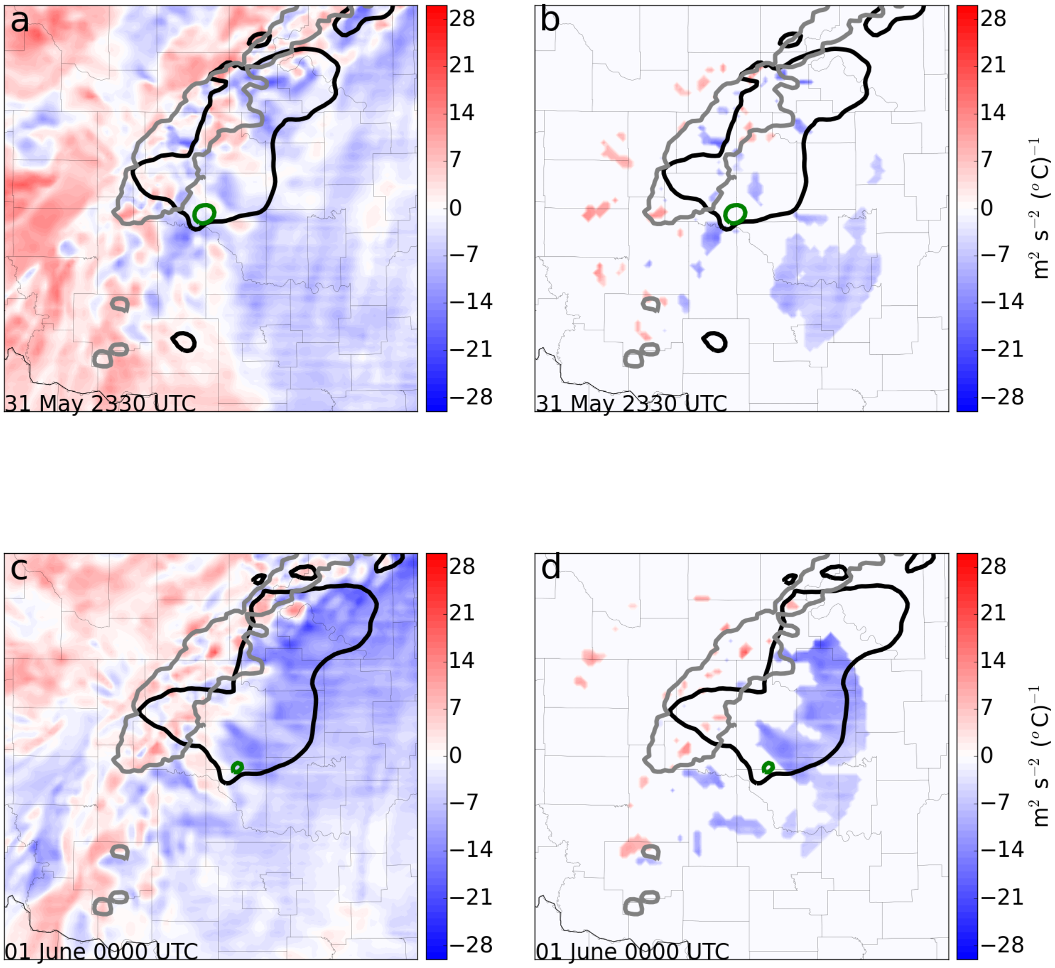

Figure 5.22. 31 May target storm averaged 2-5 km UH (> 75 m^2s^{-2}) sensitivity to initial condition 850 hPa temperature in m^2s^{-2} $(^oC)^{-1}$ and ensemble mean forecasted reflectivity (20 dBZ; black contour) and 2-5 km UH (75 m^2s^{-2}; green contour) and ensemble mean initial condition reflectivity (20 dBZ; gray contour) for forecast times (a) 1-hour, valid 2330 UTC (b) 1-hour with statistical significance test (c) 90 minutes, valid 0000 UTC, 01 June (d) 90 minutes with statistical significance test.

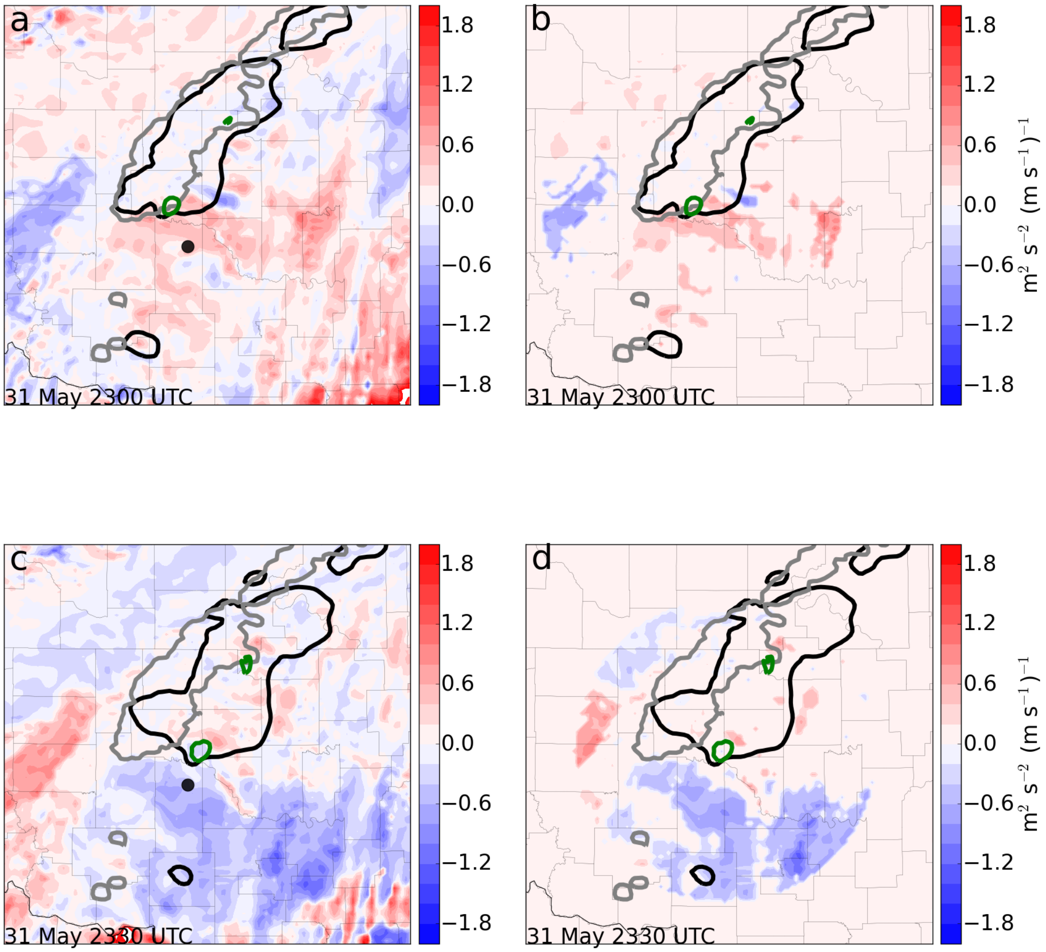

Figure 5.23. 31 May target storm averaged 0-1 km UH (> 5 m^2s^{-2}) sensitivity to initial condition SHR01 in m^2s^{-2} $(m\ s^{-1})^{-1}$ and ensemble mean forecasted reflectivity (20 dBZ; black contour) and 0-1 km UH (5 m^2s^{-2}; green contour) and ensemble mean initial condition reflectivity (20 dBZ; gray contour) for forecast times (a) 30 minutes, valid 2300 UTC (b) 30 minutes with statistical significance test (c) 1-hour, valid 2330 UTC (d) 1-hour with statistical significance test. The black dot in (a) and (c) is the grid point for Fig. 5.24.

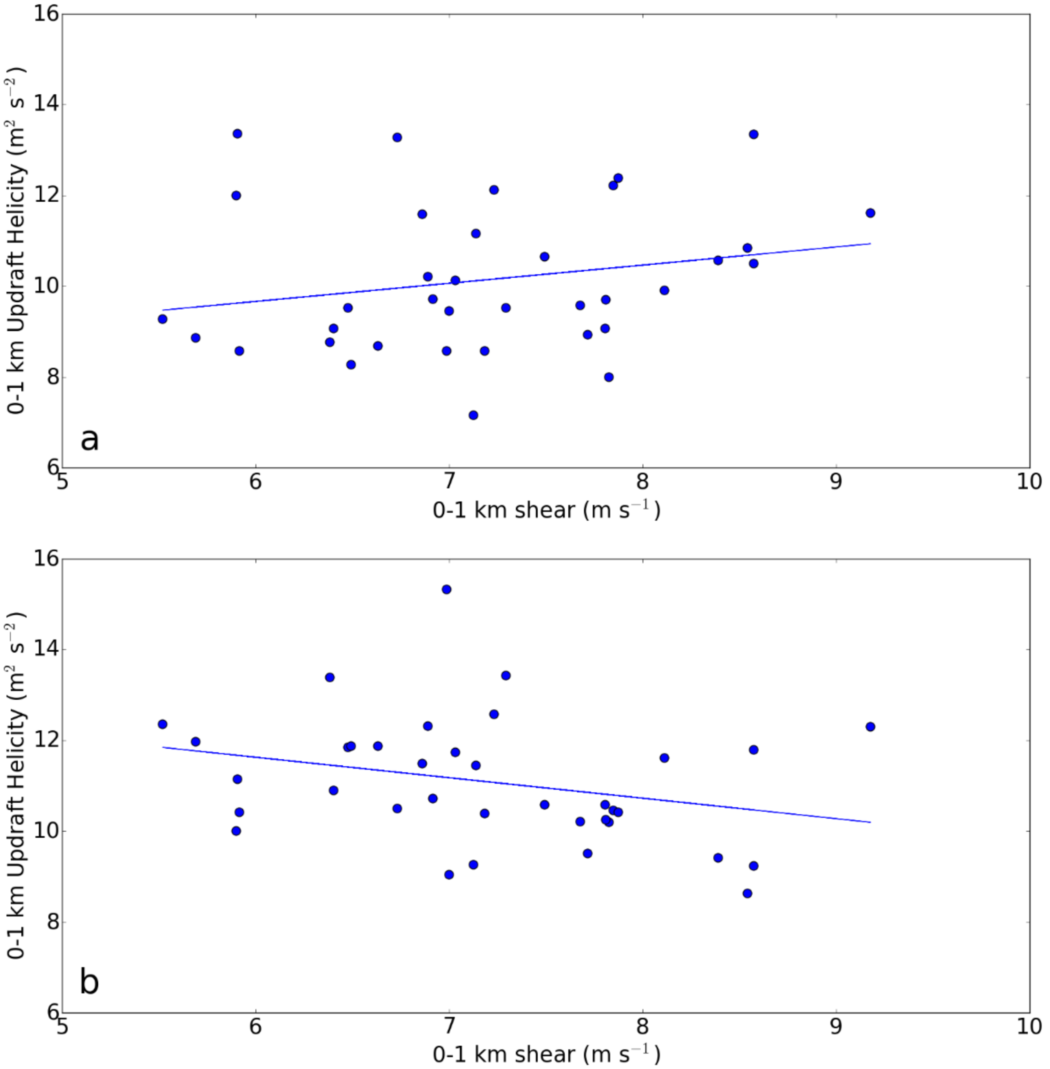

Figure 5.24. Scatter plots of initial condition SHR01 versus target storm forecasted average 0-1 UH (> 5 m^2s^{-2}) at black dot in Fig. 5.23 for forecast lead times (a) 30 minutes (b) 1-hour.

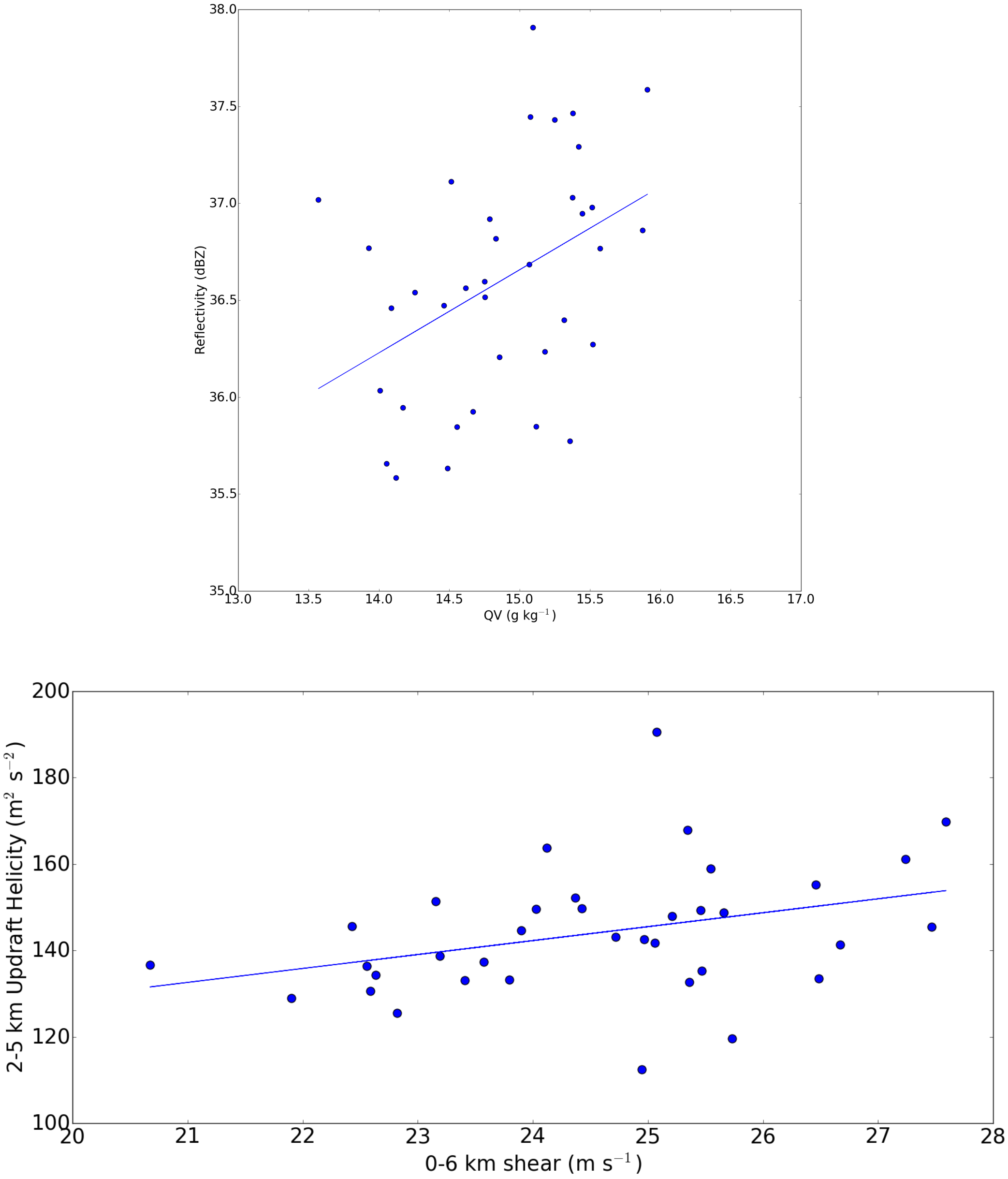

Figure 5.25. Example scatterplots of initial condition water vapor mixing ratio (g kg^{-1}) and one-hour forecast reflectivity (dBZ; top); initial condition 0-6 km shear and one-hour forecast 2-5 km UH (m^{2}s^{-2}; bottom).

5.4 Supercell evolution sensitivity to storm-induced shear perturbations

It is shown in Chapter 4 that vertical wind shear is enhanced within the inflow region of supercells. Since UH is positively sensitive to shear within the inflow region, these short-term impacts on the environment by convection could be important to convection evolution. ESA is once again applied to UH, however, the sensitivity variable is the *change* in wind shear over an hour time period attributed to the storm, and the forecast metrics are the 2-5 and 0-1 km UH (Fig. 5.26). Using this technique, positive (negative) sensitivities represent scenarios where short-term increases (decreases) in shear caused by the storm result in larger UH in the future.

Beginning with the 30 May case, 2-5 km UH is positively sensitive to the one hour storm-induced change in SHR06 (1800 – 1900 UTC) to the south and east of the supercell (Fig. 5.27). This suggests that the storm-induced increases in SHR06 have an effect on future convection evolution, meaning a positive feedback exists between the storm and environment. However, most of these sensitivities are not statistically significant (Fig. 5.27b,d,f).

The 31 May results are more robust than the previous day. The 2-5 km UH is positively sensitive to the one hour storm-induced change in SHR06 (2130 – 2230 UTC) for all three forecasts shown (Fig. 5.28). This inflow positive sensitivity is statistically significant in the 30 and 60 minute forecasts (Fig. 5.28b,d), supporting the idea of positive feedback between the storm and its nearby environment. This feedback is more prevalent on this day likely because the storm is larger and more intense and perturbs the environment to a greater extent than on 30 May (Chapter 4). A similar analysis is done for 0-1 km UH and storm-induced change in SHR01 (Fig. 29). Low-level rotation is positively sensitive to storm-induced SHR01 enhancements just to the south of the storm in the 30 minute forecast (Fig. 5.29a,b). Negative sensitivities are present for the 60 minute forecast (Fig. 5.29c,d), similarly to the negative sensitivities to the value of SHR01 (Fig. 5.23). Positive sensitivities return for the 90 minute forecast in close proximity to the UH region's forecast position (Fig. 5.29e,f).

The general finding suggested by these results is that UH magnitude and environmental wind shear are positively correlated. To briefly explore this relationship further, an idealized supercell simulation, initialized with a 3 K warm bubble, is created with an environmental sounding conducive to supercell development (Weisman and Klemp 1982). The domain has a 3 km grid spacing as does the inner domain for the real data cases. This simulation is rerun in two other instances where the SHR06 profile is enhanced. Using these three model simulations, 2-5 km UH is compared at various times during the model runs (Fig. 5.30). Initially, environments of higher shear yield larger average UH until an hour into the simulations. UH does not increase as largely in the 32 m s^{-1} case compared to the other two between 45 and 60 minutes. Varying shear magnitudes seems to affect the rotation cycling rates at later times since UH decreases at varying rates and times. Overall, these results support the notion that increased environmental wind shear will induce greater UH.

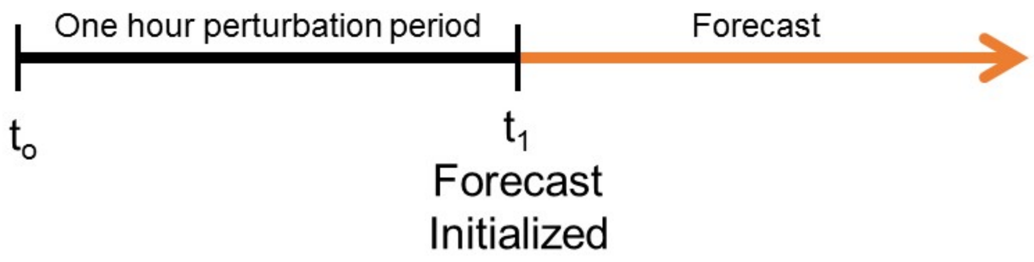

Figure 5.26. Schematic of storm-induced perturbation period followed by the forecast. In the 31 May case, the perturbation period spans 2130 – 2230 UTC.

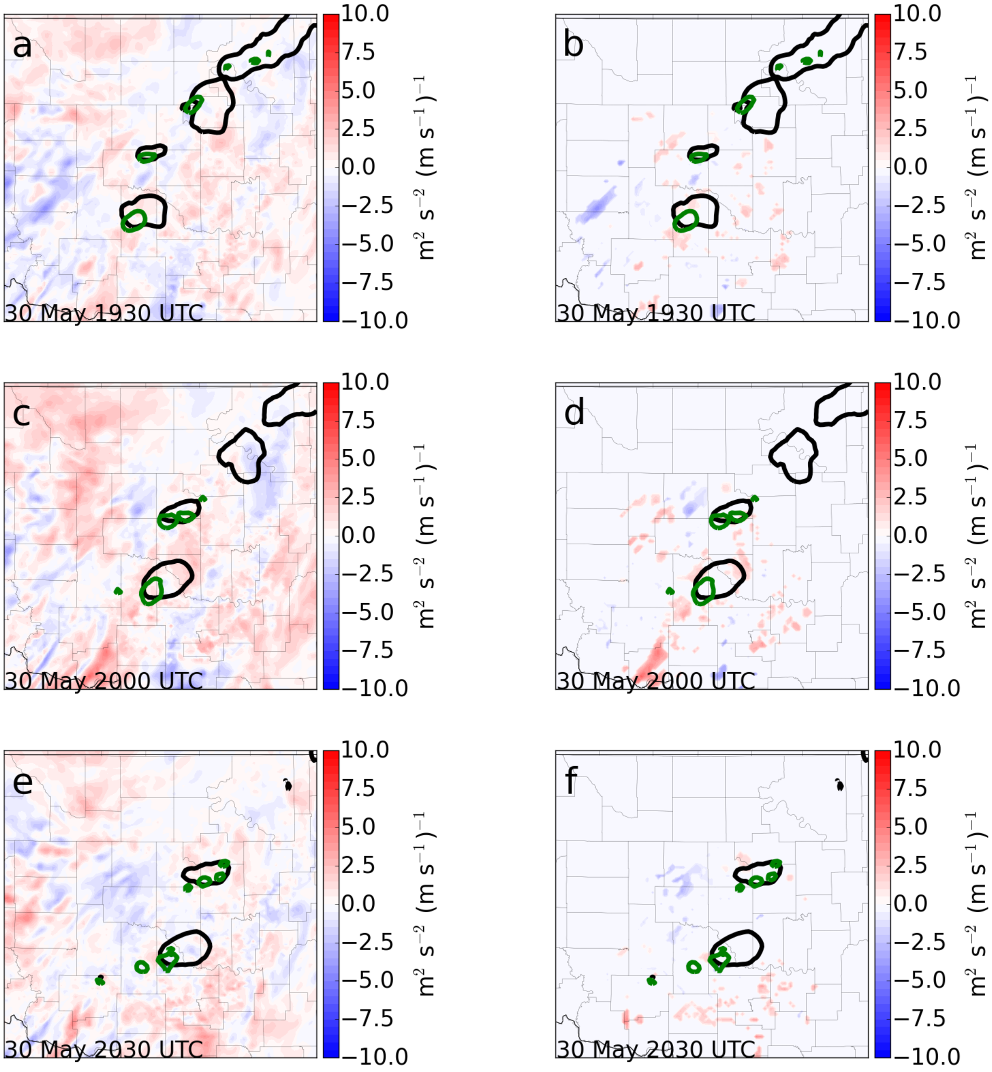

Figure 5.27. 30 May target storm averaged 2-5 km UH (> 5 m^2s^{-2}) sensitivity to initial one hour storm-induced change of SHR06 in m^2s^{-2} $(m\ s^{-1})^{-1}$ and ensemble mean forecasted reflectivity (20 dBZ; black contour) and 2-5 km UH (5 m^2s^{-2}; green contour) for forecast times (a) 30 minutes, valid 1930 UTC (b) 30 minutes with statistical significance test (c) 1-hour, valid 2000 UTC (d) 1-hour with statistical significance test (e) 90 minutes, valid 2030 UTC (f) 90 minutes with statistical significance test.

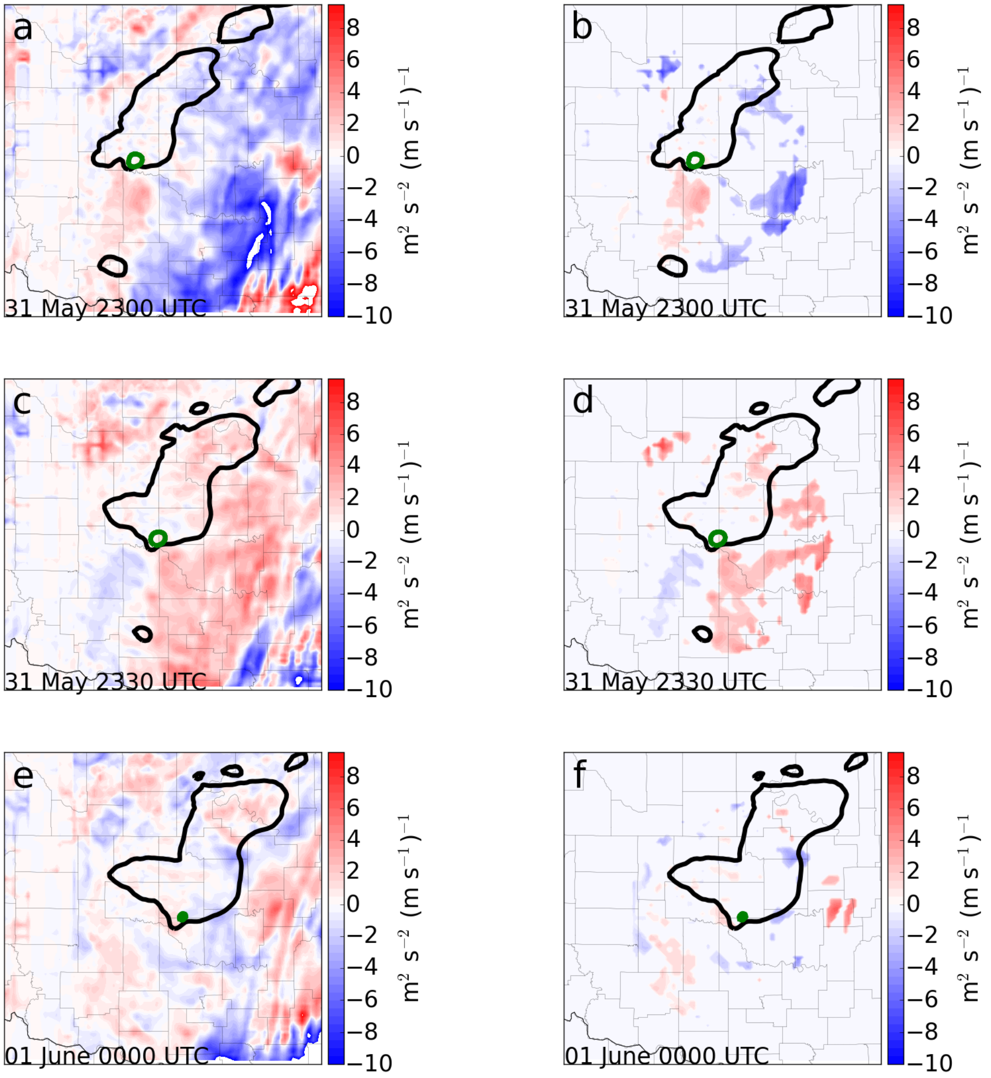

Figure 5.28. 31 May target storm averaged 2-5 km UH (> 75 m^2s^{-2}) sensitivity to initial one hour storm-induced change of SHR06 in m^2s^{-2} $(m\ s^{-1})^{-1}$ and ensemble mean forecasted reflectivity (20 dBZ; black contour) and 2-5 km UH (75 m^2s^{-2}; green contour) for forecast times (a) 30 minutes, valid 2300 UTC (b) 30 minutes with statistical significance test (c) 1-hour, valid 2300 UTC (d) 1-hour with statistical significance test (e) 90 minutes, valid 0000 UTC, 01 June (f) 90 minutes with statistical significance test.

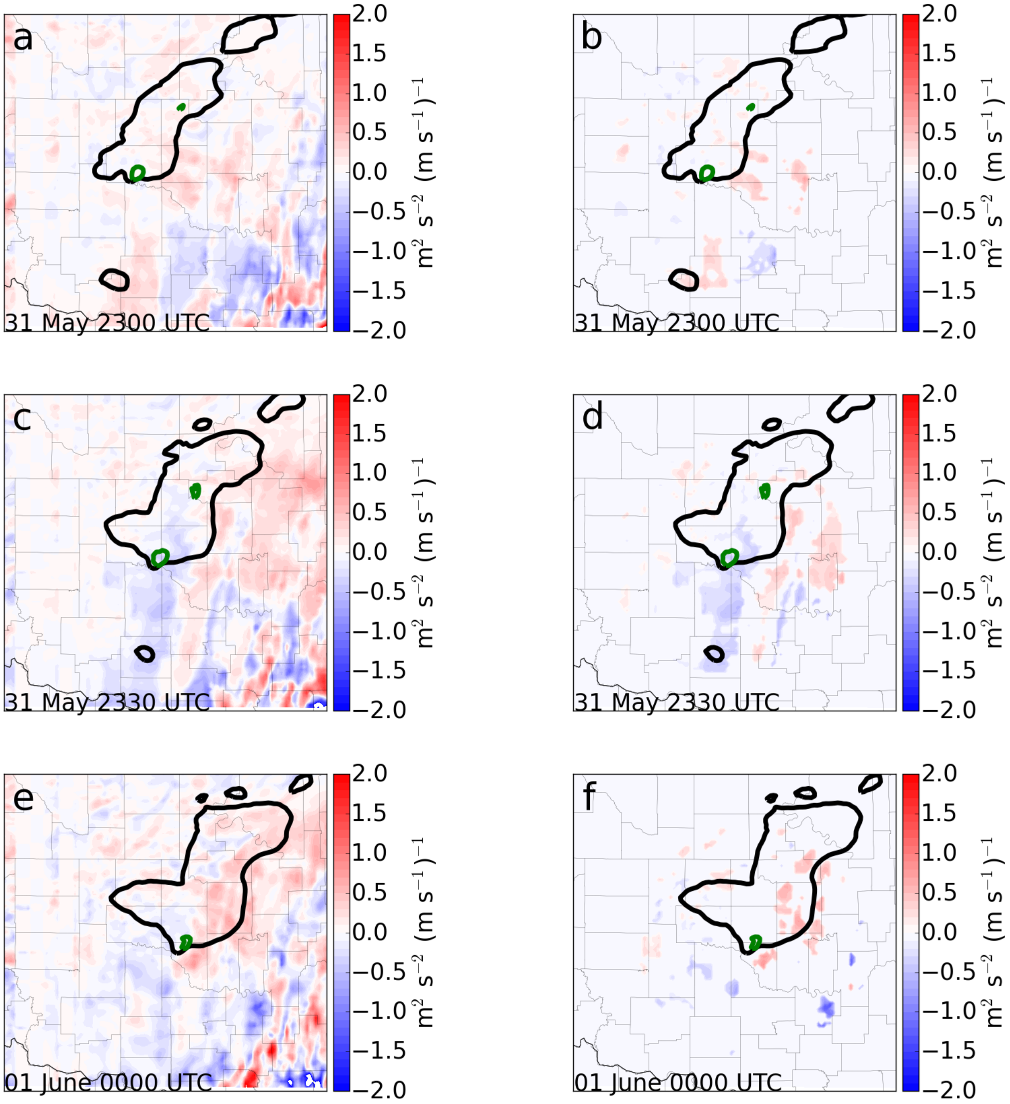

Figure 5.29. 31 May target storm averaged 0-1 km UH (> 5 m^2s^{-2}) sensitivity to initial one hour storm-induced change of SHR01 in m^2s^{-2} $(m\ s^{-1})^{-1}$ and ensemble mean forecasted reflectivity (20 dBZ; black contour) and 2-5 km UH (5 m^2s^{-2}; green contour) for forecast times (a) 30 minutes, valid 2300 UTC (b) 30 minutes with statistical significance test (c) 1-hour, valid 2300 UTC (d) 1-hour with statistical significance test (e) 90 minutes, valid 0000 UTC, 01 June (f) 90 minutes with statistical significance test.

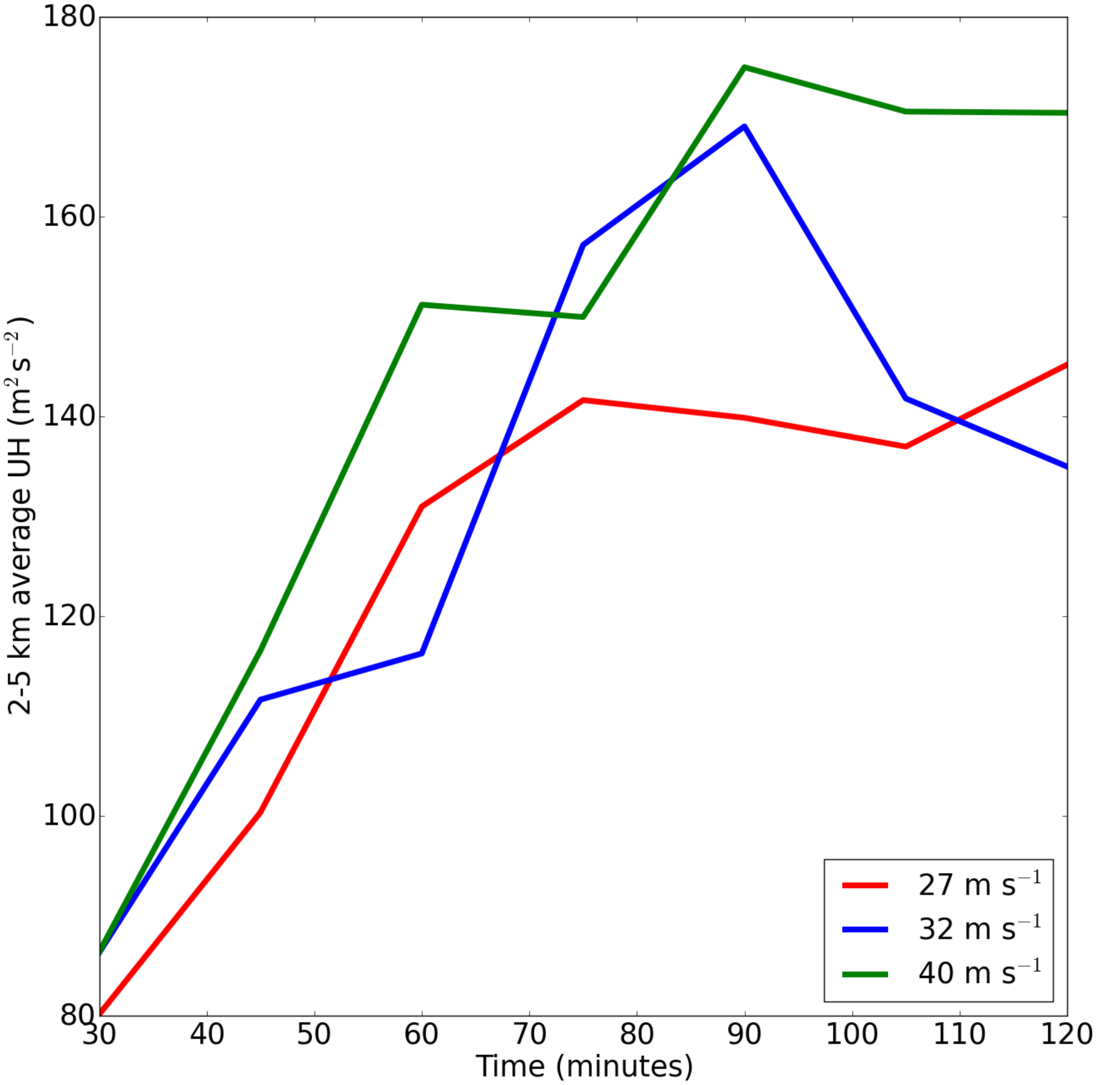

Figure 5.30. Idealized storm averaged 2-5 km UH with time for environments initialized with SHR06 of 27 m s^{-1} (red), 32 m s^{-1} (blue), 40 m s^{-1} (green).

5.5 Discussion and conclusions

The results of this chapter reveal how convection evolution is dependent on the surrounding near-storm environment. This dependency is shown for three case studies: one MCS and two supercells. The results suggest that it is imperative for the near-storm environment to be reasonably well represented in CAM initial conditions, especially in regions of high forecast sensitivity. Model biases for different state variables, as shown in Chapter 3, can degrade the accuracy of model initial conditions. Thus, model biases in areas of high forecast sensitivity may possibly have negative effects on forecast accuracy. The following are potential model biases that may impact forecasts based on ESA:

1) Under-depicted low-level inflow wind speed could affect supercell UH and multi-cell reflectivity. Since supercell UH in these cases is positively sensitive to inflow wind speed, an under-depiction of initial condition inflow winds should, in theory, lead to under-estimated forecasted UH. For the 29 May MCS case, the average forecast composite reflectivity is negatively sensitive to low-level inflow wind speed. From these results, it is suggested the under-depiction of inflow winds will lead to higher average reflectivity.
2) Comparison of observed and analysis wind shear shows the under-depiction of shear within model analyses due to the under-depiction of low-level wind speed. UH is positively sensitive to inflow vertical wind shear (over varying depths; some not shown) meaning a negative bias in initial condition shear would produce weaker forecast UH. For low-level

rotation, this under-depiction could be important to tornado probabilities derived from proxies.

3) In Chapter 3, results show cold pool depth is under-depicted in CAM analyses. ESA applied to the 29 May MCS shows small areas of negative sensitivity along the apex of the gust front for 850 hPa temperature, meaning colder temperatures at these locations are associated with higher reflectivity values. Deeper cold pools will cause their propagation speed to increase, thus resulting in more lift along the gust front.

Multiple ESAs use reflectivity and accumulated rainfall as forecast metrics and evaluate the resulting sensitivities from low- and mid-level moisture as depicted in the initial conditions. These results suggest that a more accurate depiction of initial condition low-level and cloud-level moisture could lead to improved forecasts of rainfall and flash flooding potential. Rainfall is also dependent on mid-level moisture in the 31 May case. A good representation of mid-level moisture will benefit rainfall forecasts, however, mid-level moisture in the proximity of convection is difficult to observe. In the future, available storm-scale satellite observations could improve initial conditions of these fields (Jones and Stensrud 2012).

These results from several ESAs using various forecast metrics and initial condition variables show clearly that low-level environmental features affect short-term convection evolution. However, the selection of initial condition variables is important and deserves careful attention. Variables at 850 hPa are selected as initial condition variables in this study since ensemble members have varying PBL schemes, making results from initial condition variables outside of the PBL more reliable. For example, using near-surface temperature, moisture, and winds in the ESAs would skew the results since members could be clustered together based on PBL scheme. Therefore, these ESAs would provide unreliable results. Variables below 850 hPa would be appropriate if an ensemble only used one PBL scheme, although it is probable that the near-surface environment will affect convection evolution in a similar manner as the 850 hPa environment. Regardless, the results suggest that observations from a dense network of surface observing systems near convective storms could improve short-term predictions of convection evolution via the concept of observation targeting.

A significant finding in this study is the presence of positive feedback between a convective storm and its surrounding environment. Since vertical wind shear is enhanced within supercell inflow regions and supercell rotation is affected by environmental shear, the storm-induced enhancements of shear result in larger UH at a later time. This effect is much stronger in the tornadic supercell of 31 May than the non-tornadic supercell of 30 May. The 31 May supercell was much larger and more intense given the high CAPE and storm-relative environmental helicity, thus the storm perturbed the environment to a much larger extent. These larger perturbations allow for more pronounced storm-environment positive feedback. This feedback could be a crucial part of mesocyclone maintenance and intensity and deserves further study.

In summary, ESA can be an effective tool on the storm-scale to reveal storm-environment dependencies. Future work should include more supercell case studies of various sizes and intensities to further explore storm-environment feedbacks. Sensitivities to environmental initial conditions can be coupled with observations within regions of high sensitivity to weight the ensemble member forecasts where the initial conditions are closest to these observations.

Summary

Understanding convection-environment interactions is crucial to convection predictability. The study assesses the impacts of convection on the surrounding environment and effects of these impacts on further convection evolution. The hypothesis that environmental perturbations have a significant impact on convection evolution is analyzed. The results of this study provide an in-depth analysis of convective storm and environmental interactions using both observations and CAMs. Observations are considered the ground truth and are used to verify CAM analyses and forecasts. Verified CAMs are then used to assess the influence of convection on the surrounding environment. Short-term convection forecast sensitivities to the surrounding environment, both the environment itself and changes to the environment, reveal convection evolution dependencies on the environmental features.

MPEX included frequent sampling of pre-convective and near-storm environments via mobile upsonde units. Using these unique observations, CAMs are verified in various near-storm environment regions including inflow, outflow, and anvil. CAM analyses and forecasts are shown to depict the near-storm environment reasonably well with a few exceptions. Low-level inflow wind speeds are under-depicted in both analyses and forecasts. Forecast inflow wind speeds biases nearly triple from that of analyses. Inflow winds that are too weak could hinder storm longevity and intensity. Cold pool depths are also under-depicted in CAMs. Shallow cold pools move slower which would affect the convection development along its leading edge.

Since the environments have been thoroughly verified using MPEX upsondes, CAMs are used to evaluate the impacts of convection on the surrounding environment.

Because short-term changes in an environment may or may not be storm-induced, the non-convection-allowing outer domain is used to isolate the storm-induced changes on the convection-allowing inner domain. For supercells, vertical wind shear increases within inflow regions due to an increase in low-level wind speed. This has been described in previous studies using idealized simulations of supercells. The under-depiction of low-level inflow wind speeds suggests that the observed shear may enhance to a greater extent. CAPE also increases in supercell inflow regions, particularly on 31 May. CAPE is depleted in outflow regions due to cold pool development. In the upper-troposphere, winds are accelerated in the upper-level outflow and may lead to enhancements in synoptic-scale jet streaks.

Ensemble sensitivity analysis is found to be a useful tool for diagnosing storm-environment dependencies. Reflectivity and accumulated rainfall are sensitive to low-level water vapor mixing ratio in multiple cases. Higher amounts of low-level inflow moisture will result in higher average storm reflectivity and accumulated rainfall. Supercell updraft helicity is also affected by the surrounding environment. It is found that an increase in inflow region initial condition shear will result in an increase in updraft helicity over various depths. Since inflow shear is enhanced by convection, the storm is somewhat self-sustaining, since an increase in shear by convection will enhance the storm's updraft helicity at a later time. This is an example of positive feedback between the storm and environment, and deserves further study to understand why this feature is more pronounced in some cases and not others.

Overall, this study has major implications for hazardous weather prediction. Understanding the environmental initial conditions necessary to predict hazards such as tornadoes, hail, and damaging winds will ultimately improve reliable forecast lead times. Improved knowledge of where environmental perturbations influence storm structure and evolution could lead to an improvement in how ensemble members are formulated. Future studies should assess other cases to create a large sample size of storm-environment interaction analyses, including supercell cases where the inflow wind shear feedback is present.

References

Aksoy, A., D. Dowell, and C. Snyder, 2009: A multicase comparative assessment of the ensemble Kalman filter for assimilation of radar observations. Part I: Storm-scale analyses. *Mon. Wea. Rev.*, **137**, 1805–1824.

Aksoy, A., D. Dowell, and C. Snyder, 2010: A multicase comparative assessment of the ensemble Kalman filter for assimilation of radar observations. Part II: Short-range ensemble forecasts. *Mon. Wea. Rev.*, **138**, 1273–1292.

Anabor, V., D. J. Stensrud, and O. L. L. de Moraes, 2009: Simulation of a serial upstream-propagating mesoscale convective system event over southeastern South America. *Mon. Wea. Rev.*, **137**, 2144–2163.

Ancell, B., and G. J. Hakim, 2007: Comparing adjoint- and ensemble-sensitivity analysis with applications to observation targeting. *Mon. Wea. Rev.*, **135**, 4117–4134.

Anderson, J. L., 2001: An ensemble adjustment filter for data assimilation. *Mon. Wea. Rev.*, **129**, 2884–2903.

Anderson, J. L., 2007: An adaptive covariance inflation error correction algorithm for ensemble filters. *Tellus*, **59A**, 210–224.

Anderson, J. L., T. Hoar, K. Raeder, H. Liu, N. Collins, R. Torn, and A. Avellano, 2009: The Data Assimilation Research Testbed: A community facility. *Bull. Amer. Meteor. Soc.*, **90**, 1283–1296.

Bednarczyk, C. N., and B. C. Ancell, 2015: Ensemble sensitivity analysis applied to a southern plains convective event. *Mon. Wea. Rev.*, **143**, 230–249.

Bluestein, H. B., J. C. Snyder, and J. B. Houser, 2015: A Multiscale Overview of the El Reno, Oklahoma, Tornadic Supercell of 31 May 2013. *Wea. Forecasting*, **30,** 525-552.

Brooks, H. E., C. A. Doswell III, and J. Cooper, 1994: On the environments of tornadic and nontornadic mesocyclones. *Wea. Forecasting*, **9**, 606–618.

Chang, E. K. M., M. Zheng, and K. Raeder, 2013: Medium-range ensemble sensitivity analysis of two extreme Pacific extratropical cyclones. *Mon. Wea. Rev.*, **141**, 211–231.

Cintineo, R. M., and D. J. Stensrud, 2013: On the predictability of supercell thunderstorm evolution. *J. Atmos. Sci.*, **70**, 1993–2011.

Clark, A. J., W. A. Gallus Jr., M. Xue, and F. Kong, 2010a: Growth of spread in convection-allowing and convection-parameterizing ensembles. *Wea. Forecasting*, 25, 594–612.

Clark, A. J., W. A. Gallus Jr., M. Xue, and F. Kong, 2010b: Convection-allowing and convection-parameterizing ensemble forecasts of a mesoscale convective vortex and associated severe weather environment. *Wea. Forecasting*, 25, 1052–1081.

Coniglio, M. C., J. Correia Jr., P. T. Marsh, and F. Kong, 2013: Verification of convection-allowing WRF model forecasts of the planetary boundary layer using sounding observations. *Wea. Forecasting*, **28**, 842–862.

Cortinas, J. V. and D. J. Stensrud, 1995: The importance of understanding mesoscale model parameterization schemes for weather forecasting. *Wea. Forecasting*, **10**, 716-740.

Cressman, G. P., 1959: An operational objective analysis system. *Mon. Wea. Rev.*, **87**, 367–374.

Dowell, D. C., F. Zhang, L. J. Wicker, C. Snyder, and N. A. Crook, 2004: Wind and temperature retrievals in the 17 May 1981 Arcadia, Oklahoma, supercell: Ensemble Kalman filter experiments. *Mon. Wea. Rev.*, **132**, 1982–2005.

Dowell, D. C., and L. J. Wicker, 2009: Additive noise for storm-scale ensemble forecasting and data assimilation. *J. Atmos. Oceanic Technol.*, **26**, 911–927.

Engerer, N. A., D. J. Stensrud, and M. C. Coniglio, 2008: Surface characteristics of observed cold pools. *Mon. Wea. Rev.,* 1**36**, 4839-4849.

Fritsch, J. M., and R. A. Maddox, 1981a: Convectively driven mesoscale pressure systems aloft. Part I: Observations. *J. Appl. Meteor.*, **20**, 9–19.

Fritsch, J. M., and R. A. Maddox, 1981b: Convective driven mesoscale weather systems aloft. Part II: Numerical simulations. *J. Appl. Meteor.*, **20**, 20–26.

Garcies, L., and V. Homar, 2009: Ensemble sensitivities of the real atmosphere: Application to Mediterranean intense cyclones. *Tellus*, **61A**, 394–406.

Garcies, L., and V. Homar, 2010: An optimized ensemble sensitivity climatology of Mediterranean intense cyclones. *Nat. Hazards Earth Syst. Sci.*, **10**, 2441–2450.

Gaspari, G., and S. E. Cohn, 1999: Construction of correlation functions in two and three dimensions. *Quart. J. Roy. Meteor. Soc.*, **125**, 723–757.

Hakim, G. J., and R. D. Torn, 2008: Ensemble synoptic analysis. *Synoptic-Dynamic Meteorology and Weather Analysis and Forecasting: A Tribute to Fred Sanders*, *Meteor. Monogr.*, No. 55, Amer. Meteor. Soc., 147–162.

Hill, A. J., C. C. Weiss, and B. C. Ancell, 2016: Ensemble sensitivity analysis for mesoscale forecasts of dryline convection initiation, *Mon. Wea. Rev*., **144**, 4161–4182.

Hitchcock, S. M., M. C. Coniglio, and K. H. Knopfmeier, 2016: Impact of MPEX upsonde observations on ensemble analyses and forecasts of the 31 May 2013 convective event over Oklahoma. *Mon. Wea. Rev*., **144**, 2889–2913.

Hong, S. –Y, S. Y. Noh, and J. Dudhia, 2006: A new vertical diffusion package with an explicit treatment of entrainment processes. *Mon. Wea. Rev*., **134**, 2318–2341.

Ito, K., and C.-C. Wu, 2013: Typhoon-position-oriented sensitivity analysis. Part I: Theory and verification. *J. Atmos. Sci.*, **70**, 2525–2546.

Johnson, A., X. Wang, J. R. Carley, L. J. Wicker, and C. Karstens, 2015: A comparison of multiscale GSI-based EnKF and 3DVar data assimilation using radar and conventional observations for midlatitude convective-scale precipitation forecasts. *Mon. Wea. Rev*., **143**, 3087–3108.

Jones, T. A., and D. J. Stensrud, 2012: Assimilating AIRS temperature and mixing ratio profiles using an ensemble Kalman filter approach for convective-scale forecasts. *Wea. Forecasting*, **27**, 541–564.

Jones, T. A., K. Knopfmeier, D. Wheatley, G. Creager, P. Minnis, and R. Palikondo, 2016: Storm-scale data assimilation and ensemble forecasting with the NSSL experimental Warn-on-Forecast system. Part II: Combined radar and satellite data experiments. *Wea. Forecasting*, **31**, 297–327.

Kain, J. S., S. J. Weiss, J. J. Levit, M. E. Baldwin, and D. R. Bright, 2006: Examination of convective allowing configurations of the WRF model for the prediction of severe convective weather: The SPC/NSSL spring program 2004. *Wea. Forecasting*, **21**, 167–181.

Kain, J. S., and Coauthors, 2008: Some practical considerations for the first generation of operational convection allowing NWP: How much resolution is enough? *Wea. Forecasting*, **23**, 931–952.

Kerr, C. A., D. J. Stensrud, and X. Wang, 2015: Assimilation of cloud-top temperature and radar observations of an idealized splitting supercell using an Observing System Simulation Experiment. *Mon. Wea. Rev.*, **143**, 1018–1034.

Kerr, C. A., D. J. Stensrud, and X. Wang, 2017: Verification of convection-allowing model ensemble analyses of near-storm environments using MPEX upsonde observations. *Mon. Wea. Rev.*, **145**, 857-875.

Keyser, D. A., and D. R. Johnson, 1984: Effects of diabatic heating on the ageostrophic circulation of an upper tropospheric jet streak. *Mon. Wea. Rev.*, **112**, 1709–1724.

Ku, H. H., 1966: Notes on the use of propagation of error formulas. *J. Res. Nat. Bureau Standards*, **70C**, 263–273.

Leary, C. A., 1979: Behavior of the wind field in the vicinity of a cloud cluster in the intertropical convergence zone. *J. Atmos. Sci.*, **36**, 631–639.

LeDimet, F., and O. Talagrand, 1986: Variational algorithms for analysis and assimilation of meteorological observations: Theoretical aspects. *Tellus*, **38A**, 97–110.

Maddox, R. A., 1980: Mesoscale convective complexes. *Bull. Amer. Meteor. Soc.*, **61**, 1374–1387.

Majcen, M., P. Markowski, Y. Richardson, D. Dowell, and J. Wurman, 2008: Multipass objective analyses of Doppler radar data. *J. Atmos. Oceanic Technol.*, **25**, 1845–1858.

McMurdie, L. A., and B. Ancell, 2014: Predictability characteristics of land-falling cyclones along the North American west coast. *Mon. Wea. Rev.*, **142**, 301–319.

Metz, N. D., and L. F. Bosart, 2010: Derecho and MCS development, evolution, and multiscale interactions during 3–5July 2003. *Mon. Wea. Rev.*, **138**, 3048–3070.

Ninomiya, K., 1971a: Dynamical analysis of outflow from tornado-producing thunderstorms as revealed by ATS III pictures. *J. Appl. Meteor.*, **10**, 275–294.

Ninomiya, K., 1971b: Mesoscale modification of synoptic situations from thunderstorm development as revealed by ATS III and aerological data. *J. Appl. Meteor.*, **10**, 1103–1121.

Parker, M. D., 2014: Composite VORTEX2 supercell environments from near-storm soundings. *Mon. Wea. Rev.*, **142**, 508–529.

Perkey, D. J., and R. A. Maddox, 1985: A numerical investigation of a mesoscale convective system. *Mon. Wea. Rev.*, **113**, 553–566.

Romine, G. S., C. S. Schwartz, R. D. Torn, and M. L. Weisman, 2016: Impact of assimilating dropsonde observations from MPEX on ensemble forecasts of severe weather events. Mon. Wea. Rev., 144, 3799– 3823.

Rotunno, R., J. B. Klemp, and M. L. Weisman, 1988: A theory for strong, long-lived squall lines. *J. Atmos. Sci.*, **45,** 463–485.

Sapucci, L. F., L. A. T. Machado, R. B. Silveira, G. Fisch, and J. F. G. Monico, 2005: Analysis of relative humidity sensors at the WMO radiosonde intercomparison experiment in Brazil. *J. Atmos. Oceanic Technol.*, **22,** 664–678.

Skamarock, W. C., and Coauthors, 2008: A description of the Advanced Research WRF version 3. NCAR Tech. Note TN–475+STR, 113 pp. [Available online at http://www2.mmm.ucar.edu/wrf/users/docs/arw_v3.pdf.]

Smull, B. F., and J. A. Augustine, 1993: Multiscale analysis of a mature mesoscale convective complex. *Mon. Wea. Rev.*,**121**, 103–132.

Snyder, C., and F. Zhang, 2003: Assimilation of simulated Doppler radar observations with an ensemble Kalman filter. *Mon. Wea. Rev.*, **131**, 1663–1677.

Sobash, R. A., and D. J. Stensrud, 2015: Assimilating surface mesonet observations with the EnKF to improve ensemble forecasts of convection initiation on 29 May 2012. *Mon. Wea. Rev.*, **143**, 3700–3725.

Sobash, R. A., and L. J. Wicker, 2015: On the impact of additive noise in storm-scale EnKF experiments. *Mon. Wea. Rev.*,**143**, 3067–3086.

Stensrud, D. J., 1996: Effects of a persistent, midlatitude mesoscale region of convection on the large-scale environment during the warm season. *J. Atmos. Sci.*, **53**, 3503–3527.

Stensrud, D. J., and J. L. Anderson, 2001: Is midlatitude convection an active or a passive player in producing global circulation patterns. *J. Climate*, **14**, 2222–2237.

Stensrud, D. J., and Coauthors, 2009: Convective-scale Warn-on-Forecast system: A vision for 2020. *Bull. Amer. Meteor. Soc.*, **90**, 1487–1499.

Stensrud, D. J., and Coauthors, 2013: Progress and challenges with Warn-on-Forecast. *Atmos. Res.*, **123**, 2–16

Thompson, G., P. R. Field, W. R. Hall, and R. M. Rasmussen, 2008: Explicit forecasts of winter precipitation using an improved bulk microphysics scheme. Part II: Implementation of a new snow parameterization. *Mon. Wea. Rev.*, **140**, 562–586.

Tong, M., and M. Xue, 2005: Ensemble Kalman filter assimilation of Doppler radar data with a compressible nonhydrostatic model: OSS experiments. *Mon. Wea. Rev.*, **133**, 1789 – 1807.

Torn, R. D., 2014: The impact of targeted dropwindsonde observations on tropical cyclone intensity forecasts of four weak systems during PREDICT. *Mon. Wea. Rev.*, **142**, 2860–2878.

Torn, R. D., and G. J. Hakim, 2008: Ensemble-based sensitivity analysis. *Mon. Wea. Rev.*, **136**, 663–677.

Torn, R. D., and G. J. Hakim, 2009: Initial condition sensitivity of western Pacific extratropical transitions determined using ensemble-based sensitivity analysis. *Mon. Wea. Rev.*, **137**, 3388–3406.

Torn, R. D., 2010: Ensemble-based sensitivity analysis applied to African easterly waves. *Wea. Forecasting*, **25**, 61–78.

Torn, R. D., and D. Cook, 2013: The role of vortex and environment errors in genesis forecasts of Hurricanes Danielle and Karl (2010). *Mon. Wea. Rev.*, **141**, 232–251.

Torn, R. D., and G. S. Romine, 2015: Sensitivity of central Oklahoma convection forecasts to upstream potential vorticity anomalies during two strongly forced cases during MPEX. *Mon. Wea. Rev.*, **143**, 4064–4087.

Trapp, R. J., D. J. Stensrud, M. C. Coniglio, R. S. Schumacher, M. E. Baldwin, S. Waugh, and D. T. Conlee, 2015: Mobile radiosonde deployments during the mesoscale predictability experiment (MPEX): Rapid and adaptive sampling of upscale convective feedbacks. *Bull. Amer. Meteor. Soc.*, **97,** 329-336.

Trapp, R. J. and J. M. Woznicki, 2017: Convectively induced stabilizations and subsequent recovery with supercell thunderstorms during the Mesoscale Predictability Experiment (MPEX). *Mon. Wea. Rev*., **145**, in press.

Trier, S. B., and R. D. Sharman, 2009: Convection-permitting simulations of the environment supporting widespread turbulence within the upper-level outflow of a mesoscale convective system. *Mon. Wea. Rev.*, **137**, 1972–1990.

Wagner, T. J., W. F. Feltz, and S. A. Ackerman, 2008: The temporal evolution of convective indices in storm-producing environments. *Wea. Forecasting*, **23**, 786–794.

Weisman, M. L., and J. B. Klemp, 1982: The dependence of numerically simulated convective storms on vertical wind shear and buoyancy. *Mon. Wea. Rev.*, **110**, 504–520.

Weisman, M. L., and R. Rotunno, 2004: “A theory for strong, long-lived squall lines” revisited. *J. Atmos. Sci.*, **61,** 361–382.

Weisman, M. L., and Coauthors, 2015: The Mesoscale Predictability Experiment (MPEX). *Bull. Amer. Meteor. Soc.*, **96**, 2127–2149.

Wheatley, D. M., D. J. Stensrud, D. C. Dowell, and N. Yussouf, 2012: Application of a WRF mesoscale data assimilation system to springtime severe weather events 2007–09. *Mon. Wea. Rev.*, **140**, 1539–1557.

Wheatley, D. M., N. Yussouf, and D. J. Stensrud, 2014: Ensemble Kalman filter analyses and forecasts of a severe mesoscale convective system using different choices of microphysics schemes. *Mon. Wea. Rev.*, **142**, 3243–3263.

Wheatley, D. M., K. H. Knopfmeier, T. A. Jones, and G. J. Creager, 2015: Storm-scale data assimilation and ensemble forecasting with the NSSL Experimental Warn-on-Forecast System. Part I: Radar data experiments. *Wea. Forecasting*, **30**,1795–1817.

Wilks, D. S., 2011: *Statistical Methods in the Atmospheric Sciences*. Academic Press, 676 pp.

Wolf, B. J., and D. R. Johnson, 1995a: The mesoscale forcing of a midlatitude upper-tropospheric jet streak by a simulated convective system. Part I: Mass circulation and ageostrophic processes. *Mon. Wea. Rev.*, **123**, 1059–1087.

Wolf, B. J., and D. R. Johnson, 1995b: The mesoscale forcing of a midlatitude upper-tropospheric jet streak by a simulated convective system. Part II: Kinetic energy and resolution analysis. *Mon. Wea. Rev.*, **123**, 1088–1111.

Xie, B., F. Zhang, Q. Zhang, J. Poterjoy, and Y. Weng, 2013: Observing strategy and observation targeting for tropical cyclones using ensemble-based sensitivity analysis and data assimilation. *Mon. Wea. Rev.*, **141**, 1437–1453.

Yussouf, N., and D. J. Stensrud, 2010: Impact of phased-array radar observations over a short assimilation period: Observing system simulation experiments using an ensemble Kalman filter. *Mon. Wea. Rev.*, **138**, 517–538.

Yussouf, N., E. R. Mansell, L. J. Wicker, D. M. Wheatley, and D. J. Stensrud, 2013: The ensemble Kalman filter analyses and forecasts of the 8 May 2003 Oklahoma City tornadic supercell storm using single- and double-moment microphysics schemes. *Mon. Wea. Rev.*, **141**, 3388–3412.

Yussouf, N., D. C. Dowell, L. J. Wicker, K. H. Knopfmeier, and D. M. Wheatley, 2015: Storm-scale data assimilation and ensemble forecasts for the 27 April 2011 severe weather outbreak in Alabama. *Mon. Wea. Rev.*, **143**, 3044–3066.

Zhang, F., N. Bei, R. Rotunno, C. Snyder, and C. C. Epifanio, 2007: Mesoscale predictability of moist baroclinic waves: Convection-permitting experiments and multistage error growth dynamics. *J. Atmos. Sci*., **64,** 3579–3594.